Study on
spatial structure of core impurity ions
using EUV spectroscopy in LHD

Xianli Huang

Doctor of Philosophy

Department of Fusion Science
School of Physical Sciences
The Graduate University for Advanced Studies

2015 School Year

Abstract

Impurity study in fusion plasmas is essentially important for the issues of impurity radiation loss and fuel dilution. The radial profile of impurity emissions contains plenty of valuable information for the impurity study. Therefore, a flat-field space-resolved extreme ultraviolet (EUV) spectrometer system working in wavelength range of 10–130 Å, which is named EUV-Short2, has been developed in the Large Helical Device (LHD) for the measurement of radial profiles of not only the line emission but also the bremsstrahlung continuum in the central column of plasmas. These measurements are aimed at studies on the impurity transport and Z_{eff}, respectively.

The new EUV spectrometer system has been equipped with a thin filter to block the spike noise entering the spectrometer through an entrance slit which is caused by high-energy neutral particles originating in neutral beam injection (NBI). Three filters of 11 μm thick beryllium (Be), 3.3 μm thick polypropylene (PP) and 0.5 μm thick polyethylene terephthalate (polyester, PET) have been examined on the performance for eliminating the spike noise, in particular, wavelength dependence of filter transmittance and particle penetration depth of filters. Although the 11 μm Be and 3.3 μm PP filters can fully delete the spike noise in wavelength range of $\lambda \leq 20$ Å, the signal intensity is also considerably reduced. The 0.5 μm PET filter, on the other hand, can maintain sufficient signal intensity for the measurement and a small number of spike noises remained in the signal is acceptable for the analysis. As a result, the EUV bremsstrahlung is successfully observed without spike noise at 20 Å even in low-density discharges, e.g. 2.9×10^{13} cm^{-3}, when the 0.5 μm PET filter is used. The energy distribution of spike noises is checked by analyzing the pulse height of the spike noise signal. The noise count is also analyzed and the result is compared between holographic and ruled gratings.

The spectral resolution of the spectrometer is examined as a function of wavelength. The spectral width, $\Delta\lambda_0$, measured at the foot position of a spectral line indicates a good spectral resolution, e.g. $\Delta\lambda_0 = 0.13$ Å at $\lambda = 20$ Å and $\Delta\lambda_0 = 0.33$ Å at $\lambda = 100$ Å with when 100 μm wide entrance slit is used. The vertical spatial resolution examined with vertical profiles of edge line emissions also indicates a

sufficient value, e.g. 3 cm when 1.0 mm wide spatial resolution slit is used. As a result, the vertical profile of Fe n = 3–2 L_α transition array composing of several spectral lines of FeXVII to FeXXIV, which are emitted in the narrow wavelength range of 10 to 18 Å, has been successfully observed with good spectral and spatial resolutions. Absolute intensity calibration of the spectrometer system is *in situ* carried out using visible and EUV bremsstrahlung continua.

Study on tungsten is one of the most important issues in the recent fusion research because the tungsten is used as a material in divertor of International Thermonuclear Experimental Reactor (ITER). In order to develop the tungsten diagnostics by measuring tungsten spectra, two coaxial pellets with tungsten inserted into graphite carbon and polyethylene (PE) tubes are designed and tested in LHD. The tungsten pellet with carbon tube causes plasma collapse, while that with PE tube smoothly finishes the ablation without collapse. The deposition profile of the two pellets is analyzed with a help of pellet ablation spectroscopy. It is found that the tungsten pellet with carbon tube can significantly penetrate into the core plasma and leads to the plasma collapse. Thus, the tungsten spectrum and its radial profile are successfully observed when the tungsten pellet with PE tube is used.

EUV line emission of FeXVII emitted from Ne-like ions (Fe^{16+}) is usually dominant in the Fe n = 3–2 L_α transition array because the Ne-like ions exist over a wide temperature range in the ionization equilibrium as well as He-like ions. Radial profiles of FeXVII 3s–2p and 3d–2p transitions emitted in wavelength range of 15-17 Å are observed and reconstructed into the local emissivity profile. The emissivity ratios among FeXVII n = 3–2 transitions calculated from the radial emissivity profile are compared with calculation based on a collisional-radiative (CR) model developed for Fe ions. The result reasonably confirms the effect of electron temperature and density on the emissivity ratios. However, the emissivity of 3C ($2p^5 3d\ ^1P_1 \rightarrow 2p^6$) transition is obviously lower than the prediction from the CR model. This discrepancy is consistent with measurements in the solar corona and other laboratory plasmas.

The EUV-Short2 spectrometer is attempted to measure the Z_{eff} profile because the Z_{eff} diagnostics using visible bremsstrahlung is only applicable to an extremely limited experimental condition, i.e. relatively high-density discharges ($n_e \geq 4 \times 10^{13}$ cm^{-3}) and inward-shifted configurations ($R_{ax} \leq 3.6$ m). The radial profile of EUV

bremsstrahlung is then measured with sufficient signal intensity by enlarging both the entrance and space-resolved slits and by installing the PET filter. The Z_{eff} profile analysis is carried out in low-density and high-T_i discharges with carbon pellet injection. The evolution of the Z_{eff} profile shows a centrally peaked profile just after the pellet injection, while the profile gradually returns to the original flat profile as a function of time. Comparison between Z_{eff} and T_i profiles in the plasma center clearly indicates a positive correlation between the two, i.e. T_i increases when Z_{eff} increases.

The Fe n = 3–2 L_α transition array is utilized for the impurity transport study in LHD. Since the radial location of Fe^{16+} through Fe^{23+} ions is widely distributed in LHD plasmas due to the large variation of the ionization energy, the impurity transport study is basically possible without any assumption on the radial structure of transport coefficients when the radial profile of the L_α transitions of FeXVII to FeXXIV is simultaneously measured. A one-dimensional impurity transport code is utilized to simulate the radial emissivity profile of iron L_α transitions. The transport coefficient can be then determined by fitting the measured profile of Fe L_α transitions in several ionization stages with the impurity transport code. The impurity transport analysis is attempted to discharges with peaked and hollow density profiles. The result suggests the convection velocity is mainly driven by the density gradient. It is also well described with neoclassical theory on the impurity transport.

Contents

List of figures

List of tables

Chapter 1

Introduction

1.1 Impurities in fusion plasmas

Production of electric energy based on magnetically confined fusion devices is an extremely attractive solution to entirely solve the energy problem in the human society because enormous amount of the fuel resource exist in the sea of the earth for the nuclear fusion [1]. Considering the cross-section in the fusion reaction, the most promising process for the fusion reactor is to use D-T reaction [2] of

$$D^{+} + T^{+} \rightarrow {}^{4}He^{2+}\ (3.52\ \text{MeV}) + n\ (14.06\ \text{MeV}), \qquad (1.1)$$

where D^+, T^+, $^4He^{2+}$ and n are the deuterium, the tritium, the alpha particle and the neutron, respectively. The kinetic energy (3.52 MeV) carried by the alpha particle is used for maintaining the self-sustainment of burning fusion plasmas through collisions with balk electrons and ions. The kinetic energy (14.06 MeV) of neutron is basically used for the source of electricity production through collisions with lithium in the blanket surrounding the vacuum vessel.

Because the fuel particles are positively charged in high-temperature plasmas, it is necessary to overcome a repulsive Coulomb potential by increasing the velocity and confinement time of fuel particles. The ignition condition necessary for self-sustainment of burning plasmas is called the Lawson criterion [3]. When the fusion plasma has a flat profile of n_i and T_i, it is given by

$$n_i T_i \tau_E > 3 \times 10^{15}\ \mathrm{cm^{-3}keVs}, \tag{1.2}$$

where n_i is the ion density, T_i the ion temperature and τ_E the energy confinement time. The energy confinement time is defined by

$$\tau_E = \frac{3}{2}\frac{\int n(T_i + T_e)dV}{P_{in}}, \tag{1.3}$$

where P_{in} is the total input power for heating the high-temperature plasma.

The Lawson criterion suggests that the fusion plasma with high temperature, e.g. $T = 10$ keV, needs to be confined in a fusion reactor for certain period, e.g. $\tau_E = 3$ s, at high ion densities, e.g. $n_i = 10^{14}$ cm^{-3}. For this purpose, toroidal devices for magnetic confinement of high-temperature plasmas, including both the tokamaks and stellarators, have been built in many countries of the world since 1950s, e.g. TFTR [4], JET [5], DII-D [6], JT-60U [7], ASDEX Upgrade [8] and LHD [9]. The International Thermonuclear Experimental Reactor (ITER) is currently under construction as a next-generation tokamak with D-T burning. ITER is aimed at the steady-state D-T operation with fusion power amplification of $Q \geq 5$ [10].

In the fusion research based on the magnetically confined high-temperature plasma, the impurity problem is one of fundamental issues which cannot be avoided. The alpha particle as the fusion product of D-T reaction becomes an intrinsic impurity species, so-called 'helium ash'. In addition, impurities like carbon, iron and tungsten may also be the intrinsic impurity which is brought by an interaction between the edge

plasma and plasma-facing components such as the first wall and divertor plates. These impurities mainly cause two problems in the fusion device. First, the impurity contamination dilutes the fuel ions and then leads to a reduction of the fusion output. In order to avoid this, the fraction of helium ash in the fusion reactor should be maintained at a low level (< 10%). Second, the plasma power balance can be seriously affected by the radiation loss from impurity ions. The impurity ions emit not only the line radiation but also the bremsstrahlung or synchrotron radiation in the fusion plasma. The total energy loss through these processes rapidly increases against the impurity atomic number, Z. For example, when the iron ($Z = 26$) density fraction is 0.2% to the fuel ions, the radiation power exceeds 10% of the total fusion power [2]. In the case of tungsten ($Z = 74$) the fraction is very small, i.e. below 0.01%, to reproduce the same radiation loss as the iron. Therefore, the high-Z impurity must be removed at least from the plasma core in the fusion reactor.

In order to control the impurity influx and reduce the impurity density, understanding of the impurity transport in the fusion plasma is extremely important. According to the neoclassical theory on the impurity transport, the collision between the fuel ion and high-Z impurity basically causes an impurity concentration towards the plasma center, which is called 'impurity accumulation' [11]. However, the impurity accumulation can be reduced, if an effect of 'temperature screening' is dominant, which occurs at radial location where the temperature gradient is steep. As the typical example, it is reported in JET that ion cyclotron range of frequency heating (ICRF) can disturb the formation of the impurity accumulation [12]. The sawteeth crash is also found to be effective for lowering the central impurity concentration [13]. On the other hand, the anomalous transport becomes often dominant rather than the neoclassical transport. However, there exists no sufficient theory to explain the anomalous impurity transport, while a few experimental results suggest the effect of trapped electron mode (TEM) and ion temperature gradient (ITG) mode [14, 15]. In order to clarify the role of neoclassical transport and investigate the mechanism of anomalous transport, further experimental study is absolutely necessary on the impurity transport.

The impurity transport has been intensively studied in the core [16–23] and edge [23–28] plasmas of the Large Helical Device (LHD). Impurity accumulation is sometimes observed in discharges heated by neutral beam injection (NBI) [20]. The confinement time of impurities is found to increase with density. With an assumption

on the radial structure of transport coefficients, a positive relation between the inward convection and the impurity charge has been observed when the impurity transport is studied by injecting the impurity pellet [17]. It is also found that the inward convection in helium plasmas is lower than that in hydrogen plasmas [18]. A phenomenon called 'impurity hole' characterized by an outward impurity flux has been observed in high ion temperature discharges in LHD [23]. The underlying mechanism of the process is still in open question. In the ergodic layer of LHD, on the other hand, iron ions from the first wall are found to be prevented from entering the core plasma and then the iron concentration is always at a low level even if the impurity accumulation happens. This effective impurity screening is mainly a result of the friction force caused by the density gradient along the magnetic field, which dominates the thermal force due to the ion temperature gradient [24]. The screening effect is more efficient at higher densities and heavier impurities.

Recently, the study on tungsten becomes one of main topics in the fusion research because the tungsten is planned to use in ITER divertor [30, 31]. The tungsten divertor is being installed in many tokamaks for making prior arrangement to the ITER operation. The tungsten spectroscopy has been also extensively carried out in many fusion devices [32–36]. A result from ASDEX Upgrade suggests that the central ECRH heating reduces the central tungsten content [37]. A poloidally asymmetric distribution of the highly ionized tungsten ion has been observed in tokamaks such as JET [38]. The reason is attributed to the centrifugal force associated with the toroidal rotation [39], impurity localization caused by ICRF heating [40] and temperature anisotropies of the background ions produced by NBI [37]. The non-uniform distribution may give a significant effect on the neoclassical transport of impurity ions [41]. Due to a complex electronic structure in the tungsten atom, several line emissions and pseudo continua remain unidentified. In addition, the tungsten transport study seems to be difficult at present because rate coefficients of ionization and recombination for the tungsten ions include much uncertainty. In order to carry out detail analysis of the tungsten transport, both the theoretical and experimental efforts are strongly desired for determining the accurate rate coefficients, while some theoretical modeling for the tungsten ion is in progress [42]. Experimental determination of accurate rate coefficients is possible from the profile measurement of tungsten ion density.

1.2 EUV spectroscopy

1.2.1 EUV spectroscopy in fusion research

Spectroscopy is a powerful and essential tool for diagnostics of laboratory and space plasmas [43, 44]. Various spectroscopic methods have been developed to measure the line and continuum radiation emitted from electrons, ions and atoms in the plasma. Information on plasma parameters can be extracted from the spectroscopic data. In the fusion research, plasma spectroscopy covers a wide spectral range from infrared to soft X-rays [45], as listed in Table 1.1. When the electron temperature increases, the main part of impurity line radiation moves to shorter wavelength side, i.e. from vacuum ultraviolet (VUV) with low photon energies to soft x-rays with high photon energies. The present thesis is focused on the spectroscopy in the spectral wavelength range of 10 to 500 Å named extreme-ultraviolet (EUV) between VUV and soft x-rays.

Table 1.1 Spectral ranges for plasma spectroscopy

Spectral ranges	Wavelengths / Energy ranges
Near Infrared	7000–12000 Å / 1–2 eV
Visible	4000–7000 Å / 2–3 eV
Ultraviolet (UV)	2000–4000 Å / 3–6 eV
Vacuum ultraviolet (VUV)	500–2000 Å / 6–25 eV
Extreme ultraviolet (EUV)	10–500 Å / 25–1200 eV
Soft X-rays	1–10 Å / 1200–12000 eV

EUV spectroscopy plays an important role in the fusion research because most of impurity line emissions from low-, medium- and high-Z elements exist in the EUV wavelength range. The EUV spectroscopy can be also utilized for plasma diagnostics to determine plasma parameters such as T_e, n_e, T_i and Z_{eff} in addition to the application to the impurity transport study. For example, huge radiation loss caused by the high-Z

impurity has been revealed by the EUV spectroscopy on the Princeton Large Torus in the 1970s [46].

A diffraction grating in reflection and transmission types has been widely used in the spectroscopy because of its high resolving power [47]. In particular, the reflection grating with a grazing incident angle has been commonly adopted for the EUV spectroscopy. The principle of diffraction grating is expressed in the following equation of

$$m\lambda = d\,(\sin\alpha + \sin\beta)\,, \tag{1.4}$$

where m is the spectral order, λ the wavelength of diffracted light, d the groove spacing. Values of α and β denote the angles of incidence and diffraction, respectively. The inverse of the groove spacing, which is expressed by grooves per millimeter (g/mm), is usually given as a groove density of the grating. A typical groove shape of a ruled grating is shown in Fig. 1.1. As indicated in Eq. 1.4, the diffraction occurs in the parallel light when the optical path difference between neighboring two grooves is equal to the integral multiple of the light wavelength. Since the reflectivity of EUV light at normal incidence on the grating is extremely low, the EUV spectrometer must be operated at grazing angle.

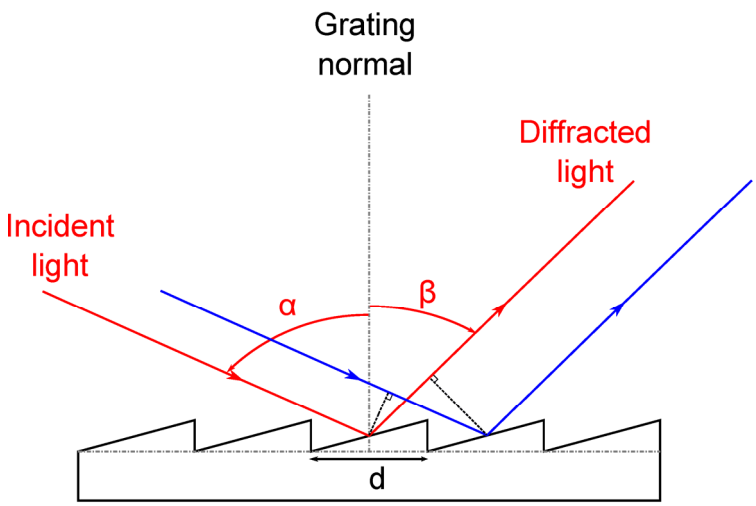

Fig. 1.1 Ruled grating and principle of diffraction.

A spectrometer equipped with a traditional spherical-concave grating is generally designed with the theory of Rowland mounting [48, 49]. The SPRED spectrometer with a toroidal ruled grating was developed in 1982 to obtain a flat focal plane instead of the Rowland mounting [50]. A design improvement was later done to achieve a

complete flat focal plane using an aberration corrected varied-line-spacing (VLS) concave ruled grating [51]. Excellent spectrometer performance has been obtained in the EUV range using a holographic grating on LHD [52, 53]. The holographic grating is fabricated based on an etching method with photoresist processing. Compared with the ruled grating, the holographic grating can well suppress the higher-order light and stray light [54]. In LHD, a space-resolved EUV spectrometer was also developed for profile measurement in the wavelength range of 50–500 Å [55]. The space-resolved EUV spectrometer has been recently upgraded to two-dimensional measurement system [56]. Further descriptions on the EUV spectrometers on LHD are given in the next section. At present, the EUV spectrometer has been widely used in many fusion devices such as NSTX [57], ASDEX-U [58], EAST [59], HL-2A [60].

1.2.2 EUV spectrometers on LHD

The EUV spectrometers installed on LHD are listed in Table 1.2. Two spectrometers with 1200 and 2400 grooves/mm laminar-type holographic gratings work as an impurity monitor in wavelength ranges of 50–500 Å named EUV-Long [52] and 10–130 Å named EUV-Short [53]. A space-resolved EUV spectrometer named EUV-Long2 with a 1200 g/mm grating for measuring the radial profile and two-dimensional distribution of impurity line emissions also covers the same long wavelength range as EUV-Long [55]. A mechanism has been added in the system to scan the observation chord horizontally during a single discharge [56]. At present it can measure either upper or lower half of LHD plasmas at horizontally elongated cross section by selecting an appropriate vertical angle in the observation chord. The observation chord of the spectrometer can be also moved in the horizontal direction for the two-dimensional measurement. A new spectrometer named EUV-Short2 working in the short-wavelength range as well as EUV-Short has been developed in the present thesis work. The observation range is fixed to the upper half of LHD plasmas at horizontally elongated plasma cross section.

A schematic drawing of the EUV spectrometer on LHD is displayed in Fig. 1.2 in the top view. The main conponents of the EUV spectrometer consist of an entrance slit, a gold-coated varied-line-spacing grating and a charge-coupled device (CCD) detector. A spatial resolution slit is placed in front of the entrance slit for radial profile measurement. A photo of EUV-Short2 is shown in Fig. 1.3.

Table 1.2 List of EUV spectrometers on LHD

Spectrometer	Grating type, grove density (g/mm) and angle of incidence (deg.)	Wavelength range (Å)	Profile measurement
EUV-Long	Holographic, 1200, 87.0	50–500	No
EUV-Short	Holographic, 2400, 88.65	10–130	No
EUV-Long2	Holographic, 1200, 87.0	50–500	Upper or lower half profile, 2-D distribution
EUV-Short2	Holographic, 2400, 88.6	10–130	Upper half profile

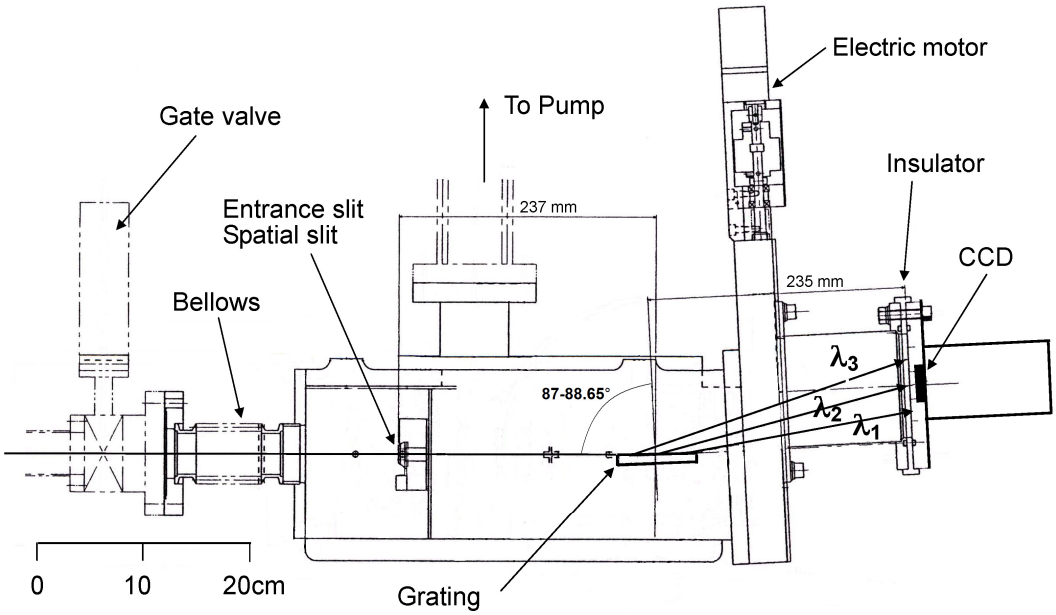

Fig. 1.2 Schematic drawing of EUV spectrometer on LHD in top view.

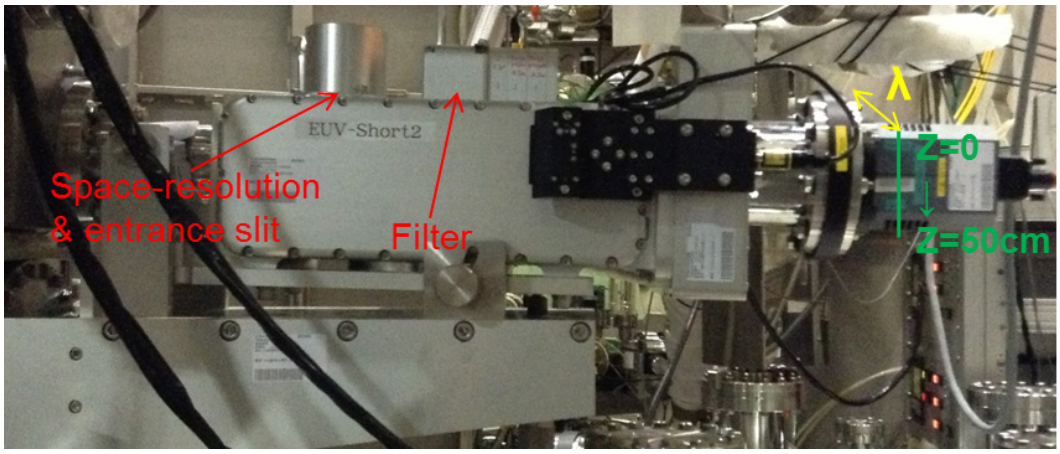

Fig. 1.3 Photo of EUV-Short2 in side view. Directions of wavelength and vertical profile on the focal plane are denoted by yellow and green bars, respectively.

1.3 Large Helical Device and relevant diagnostics

Large Helical Device (LHD) is the largest superconducting stellarator in the world. The main objective of the LHD project is to make comprehensive understanding on the plasma physics in toroidal systems and to develop technologies for a steady-state fusion reactor. LHD has a pair of superconducting helical coils and three pairs of superconducting poloidal coils. The poloidal and toroidal pitch numbers of the helical coils are l = 2 and of m = 10, respectively [61]. The three pairs of poloidal coils are composed of outer vertical (OV) and inner vertical (IV) and inner shaping (IS) coils. The OV and IV coils are used for cancelation of the vertical field produced by the helical coils and horizontal shift of the magnetic axis. The IS coil is used for controling the plasma shape of elliptical LHD plasmas. A bird's-eye view of LHD is displayed in Fig. 1.3 [62]. The main specifications of LHD and achieved plasma parameters are listed in Table 1.3.

The LHD plasma is maintained and heated by electron cyclotron resonance heating (ECH) [63], ion cyclotron range of frequency (ICRF) heating [64] and neutral beam injection (NBI) heating [65]. The LHD discharge is usually initiated by ECH. The ICRF and ECH heating are also used for steady operation of long pulse

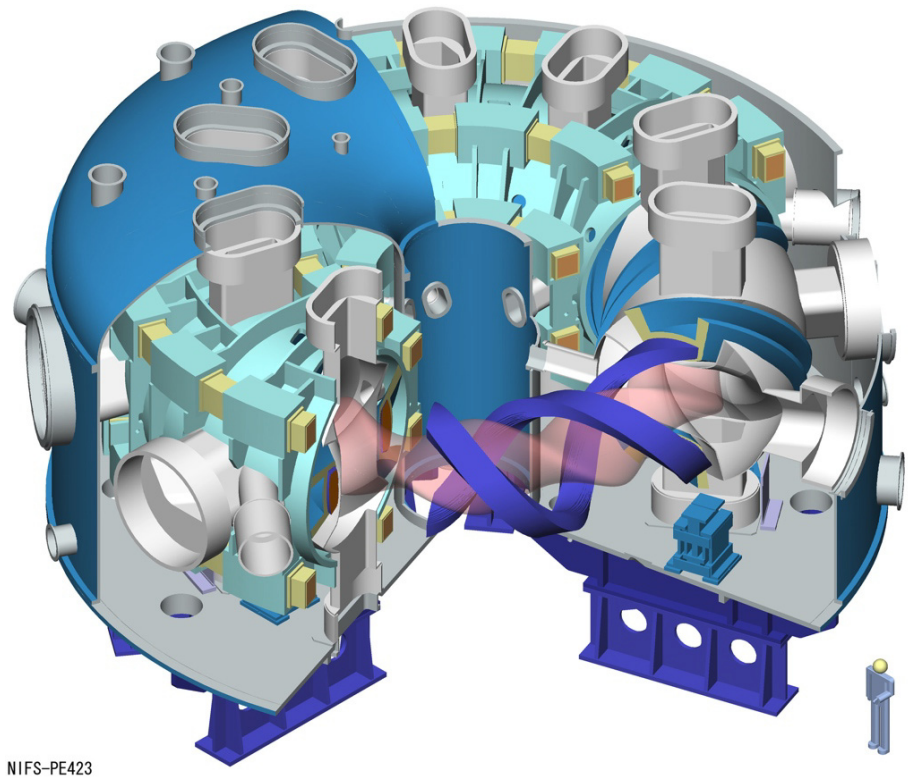

Fig. 1.4 Bird's-eye view of LHD [62].

Table 1.3 Main specifications of LHD and achieved plasma parameters

Major plasma radius	$3.5 \leq R \leq 4.2$ m
Averaged plasma minor radius	$0.50 \leq a_p \leq 0.65$ m
Plasma volume within LCFS	$20 \leq V_{plasma} \leq 30$ m^3
Toroidal magnetic field	$B_t < 3$ T
ECRH power	$P_{ECH} \leq 3.7$ MW
ICRF power	$P_{ICRF} \leq 2$ MW
Port-through NBI power	$P_{NBI} \leq 28$ MW
Central electron temperature	$T_e \leq 15$ keV
Central ion temperature	$T_i \leq 8$ keV
Central electron density	$1\times10^{13} \leq n_e \leq 1\times10^{15}$ cm^{-3}

discharges up to 1 hour. The NBI consists of five beams. Three tangentially injected negative-ion-source-based NBI beams (n-NBI) have high energy of 180 keV, while two perpendicularly injected positive-ion-source-based NBI beams (p-NBI) have low energy of 40 keV. Therefore, the n-NBI mainly heats bulk electrons and always used for maintaining discharges, while the p-NBI mainly heats bulk ions and used for ion temperature increase in low-density discharges.

Various diagnostics have been installed on the LHD for the plasma control and plasma physics study [66]. The main diagnostics systems are listed in Table 1.4. Here, the diagnostics related to the thesis work is brief introduced.

The electron temperature profile is measured by a YAG Thomson scattering (TS) system [67] and electron cyclotron emission (ECE) diagnostics [68]. The electron density profile is provided by the TS system, a far infrared (FIR) laser interferometer [69], a millimeter-wave interferometer [70] and a CO_2 laser imaging interferometer [71]. The ion temperature is measured by charge exchange spectroscopy (CXS) and X-ray crystal spectroscopy [72].

The electron temperature and density profiles used in the thesis work are taken from the TS system and the FIR laser interferometer. The TS system observes the whole plasma region along a major radius (R) on the mid-plane with spatial resolution of 12–25 mm and temporal resolutions of 10–100 ms. The absolute value of the density profile obtained by the TS system is calibrated against the line-integrated density measured by millimeter interferometer. In the FIR laser interferometer, the CH_3OH laser at a wavelength of 118.8 μm has totally 13 probe beams vertically passing through the LHD plasma at vertically elongated plasma cross section. When the TS system is not available, the density profile is derived from line-integrated signals with an Abel inversion technique.

Table 1.4 Main diagnostics on LHD

Diagnostic	Measurement
Magnetic probes	Plasma current $I_p(t)$, plasma pressure, magnetic fluctuations
Millimeter-wave interferometer	Line-averaged electron density $<n_e>$
FIR and CO_2 laser interferometers	Radial profile of electron density $n_e(r, t)$
Microwave reflectometer	$n_e(r, t)$ and fluctuations
Thomson scattering	Radial profile of electron temperature $T_e(r, t)$, $n_e(r, t)$
Electron cyclotron emission (ECE) systems	$T_e(r, t)$
X-ray pulse height analyzer (PHA)	$T_e(r, t)$, impurities
Neutral particle analyzer (NPA)	Ion temperature $T_i(t)$, ion energy spectrum $f(E)$
Charge exchange spectroscopy (CXS)	$T_i(r, t)$, plasma poloidal rotation $V_p(r, t)$ and toroidal rotation $V_t(r, t)$
X-ray crystal spectroscopy	Central ion temperature $T_i(r = 0, t)$, $V_t(t)$
Bolometer	Total radiated power $P_{rad}(r, t)$
VUV and EUV spectroscopy	Impurities, $T_i(t)$
Visible spectroscopy	Impurities, neutral hydrogen density $n_{H0}(t)$, radial profiles of effective ion charge $Z_{eff}(r, t)$
Soft X-ray photodiode array	MHD
Plasma monitor camera	Plasma position and shape
CO_2 laser PCI	Micro-turbulence
Heavy ion beam probe (HIBP)	Plasma potential $\Phi_p(r, t)$ and fluctuation
Langmuir probe	$T_e(t)$, $n_e(t)$, $\Phi_p(t)$ of edge plasma
Li beam probe	Edge n_e fluctuation
Divertor interferometer	$<n_e>$ at divertor leg
Lost fast-ion probe	Pitch angle and energy of escaping fast ions
Visible / infrared TV	Plasma-wall interaction

1.4 Motivation and structure of thesis

Based on the newly developed space-resolved EUV-Short2 spectrometer working in the short-wavelength of 10–130 Å, the thesis study is focused on the following goals.

I. Radial profile measurement of the following spectral lines emitted from core plasma.

(1) Line emissions from H- and He-like ions of low-Z intrinsic impurities, such as CV (40.27 Å, 40.73 Å), CVI (28.47 Å, 33.73 Å), OVII (21.60 Å, 21.80 Å) and OVIII (16.01 Å, 18.97 Å), which usually have the strongest intensity in the short-wavelength EUV range and are important for good plasma control.

(2) Line emissions from intrinsically existing metallic impurities, such as FeXVII to FeXXIV at 10–20 Å, which can suggest a condition of plasma-wall interaction.

(3) Other impurity line emissions with impurity pellet injection, such as TiXIII to TiXX at 10–30 Å, MoXXIV to MoXXVIII at 65−90 Å and WXX to WXLV at 20–70 Å, which are useful for diagnostic purpose, atomic & molecular physics and spectrometer calibration in addition to the transport study.

These line emissions have been clearly observed using the impurity monitor (EUV-Short). Radial profile measurement of these emissions is very important for determination of the impurity ion density and spectroscopic use.

II. Impurity transport study in core plasmas of LHD, in particular, impurity accumulation and impurity hole. The Fe L_α transition array in the wavelength range of 10–20 Å has a unique advantage for the impurity transport study because the charge state of FeXVII-FeXXIV can be simultaneously measured with the radial profile.

III. Bremsstrahlung continuum profile measurement in short-wavelength EUV range for Z_{eff} diagnostics in low-density discharges and wider discharge conditions.

Since the visible bremsstrahlung continuum, which is usually used for Z_{eff} measurement in the fusion research, has extreme non-uniform poloidal distribution in

the thick ergodic layer at magnetic configurations of R_{ax} > 3.6 m, the Z_{eff} profile measurement with visible bremsstrahlung is only possible in relatively high-density discharges ($n_e \geq 4 \times 10^{13}$ cm^{-3}) at magnetic configuration of $R_{ax} \leq 3.6$ m. Application of the EUV bremsstrahlung continuum to the Z_{eff} profile measurement is highly attractive because the EUV bremsstrahlung has no emission in the ergodic layer and the intensity is much larger than the visible bremsstrahlung intensity.

The present thesis has the following structure;

Chapter 1 introduces the role of impurities in magnetically confined fusion plasmas. The EUV spectroscopy on the fusion device is briefly reviewed. The basic information on LHD and diagnostic instruments in LHD is also given in relation to the present thesis study.

Chapter 2 describes the development of the space-resolved EUV spectrometer working in the wavelength range of 10–130 Å, which is the base of the present thesis study. Details of the space-resolved EUV-Short2 spectrometer are explained with absolute intensity calibration and performance of a thin filter used for blocking spike noises originated in NBI fast ions.

Chapter 3 describes the result of coaxial pellet development for high-Z impurity pellet injection. Use of the coaxial pellet which can avoid plasma collapse is essentially important for the study on spectral identification and transport analysis of metallic impurities in LHD, in particular, the study on tungsten. The performance of two kinds of the co-axial pellet is discussed on the entirely different plasma response.

Chapter 4 presents a spectral analysis on Ne-like FeXVII n = 3–2 L_α transitions, which are usually dominant in the Fe L_α array consisting of FeXVII to FeXXIV. Emissivity ratios analyzed among several FeXVII L_α transitions are compared with theoretical predictions based on a collisional-radiative (CR) model.

Chapter 5 presents the Z_{eff} profile evaluated with EUV bremsstrahlung continuum in low-density and high-T_i discharges. The Z_{eff} profile after carbon pellet injection is analyzed as a function of time. The density dependence of Z_{eff} values is also examined.

Chapter 6 presents the result of impurity transport analysis using the Fe n = 3–2 L_α transition array. A one-dimensional impurity transport code is employed to determine the radial structure of transport coefficients. The Fe transport coefficients

are analyzed in discharges with peaked and hollow density profiles. The result is discussed on density and temperature gradients to compare with predictions from the neoclassical theory on the impurity transport.

Finally, the present thesis study is summarized in chapter 7.

References

[1] J. Freidberg, Plasma Physics and Fusion Energy, Cambridge University press, Cambridge (2007).

[2] J. Wesson, Tokamaks, 4th edition, Oxford University press, New York (2012).

[3] J. D. Lawson, the Proceedings of the Physical Society **B70**, 6 (1957).

[4] R.J. Hawryluk, Reviews of Modern Physics **70**, 537 (1998).

[5] J. Wesson, The Science of JET. JET Joint Undertaking (2000).

[6] J. L. Luxon *et al*., Plasma Phys. Control. Fusion **32**, 869 (1990).

[7] H. Ninomiya *et al*., Fusion Engineering and Design **51–52**, 1015 (2000).

[8] A. Kallenbach, J. Adamek, L. Aho-Mantila *et al*., Nucl. Fusion **51**, 094012 (2011).

[9] A. Komori *et al*., Nucl. Fusion, **49**,104015 (2009).

[10] R. Aymar, *et al*., Plasma Phys. Control. Fusion **44**, 519 (2002).

[11] S. P. Hirshman and D. J. Sigmar, Nuclear Fusion **21**, 1079 (1981).

[12] M. Valisa *et al*., Nucl. Fusion **51**, 033002 (2011).

[13] R. Dux *et al*., Nuclear Fusion, **39**, 1509 (1999).

[14] D. Villegas *et al*., Phys. Rev. Lett. **105**, 035002 (2010).

[15] N. T. Howard *et al*., Plasma Phys. Control. Fusion **56**, 124004 (2014).

[16] S. Morita *et al*., Fusion Sci. Technol. **59** 91 (2010).

[17] H. Nozato, *et al*., Phys. Plasma **11**, 1920 (2004).

[18] H. Nozato, *et al*., Phys. Plasma **13**, 092502 (2006).

[19] H. Y. Zhou, *et al*., J. Appl. Phys. **107**, 053306 (2010).

[20] C. F. Dong *et al*., Plasma Sci. Technol.**15**, 230 (2013).

[21] S. Morita *et al*., Plasma Sci. Technol. **11** 402 (2009).

[22] S. Muto *et al*., Plasma and Fusion Res. **2** S1069 (2007).

[23] M. Yoshinuma *et al*., Nucl. Fusion **49** 062002, (2009).

[24] S. Morita *et al*., Nucl. Fusion **53** 093017 (2013).

[25] S. Morita *et al*., Plasma Phys. Control. Fusion **56** 094007 (2014).

[26] M. Kobayashi, *et al*., Fusion Sci. Technol. **58** 220 (2010).

[27] M. Kobayashi, *et al*., Plasma and Fusion Res. **3**, S1005 (2008).

[28] M. B. Chowdhuri, *et al*., Phys. Plasma **16**, 062502 (2009).

[29] E. H. Wang *et al*., Rev. Sci. Instrum. **83**, 043503 (2012)

[30] R. A. Pitts *et al*., Phys. Scr. **2009**, 014001 (2009).

[31] V. Philipps, Journal of Nuclear Materials **415**, S2 (2011).

[32] S. Morita *et al*., AIP Conf. Proc. **1545**, 143 (2013).

[33] C. S. Harte *et al*., J. Phys. B: At. Mol. Opt. Phys. **43**, 205004 (2010).

[34] G. F. Matthews *et al*., Phys. Scr. **2011**, 014001 (2011).

[35] J. Clementson *et al*., Rev. Sci. Instrum. **81**, 10E326 (2010).

[36] T Pütterich *et al*., Plasma Phys. Control. Fusion **50**, 085016 (2008).

[37] R. Neu *et al*., Plasma Phys. Control. Fusion **44**, 811 (2002).

[38] T. Koskela *et al*., Plasma Phys. Control. Fusion **57** 045001(2015).

[39] F. L. Hinton and S. K. Wong Phys. Fluids **28**, 3082 (1985).

[40] M. M. L. Reinke, Plasma Phys. Control. Fusion **54** 045004 (2012).

[41] C. Angioni and P. Helander, Plasma Phys. Control. Fusion **56,** 124001 (2014) .

[42] I. Murakami, H. A. Sakaue, C. Suzuki *et al.*, IAEA FEC 2014, EX/P6-28.

[43] H. R. Griem *et al*., Principles of Plasma Spectroscopy, Cambridge University press, Cambridge (1997).

[44] H. Kunze, Introduction to Plasma Spectroscopy, Springer, Berlin (2009).

[45] B. C. Stratton *et al*., Fusion Sci. Technol. **53** 431 (2008).

[46] E. Hinnov *et al.* Nucl. Fusion **18**,1305 (1978).

[47] E. G. Loewen and E. Popov, Diffraction gratings and applications, Marcel Dekker, New York, 1997.

[48] A. WELLER *et al.*, JET-IR(87) (1987).

[49] J. A. R. SAMSON, *Techniques of Vacuum Ultraviolet Spectroscopy*, John Wiley and Sons, New York (1967).

[50] Fonck *et al*., Appl. Opt., **21**, 2115 (1982).

[51] T. Kita *et al.,* Appl. Opt. **22**, 512 (1983).

[52] M. B.Chowdhuri *et al.,* Rev. Sci. Instrum. **78**, 023501 (2007).

[53] M. B. Chowdhuri, S. Morita and M. Goto, Applied Optics **47,** 135 (2008).

[54] M. Koike *et al*., Proceeding of SPIE **4146**, 163 (2000).

[55] C. F. Dong, S. Morita, M. Goto and H. Y. Zhou, Rev. Sci. Instrum. **81,** 033107-1 (2010).

[56] E. H. Wang, S. Morita, M. Goto and C. F. Dong, Rev. Sci. Instrum. **83**, 043503 (2012).

[57] J. K. Lepson *et al*., J. Phys. B: At. Mol. Opt. Phys. **43,** 144018 (2010).

[58] Fonck R, Ramsey A and Yelle R, Appl. Opt. **21** 2115 (1982).

[59] Y. Shen, X. Du, W. Zhang *et al*., Nucl. Instrum. Methods Phys. Res., Sect. A **700**, 86 (2013).

[60] Z Y. Cui, H. Y. Zhou, S. Morita *et al.*, Plasma Sci. Technol. **15** 110 (2013).

[61] A. Iiyoshi, *et al*., Nucl. Fusion **39**, 1245 (1999).

[62] http://www.nifs.ac.jp.

[63] T. Shimozuma. *et al*., Fusion Eng. Des. **53**, 525 (2001).

[64] T. Mutoh, *et al*., Fusion Eng. Des. **26**, 387 (1995).

[65] M. Fujiwara, *et al*., Plasma Phys. Control. Fusion **41**, B157 (1999).

[66] Kawahata, *et al*., Fusion Sci. Technol. **58**, 331 (2010).

[67] K. Narihara, et. al. Rev. Sci. Instrum. **72**, 1122 (2001).

[68] Y. Nagayama, K. Kawahata, A. England, and Y. Ito, Rev. Sci. Instrum., **70**, 1021 (1999).

[69] K. Kawahata, *et al*., Rev. Sci. Instrum. **70**, 707 (1999).

[70] K. Kawahata, *et al*., Rev. Sci. Instrum. **70**, 695 (1999).

[71] K. Tanaka, *et al*., Rev. Sci. Instrum. **72**, 1089 (2001).

[72] S. Morita *et al*., Rev. Sci. Instrum, **74**, 2375 (2003)

Chapter 2

Development of space-resolved short-wavelength EUV spectroscopy

2.1 Introduction

The effective ion charge (Z_{eff}) which is one of important parameters in magnetically confined fusion plasmas can be derived from the local emissivity of bremsstrahlung continuum. The bremsstrahlung continuum in the visible range has been usually used for the Z_{eff} measurement in tokamaks [1]. In the Large Helical Device (LHD), however, the visible bremsstrahlung intensity profile is largely distorted and shows a completely non-uniform structure along the plasma radius due to the presence of edge ergodic layer except for a specific magnetic configuration

with thin ergodic layer [2]. A poloidally non-uniform visible bremsstrahlung structure is observed with strong intensity in outer edge of the ergodic layer at inboard side of the torus. On the contrary, the extreme ultraviolet (EUV) bremsstrahlung continuum is free of the poloidally non-uniform structure, since it is never emitted from such an outer edge of the ergodic layer with extremely low electron temperature. Therefore, EUV spectroscopy is a valuable tool for measuring the bremsstrahlung continuum in LHD. Up to now, the EUV spectroscopy has been generally used for monitoring the impurity behavior in fusion plasmas [3–12].

The EUV bremsstrahlung intensity profile has been measured in LHD using a space-resolved EUV spectrometer working in 50–500 Å and the Z_{eff} profile has been analyzed from the local emissivity profile of EUV bremsstrahlung in the vicinity of 100 Å [13]. However, the spectrum from the EUV spectrometer measured at low-density discharges of $n_{\mathrm{e}} \leq 3 \times 10^{13}$ cm^{-3} is fully contaminated by a spike signal noise originated in high-energy neutral particles from neutral beams (NBI) [13]. In LHD two types of NBI with positive (p-NBI) and negative (n-NBI) ion sources are operated at energies of 40 and 180 keV for plasma heating, respectively. In order to avoid this noise, a thin carbon filter with thickness of 150 nm was attempted to block the high-energy particle. Unfortunately, a large part of the signal noise, in particular the noise from n-NBI, could not be entirely deleted because such a filter with sufficient transmittance in the EUV range 50–500 Å is too thin to effectively block the energetic neutrals. Therefore, a new space-resolved spectrometer system working at shorter wavelength range, e.g., 10–30 Å, in which a thicker filter can be used, is desired to observe a noise-free EUV bremsstrahlung profile.

In addition, the spectra at shorter EUV range near soft x-ray are of great interest for the impurity study in fusion plasmas because line emissions from many impurity elements, in particular medium- and high-Z impurities which may cause a large radiation loss, exist in the short wavelength range. For instance, the iron as an intrinsic impurity in fusion plasmas emits several strong line emissions in a narrow wavelength range between 10 and 18 Å, forming the L_{α} (n = 3–2) transition array composing of several ionization stages of Fe^{16+} to Fe^{23+}. Another important impurity in this wavelength range is tungsten, which is the main candidate for diverter plate material in the International Thermonuclear Experimental Reactor (ITER) [14, 15]. The transport study of tungsten is an urgent topic for the fusion research in addition to the detailed spectral identification and analysis for development of tungsten

diagnostics. Observation of H- and He-like ions in intrinsically existing low-Z impurity such as carbon and oxygen emitted in the short EUV wavelength range is of course important, e.g., H-like OVIII: 18.97 Å and He-like CV: 40.27 Å, because such spectral lines are usually dominant in this wavelength range [16].

Based on the motivation mentioned above, a space-resolved flat-field spectrometer working in the wavelength range of 10–130 Å called EUV-Short2 has been developed on LHD. Up to now three flat-field EUV spectrometers have been previously installed on LHD. One of the spectrometers called EUV-Long2 is capable of measuring the spatial distribution in the wavelength range of 50–500 Å [17] and is mainly aimed at studies of the edge impurity transport, while other two spectrometers called EUV-Short and EUV-Long are working in the wavelength ranges of 10–130 Å and 50–500 Å, respectively and routinely monitor the temporal impurity behavior in LHD discharges with high-time resolution of 5 ms [16, 18]. The present EUV spectrometer newly developed is aimed at studies of the Z_{eff} and core impurity transport through the profile measurement of bremsstrahlung continuum and metallic impurities in the presence of large signal noise due to high-energy particles.

In the paper the characteristics of the space-resolved EUV spectrometer is described with result of absolute intensity calibration in section 2. Bremsstrahlung profiles are presented with characteristics of thin filters for blocking the NBI noise in section 3. Iron spectrum in wavelength range of 10–18 Å is identified in detailed and vertical profiles of iron emissions of FeXVII to FeXXIV are analyzed. The results are shown in section 4. The paper is summarized in section 5.

2.2 Details on space-resolved EUV spectrometer for 10–130 Å

2.2.1 Characteristic feature of the EUV Spectrometer

The EUV spectrometer newly developed here is motivated by radial profile measurement of EUV radiation in the wavelength range of 10–130 Å from the upper half of elliptical plasmas of LHD at horizontally elongated plasma cross section. A schematic drawing of the spectrometer arrangement is shown in Fig. 2.1. The optical axis of the spectrometer perpendicular to the toroidal magnetic field can be rotated

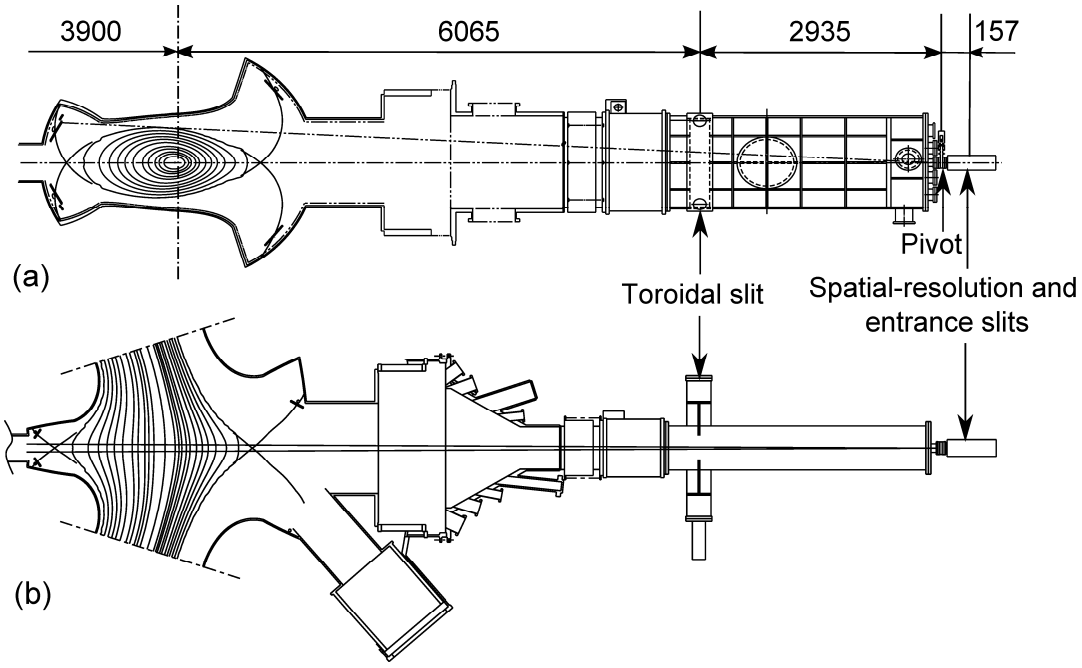

Fig. 2.1 (a) Side view and (b) top view of EUV spectrometer system working at 10–130 Å on LHD. The pivot denotes a central point for vertical and horizontal rotation of the spectrometer. The spectrometer is rotated around the central point to change the elevation angle of the central viewing chord. The elevation angle is carefully adjusted so that the observation range of the spectrometer can exactly cover the upper half of elliptical plasma at horizontally elongated plasma cross section.

about the pivot point vertically and horizontally to adjust the observation space. When the observation range is adjusted in the vertical plane, the elevation angle of the central viewing chord can be exactly determined to make possible the profile measurement at upper half vertical range of the elliptical plasma, i.e., Z = 0–50 cm. Here, Z = 0 denotes the equatorial plane. The toroidal slit shown in Fig. 2.1 is used to calibrate the elevation angle of each viewing chord [17]. The EUV spectrometer installed on a mid-plane port at the backside of rectangular vacuum extension chamber includes an entrance slit, a spatial-resolution slit, a filter unit with three different thin filters, a gold-coated concave varied-line-spacing (VLS) laminar-type holographic grating [19] with a groove density of 2400 per mm and a charge-coupled device (CCD) detector with 1024 × 255 pixels. A relatively long distance between the spectrometer and the plasma is necessary for observing the vertical plasma range

of 50 cm. In practice the distance between the central plasma position and the entrance slit of the spectrometer is set to 9157 mm when the plasma axis position is R_{ax} = 3.90 m. Since the distance between the entrance slit and the CCD detector is roughly 470 mm, which is a weak function of wavelength, we obtain a multiplication factor of 19.5. The CCD with effective area of 26.6 × 6.6 mm^2 (26 × 26 μm^2/pixel) is used in the present study. When the CCD is vertically placed on the spectrometer with horizontal wavelength dispersion, the vertical range of 520 mm (= 26.6 mm × 19.5) can be measured at the plasma center. The CCD is cooled by a Peltier device down to -20 ºC in order to reduce thermal noise in the CCD chip.

Two operation modes of the CCD are mainly used for the measurement, i.e., sub-image and full-image modes. When the vertical profile is measured, the CCD is operated with the sub-image mode to obtain a sufficient time response. In this mode, five pixels are usually summed up and converted into one channel in both dimensions of the CCD detector, while the full-image mode utilizes all the pixels of the CCD. The output data are reconstructed by 204 × 51 super-pixels. Even in this case, the CCD sampling time corresponding to the temporal resolution is considerably long, e.g., 200 ms. The full image mode is occasionally used when the elevation angle of viewing chords is calibrated and the spectral resolution of the spectrometer is examined. The sampling time is necessarily set longer than the discharge duration at the full image mode because the CCD requires extremely long time duration for the signal transfer to the shift register.

Figure 2.2 shows top view of the optical layout in the present EUV spectrometer. EUV radiation emitted from LHD plasmas passes through the entrance slit and

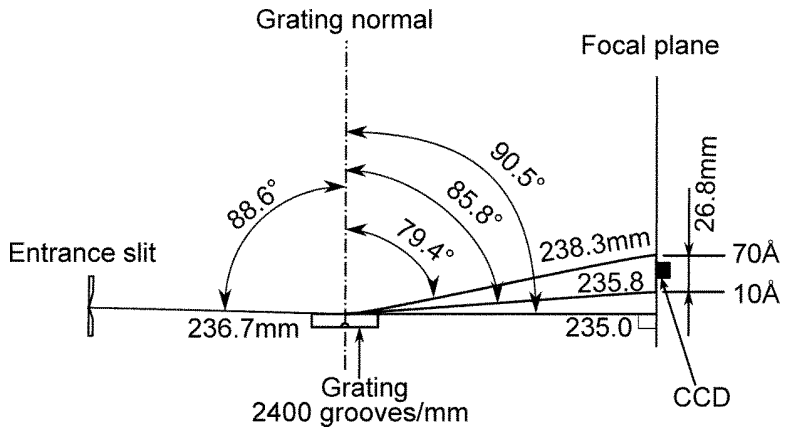

Fig. 2.2 Optical layout of space-resolved flat-field EUV spectrometer in top view.

reaches the grating adjusted at the angle of incidence of 88.6º. The diffracted EUV radiation is then focused on the focal plane as a function of the wavelength, satisfying Eq. 1.4. The focal length between the grating and the focal plane varies against the wavelength. Therefore, the multiplication factor at the vertical profile measurement slightly depends on the wavelength. An electric pulse motor directly connected to the CCD flange is remotely controlled by a computer through network to move the CCD detector position along the focal plane.

2.2.2 Performance of the EUV spectrometer

The spectral resolution of the spectrometer is examined in the full-image CCD mode by changing the entrance slit width, W_{en}. The spectral width, $\Delta\lambda_0$, is evaluated at the foot position of a spectral line, as shown in Fig. 2.3(a). Due to the varied dispersion against the wavelength, the value of $\Delta\lambda_0$ gradually increases with wavelength. If we consider the spectral resolving power, R, defined as $\lambda/\Delta\lambda_0$, it rapidly improves against the wavelength, e.g., from R = 142 at λ = 19 Å to R = 302 at λ = 101.6 Å when W_{en} = 100. The spectral resolution can be also improved even if a wider entrance slit is used, e.g., from R = 106 at λ = 19 Å to R = 264 at λ = 101.6 Å when W_{en} = 200μm and from R = 85 at λ = 19 Å to R = 211 at λ = 101.6 Å when W_{en} = 300 μm. Figure 2.3(b) shows the ratio of spectral line intensities among three different entrance slit widths. Both line intensities measured at W_{en} = 200 μm ($I_{200\mu m}$) and 300 μm ($I_{300\mu m}$) are normalized by line intensity measured at W_{en} = 100 μm ($I_{100\mu m}$). Although the ratios obtained here are scattered a little due to a relatively small signal-to-noise ratio, it can be roughly estimated that $I_{200\mu m}$ and $I_{300\mu m}$ are two and three times as large as $I_{100\mu m}$, respectively. In the daily experiment the entrance slit of W_{en} = 100 μm is used because it has better spectral resolution and the system brightness is not so dark compared to the slit of W_{en} = 200 μm and 300 μm. When the entrance slit width changes from 100 μm to 300 μm, the spectral resolution becomes clearly worse. However, the deterioration in the spectral resolution is tolerable even in such a wider slit case. The wider slit can be then used, if the signal intensity is weak.

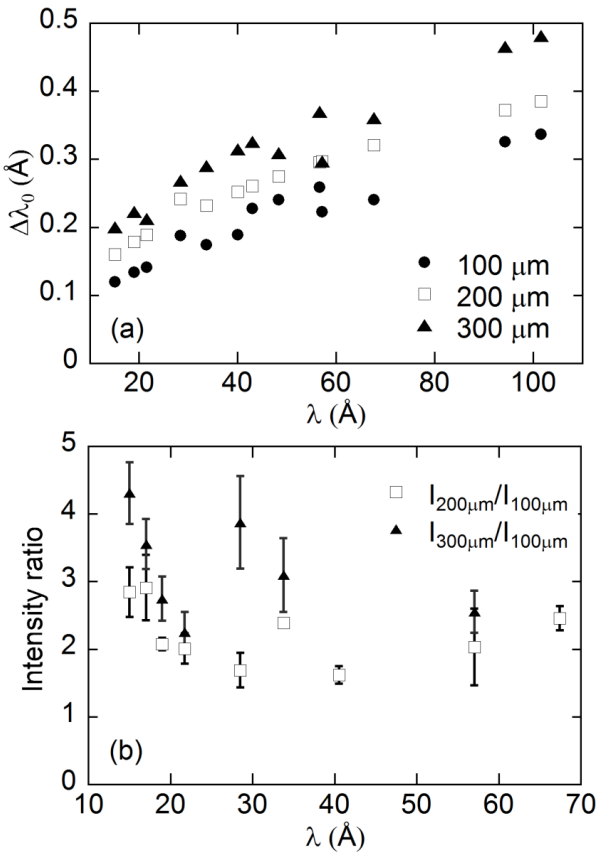

Fig. 2.3 (a) Spectral resolution, $\Delta\lambda_0$, defined by the full width at foot position of spectral line as a function of wavelength and (b) intensity ratios of line emissions at 200 μm (open squares) and 300 μm (solid triangles) entrance slit widths to that at 100 μm entrance slit width as a function of wavelength. Data are obtained with three different entrance slit widths of 100 μm (close circles), 200 μm (open squares) and 300 μm (solid triangles). Error bars stand for statistical deviations.

The spatial resolution in the vertical direction is basically determined by the width of the spatial-resolution slit, W_{sp}, while the pixel size of CCD and the distance between the grating and the CCD give a weak effect on it. Here, the spatial resolution is defined as the full width at half maximum (FWHM) in the vertical intensity profile of impurity line emissions localized in the plasma edge. In the present study the value of FWHM is evaluated from vertical profiles of CVI (40.27 Å) and OVII (21.60 Å), since those profiles distinctly have a sharp peak at the plasma edge. The result is shown in Fig. 2.4. The data are plotted for two different spatial slit widths of W_{sp} = 1.0 and 2.0 mm. The measured FWHM increases from 3 cm to 4 cm when the slit

width is switched from 1 mm to 2 mm. The result is compared with theoretical estimation indicated with solid line, which is calculated from the multiplication factor resulting from the geometric arrangement among LHD plasma, entrance slit and CCD. The measured resolution is close to the calculation at W_{sp} = 2.0 mm, whereas the value is roughly 1cm larger than the calculation at W_{sp} = 1.0 mm. It means that an exact radial emission width cannot be measured at W_{sp} = 2.0 mm due to the poor spatial resolution, while it is possible at W_{sp} = 1.0 mm. Making the deconvolution between the two values of measured and calculated FWHMs at W_{sp} = 1.0 mm, the real vertical location width of CV and OVII can be estimated to be 23 mm.

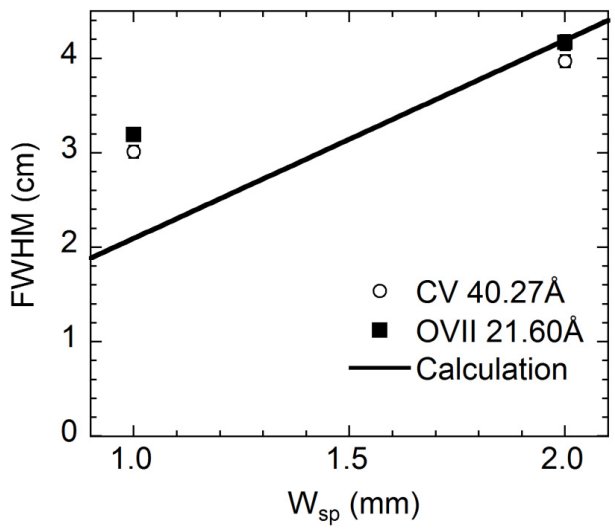

Fig. 2.4 Vertical spatial resolution defined by FWHM of edge vertical profiles of CV (open circles) and OVII (solid squares) as a function of spatial resolution slit width, W_{sp}. Solid line denotes calculated spatial resolution.

The spatial resolution in the toroidal direction is mainly determined by the angle of incidence (88.6°), the grating size (46 mm) and the multiplication factor (~ 19.2). The obtained spatial resolution of 22 mm is sufficiently small for the accurate measurement of the vertical profile, even if we consider that the elliptical plasma poloidally rotating five times during a toroidal turn makes the spatial resolution in the toroidal direction worse.

2.2.3 Absolute intensity calibration

Absolute intensity is necessary for quantitative analysis on the impurity radiation, impurity density and Z_{eff} profiles in addition to the impurity transport study. The signal intensity from the EUV spectrometer system can be absolutely calibrated using visible bremsstrahlung profile in which the intensity is already calibrated with an integrating sphere. This method has been firstly applied to another EUV system on LHD [20]. This technology provides us a remarkably convenient *in situ* calibration over the whole working wavelength range of the spectrometer system, since the bremsstrahlung continuum in fusion plasmas exists over the entire wavelength range from visible to X-ray.

The visible bremsstrahlung has been measured with an astigmatism-corrected Czerny-Turner-Type visible spectrometer [21]. The line-integrated visible bremsstrahlung profile is simultaneously observed at the wavelength range of 4575–6000 Å with a temporal resolution of 100 ms. A full vertical profile is obtained with 44 parallel viewing chords at horizontally elongated plasma cross section.

Absolute value in the local emissivity of visible bremsstrahlung continuum at 5364 Å is derived from the measured line-integrated intensity profile by means of Abel inversion as a function of magnetic surface, as shown in Fig. 2.5(a). The local emissivity of EUV bremsstrahlung can be then calculated with the following equation based on the local emissivity of visible bremsstrahlung;

$$\varepsilon_{\mathrm{brem\_EUV}} = \varepsilon_{\mathrm{brem\_vis}} \left(\frac{\lambda_{\mathrm{vis}}}{\lambda_{\mathrm{EUV}}}\right)^2 \frac{g_{\mathrm{ff\_EUV}}}{g_{\mathrm{ff\_vis}}} \exp\left[-\frac{12400}{T_{\mathrm{e}}}\left(\frac{1}{\lambda_{\mathrm{EUV}}} - \frac{1}{\lambda_{\mathrm{vis}}}\right)\right], \tag{2.1}$$

where the subscripts of 'EUV' and 'vis' denote a wavelength at EUV and visible bremsstrahlung emissions, respectively. Variables of ε [photons·cm^{-3}·s^{-1}·Å^{-1}], λ [Å], g_{ff} and T_{e} [eV] stand for the emissivity, the wavelength, the free-free gaunt factor and the electron temperature, respectively. The electron temperature profile is provided from the Thomson scattering system on LHD [22], as seen in Fig. 2.5(b). The free-free gaunt factor necessary for the present calibration is evaluated using a Chebyshev expansion as an analytical approximation [23, 24]. Here, it should be noticed that the present calibration technique does not need any information on the density profile.

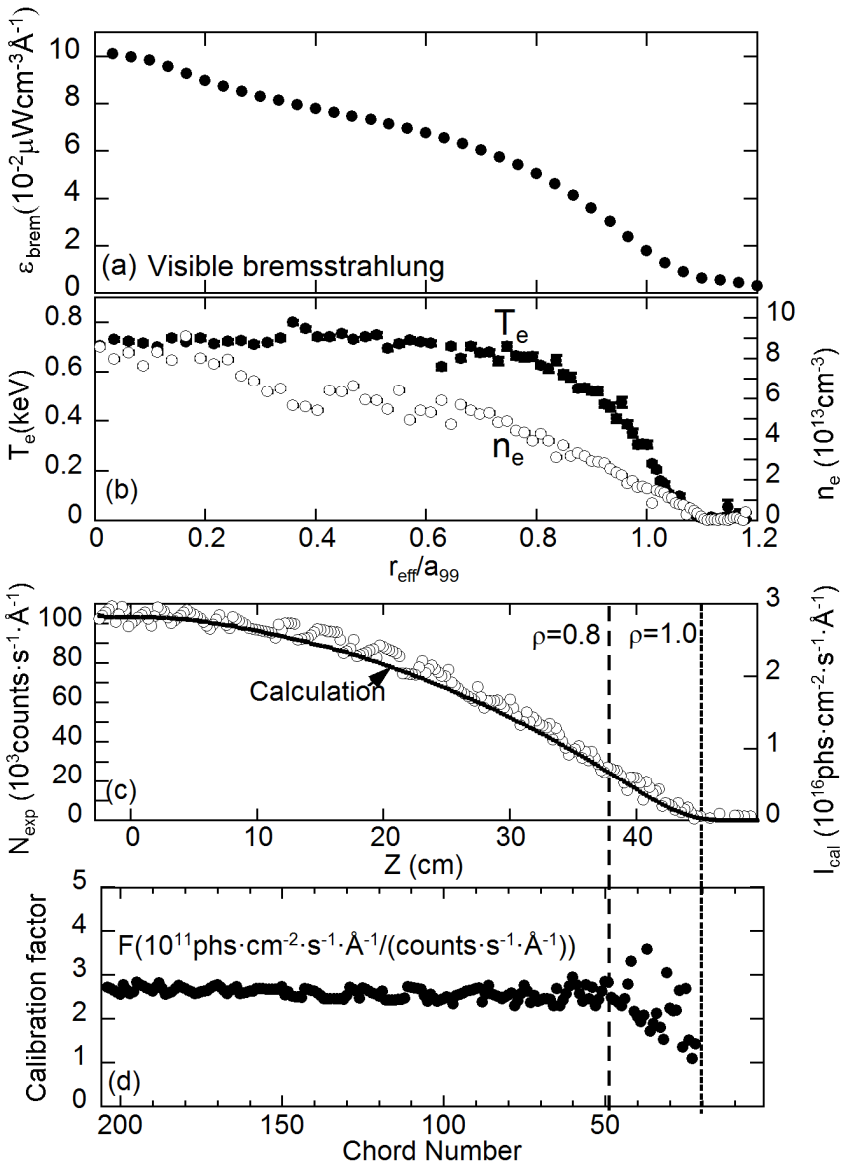

Fig. 2.5 (a) Emissivity profile of visible bremsstrahlung at 5364 Å and (b) electron temperature (solid circles) and density (open circles) profiles measured by the Thomson scattering system as a function averaged plasma minor radius, (c) chord-integrated profiles of calculated (solid line) and measured (open circles) EUV bremsstrahlung as a function of vertical position and (d) intensity calibration factor as a function of chord number in vertical profile measurement with space-resolved EUV spectrometer . The symbol of a_{99} denotes the plasma edge boundary defined at radial location in which the involved plasma stored energy is 99% to the total plasma stored energy.

Integrating the local EUV emissivity calculated with Eq. 2.2 along the viewing chord of the EUV spectrometer, a line-integrated intensity profile of the EUV bremsstrahlung can be estimated. Typical result obtained at 16.5 Å is shown in Fig. 2.5(c) with solid curve. Vertical axis of I_{cal} [photons·cm^{-2}·s^{-1}·Å^{-1}] indicates the calculated EUV bremsstrahlung intensity. The signal count of the EUV bremsstrahlung, N_{exp} [counts·s^{-1}·Å^{-1}], measured at 16.5 Å with the present EUV spectrometer system is also plotted in the figure with open circles. The calibration factor to evaluate the absolute intensity of the present EUV spectrometer system can be finally determined by directly comparing the measured signal profile with the calculated intensity profile. The result is plotted in Fig. 2.5(d). The calibration factor obtained from Fig. 2.1(a) indicates a uniform value within $\rho \leq 0.8$ against the viewing chord, whereas it shows a considerably large scattering in the range of $0.8 < \rho \leq 1.0$ due to the reduction of the signal-to-noise ratio. The uniform calibration factor within $\rho \leq 0.8$ strongly suggests a constant reflectivity of the holographic grating along the vertical direction perpendicular to the horizontal wavelength dispersion. In LHD a thick stochastic magnetic field layer sustaining edge plasma with relatively high density and temperature exist outside the last flux surface at $\rho = 1$. The edge plasma with three-dimensional structure at $\rho \geq 1$ may affect the scattered data in the bremsstrahlung profile appeared in the range of $0.8 < \rho \leq 1.0$.

A wavelength dependence of the calibration factor is also examined based on the method mentioned above. The result is shown in Fig. 2.6 with open circles. The data are fitted by a polynomial function denoted with solid line. A monotonic increase in the calibration factor against the wavelength reveals a rapid decrease in the sensitivity of the spectrometer system, in particular at $\lambda \geq 50$ Å. The bremsstrahlung intensity to be measured is actually too weak, when the wavelength is longer, e.g., $\lambda \geq 90$ Å. Therefore, the intensity calibration seems to be difficult in such longer wavelength range, unless an extreme high-density discharge using hydrogen multi-pellet injection, e.g., $n_e \geq 5 \times 10^{14}$ cm^{-3}, is adopted for the calibration. The uncertainty of the intensity calibration in the present study is estimated to be 6.4% which basically originates in the statistical deviation of the calibration factor.

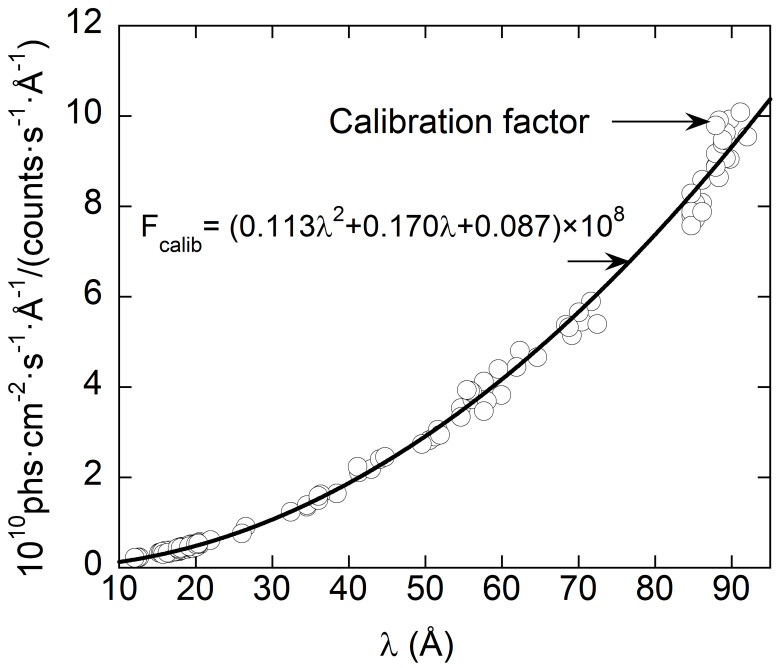

Fig. 2.6 Calibration factor as a function of wavelength obtained with the manner shown in Fig. 5. The calibration factor (F_{calib}) is fitted with polynomial expression which is denoted with solid line.

2.3 Filters for bremsstrahlung measurement

2.3.1 Spike noise caused by high-energy particles from NBI

Spectroscopy on LHD is basically free of spike noise caused by hard X-rays as seen in tokamaks due to the absence of the inductively or non-inductively accelerated non-thermal electrons for driving the plasma current. However, the spike noise has been unfortunately observed in the EUV spectrometers [13], while such a noise never appears in VUV spectrometers with small angle of incidence. In particular, the spike noise is enhanced in low-density NBI discharges in LHD.

A typical spectrum at line-averaged density of $n_e = 1.7 \times 10^{13}$ cm^{-3} during NBI discharge is shown in Fig. 2.7(a). The spectrum is fully dominated by the spike noise over all the wavelength range of 10–130 Å. It does not include bremsstrahlung continuum component because the density is quite low. Therefore, identification of line emissions is entirely difficult. When the density is increased to 4.0×10^{13} cm^{-3}, a few lines can be identified due to the reduced noise counts, as seen in Fig. 2.7(b).

After turning off the NBI pulse, on the other hand, the spike noise suddenly disappears from the spectrum, as shown in Fig. 2.7(c). Plenty of impurity line emissions can be clearly identified with weak bremsstrahlung continuum at the spectrum baseline. The spike noise also occurs immediately with the start-up of NBI. Therefore, the spike noise observed here is definitely attributed to high-energy neutral particles created by charge-exchange collision between high-energy ions arising from NBI and thermal hydrogen neutrals. These high-energy neutral particles coming out from the LHD plasma collide with the grating after passing through the entrance slit and are easily scattered over a wide angle inside the EUV spectrometer. Consequently, the spike noise is observed in the whole wavelength range as shown in Fig. 2.7(a). Another clear certification on the spike noise is seen in the spectrum from VUV spectrometers. Spike noise does not appear in the VUV spectrum at all

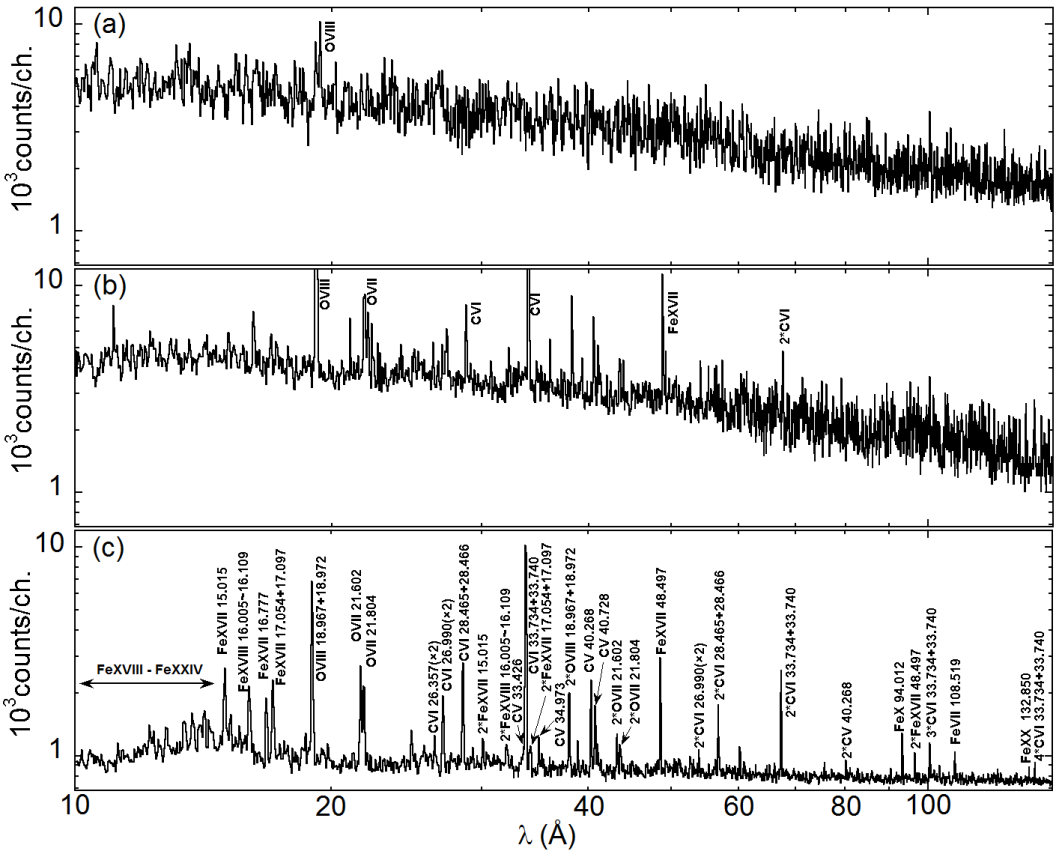

Fig. 2.7 EUV spectra at the range of 10–130 Å in hydrogen discharges with p- and n-NBIs at (a) $n_e = 1.7 \times 10^{13}$ cm^{-3} and (b) $n_e = 4.0 \times 10^{13}$ cm^{-3} and (c) after switching off NBI at $n_e = 1.7 \times 10^{13}$ cm^{-3}.

because the angle of incidence of the VUV spectrometer (< 30°) is very small compared to that of the EUV spectrometer (> 86°).

The spike noise appeared between 10 Å and 80 Å clearly differs between ruled and holographic gratings, suggesting a different feature of the particle scattering on the grating. Figure 2.8 shows the total counts per CCD frame as a function of NBI input power for comparison between the holographic (open squares) and ruled (solid circles) gratings, which are evaluated from NBI discharges with $n_e = 1.5–2.5 \times 10^{13}$ cm^{-3}. The data are obtained from another spectrometer (EUV-Short), which has no spatial resolution, with the same grating as the present spectrometer (EUV-Short2). Since only low-density discharges are adopted in plotting the figure, the total counts are mostly estimated to be from spike noises with an extraordinarily large peak value. The spike noise from the holographic grating is two times larger than that from the ruled grating, as indicated by linear fitting in Fig. 2.8 (dashed: holographic grating and solid: ruled grating). A difference in the reflectivity of EUV light between two types of gratings has been previously reported [18].

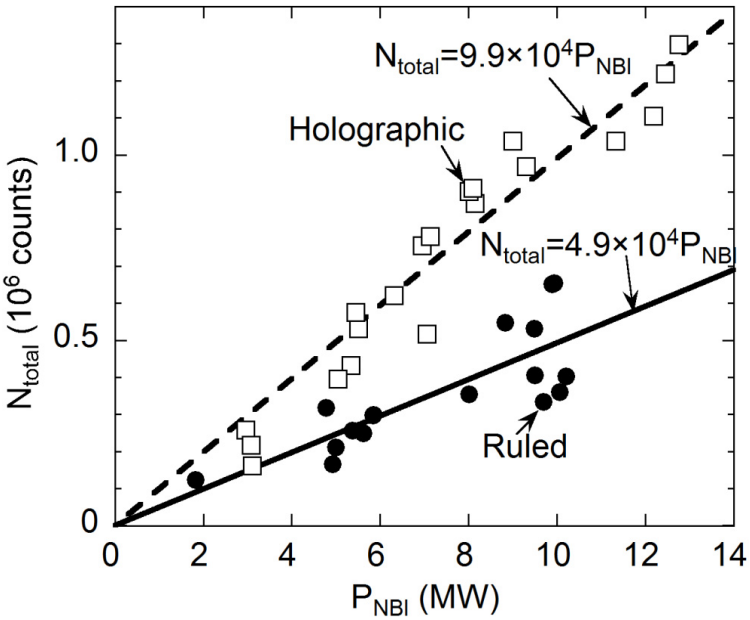

Fig. 2.8 Total spike noise counts per frame as a function of input power from tangential n-NBI at $n_e = 1.5–2.5 \times 10^{13}$ cm^{-3}. Data taken from ruled (solid circles) and holographic (open squares) gratings are fitted with polynomial expression (ruled: solid line and holographic: dashed line).

The reason why the observed spike noise is different between the two gratings arises from the surface structure. The groove shape of the ruled grating is triangle, while that of the holographic grating is rectangular. Therefore, the high-energy particle scattered at convex side of the rectangular-shaped holographic grating easily enters the CCD detector because there is no geometric barrier such as concave side of the holographic grating and the triangle-shaped ruled grating. The scattering efficiency and angular distribution of neutral particles are also affected by the surface roughness of the grating. It is reported that the surface microstructure with roughness ranging from a few nm to several hundred nm can effectively broaden the angular distribution when the neutral particle collides with a solid material at a grazing angle [25]. It is known the surface of the holographic grating is much smoother than that of the ruled grating because the stray light from the holographic grating is considerably small compared to the ruled grating. As a consequence, the surface roughness of the ruled grating may result in smaller spike noise by distributing the scattered particles into random angles.

In LHD three n-NBIs for electron heating and two p-NBIs for ion heating are installed at tangential and perpendicular injections against the toroidal plasma, respectively. Figure 2.9 (a) shows a tandem discharge using n- and p-NBIs. The n-NBI switched on at t = 3.3 s is replaced by p-NBI at t = 5.0 s and the p-NBI is switched off at t = 5.8 s. Temporal behaviors of the electron temperature and line-averaged density are shown in Fig. 2.9(b). The electron temperature behavior indicates an efficient heating by n-NBI due to the good central heat deposition. In the CCD detector the signal count created by a high-energy particle is proportional to the incident particle energy. Then, the incident energy of high-energy particles coming at the CCD can be estimated by the signal count of each spike noise. The pulse height distribution on the spike noise is analyzed as a function of the incident energy of high-energy particles for n- and p-NBI phases shown in Fig. 2.9(a). The same analysis is also done for EUV spectra without NBI, and the resultant pulse height distribution is used as the background emission, which is subtracted from the raw data in the present analysis. The result is plotted in Fig. 2.9(c). The pulse height distribution in Fig. 2.9(c) exactly reveals the contribution of high-energy particles from n- and p-NBIs. The figure clearly indicates a difference in the beam energy between the n- and p-NBIs. The total number of spike noises is roughly comparable between the n- and p-NBIs.

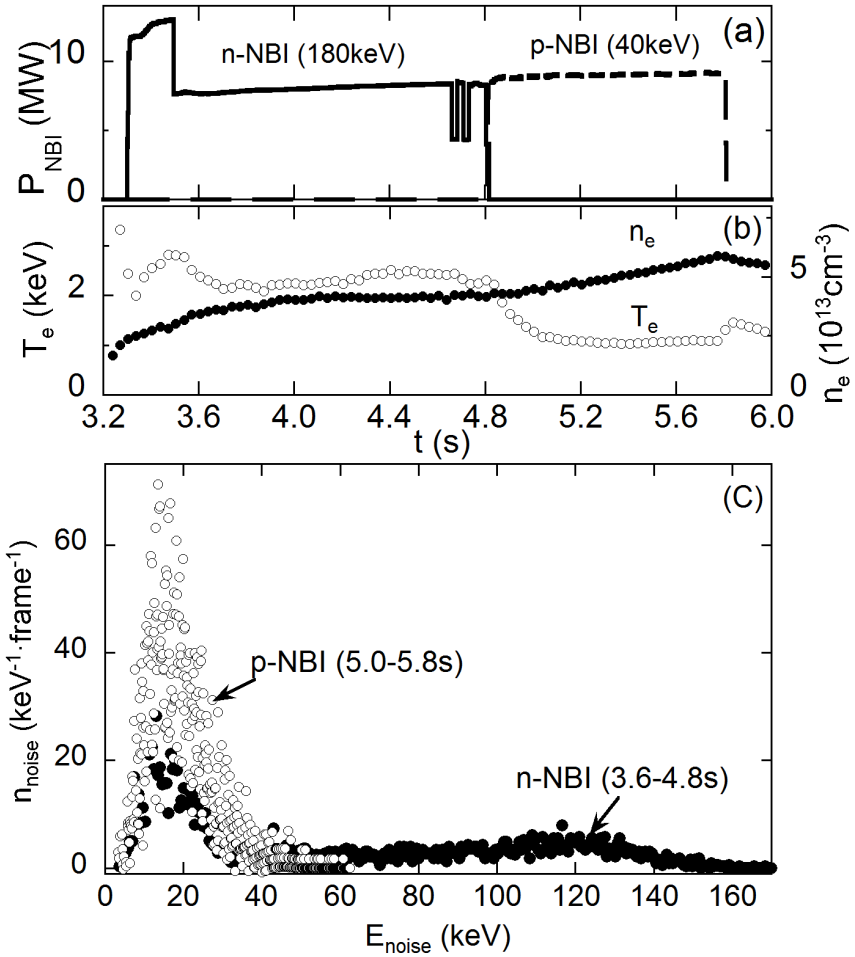

Fig. 2.9 (a) Time evolutions of port-through power of tangential n-NBI and perpendicular p-NBI and (b) electron temperature (open circles) and line-averaged density (close circles) and (c) pulse height distributions of spike noise caused by n-NBI (solid circles) and p-NBI (open circles).

Here, it is pointed out that the high-energy neutral particle flux coming out from the plasma largely depends on the angle to magnetic field lines, reflecting a different particle orbit during slowing down process against tangentially and perpendicularly injected beams. When the EUV spectrometer is installed perpendicularly to the toroidal plasma, the spike noise from p-NBI is much enhanced. On the contrary, when the spectrometer is installed tangentially to the toroidal plasma, the spike noise is basically dominated by n-NBI. In this case, however, the spike noise flux entirely depends on the direction of toroidally-circulating beam ions. If the EUV spectrometer observes the toroidally-circulating beam ions from backward direction, the spike

noise almost disappears. It is also pointed out that the result shown in Fig. 2.9(c) does not accurately indicate the ratio of high-energy neutral particle flux between n- and p-NBIs, since the particle scattering on the grating may be a little different between n- and p-NBIs. In the experiment, it is difficult to clearly distinguish the low-energy noise around 20 keV with relatively smaller peak counts from the impurity spectrum because the impurity line intensity peak count is comparable to the noise intensity count. It is reported that the high-energy particle collision above 100 keV may cause certain damage to the CCD detector [26]. However, any serious damage has not been observed in LHD at present, whereas the same CCD is being continuously used in LHD for ten years.

2.3.2 Filters for blocking high-energy particles

In order to eliminate or reduce the spike noise caused by NBIs, three kinds of filters, i.e., 11 μm thick beryllium (Be), 3.3 μm thick polypropylene (PP) and 0.5 μm thick polyethylene terephthalate (PET), have been individually installed behind the entrance slit. The percentage transmittance of the filters is shown in Fig. 2.10(a) as a function of wavelength. The 0.5 μm thick PET filter indicates the highest transmittance in wide range of EUV radiation, while the 11 μm thick Be and 3.3 μm thick PP considerably have low transmittance at $\lambda \geq 10$ Å.

With respect to the spike noise blocking, a few experiments have been reported on energy loss of the neutral hydrogen (H^0) in solid targets at the kinetic energy range of 10–180 keV. The results show that the stopping power of solid targets for H^0 is roughly half compared to that for proton [27, 28]. Figure 2.10(b) shows the projected depth of protons along the incident direction as a function of proton energy. The energy of p-NBI (40 keV) and n-NBI (180 keV) is denoted by two vertical dashed lines. The projected depth of proton at p-NBI energy is smaller than the thickness of prepared three filters. Therefore, we reasonably expect that all the filters can efficiently block the high-energy particle from p-NBI. On the contrary, the projected depth at the n-NBI energy is much longer. The projected depth is 2.2 μm, 1.8 μm and 1.6 μm for PP, PET and Be, respectively. Even in this case, the 11 μm thick Be and 3.3 μm thick PP can sufficiently block the high-energy particle from n-NBI. In the case of the 0.5 μm PET filter, however, the result is not straightforward because the

projected depth is longer than the thickness. It seems that the PET filter is useful only in the low energy region, e.g., $E_p \leq 50$ keV. If the stopping power of neutral hydrogen is smaller than that of proton, the threshold energy to block the high-energy particle for the PET filter may be reduced. On the other hand, the elastic scattering of neutral hydrogen in the solid material effectively contributes to the spike noise reduction. If the high-energy particle changes the incident angle in the filter, it cannot reach the grating because the effective size of the grating in the present EUV spectrometer (46 mm × tan(90° - 86.6°) = 1.1 mm, where 46 mm is the grating size) is entirely small due to the large angle of incidence. Even if the angle change of the high-energy particle in the filter is very small, the effect may be not negligible.

Figures 2.11(b), (c) and (d) show the space-resolved spectral image measured with 11 μm thick Be, 3.3 μm PP and 0.5 μm PET filters in NBI discharges at $n_e = 2 \times 10^{13}$ cm^{-3}, respectively. Figures 2.11(a) and (e) show the image without filter after

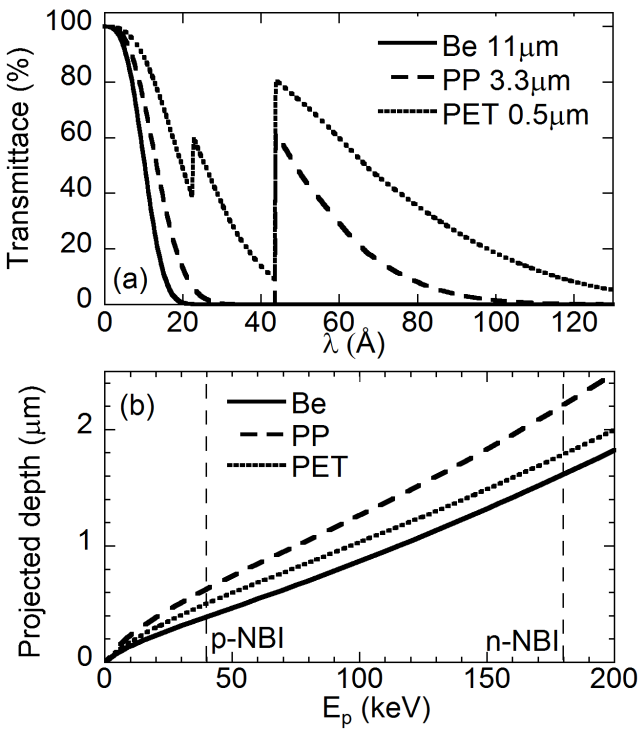

Fig. 2.10 (a) Percentage transmittance of three filters as a function of wavelength; solid line: 11 μm thick Be, dash line: 3.3 μm thick PP and dotted line: 0.5 μm thick PET. (b) Projected depth curves of Be, PET and PP as a function of incident proton energy. Vertical dashed lines denote the injection energy of perpendicular p-NBI and tangential n-NBI.

switching off the NBI (post- NBI) and during NBI, respectively. Seeing Fig. 2.11(e), we can understand that the NBI spike noise distributes all over the CCD position and strongly blurs the spectrum image. On the contrary, the spike noise completely disappears from the image, when the NBI is switched off (see Fig. 2.11(a)). Since the Be and PP filters can sufficiently block all the high-energy particles coming at the spectrometer, the spike noise fully vanishes from the images (see Figs. 2.11(b) and (c)). However, we notice that the spectral intensity is also weakened by the filters. When the two images of Figs. 2.11(b) and (c) are compared with Fig. 2.11(a), it is very clear. In the case of the PET filter, on the other hand, the result is clearly different from those mentioned above. When the image with PET filter in Fig. 2.11(d) is compared to Fig. 2.11 (a), we find that the two images of Figs. 2.11(a) and (d) seem to be identical, although a few spike noises are still appeared in Fig. 2.11(d).

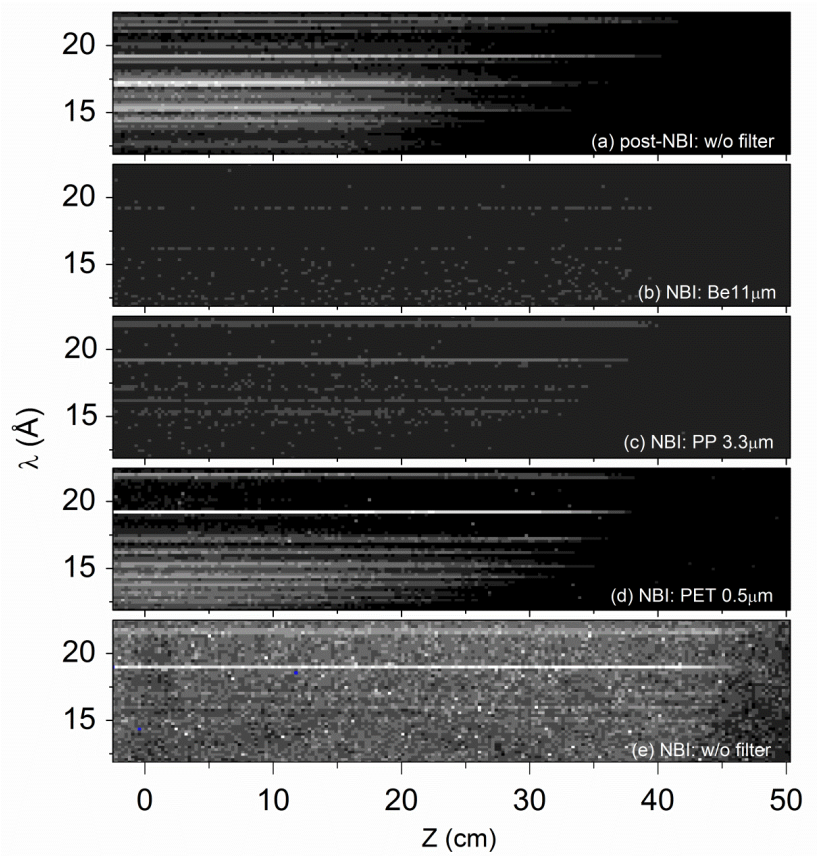

Fig. 2.11 CCD images of the EUV spectrometer from NBI discharges at $n_e = 2 \times 10^{13}$ cm^{-3} with different conditions; (a) after switching off NBI (post-NBI) without filter, (b) during NBI with 11 μm Be, (c) during NBI with 3.3 μm PP, (d) during NBI with 0.5 μm PET and (e) during NBI without filter.

The EUV spectra against wavelength in the range of 10–130Å are composed of space-resolved spectra measured from successive discharges. The result is shown in Fig. 2.12 with the same form as Fig. 2.11. When the EUV spectrum without filter is compared between Fig. 2.12(a) after switching off NBI and Fig. 2.12(e) during NBI, we understand again that the spike noise gives a serious damage to the spectrum (see a large base line in Fig. 2.12(e)). Here, we should notice that the exposure time in Fig. 2.12 for the space-resolved measurement (127ms) is much longer than that in Fig. 2.7

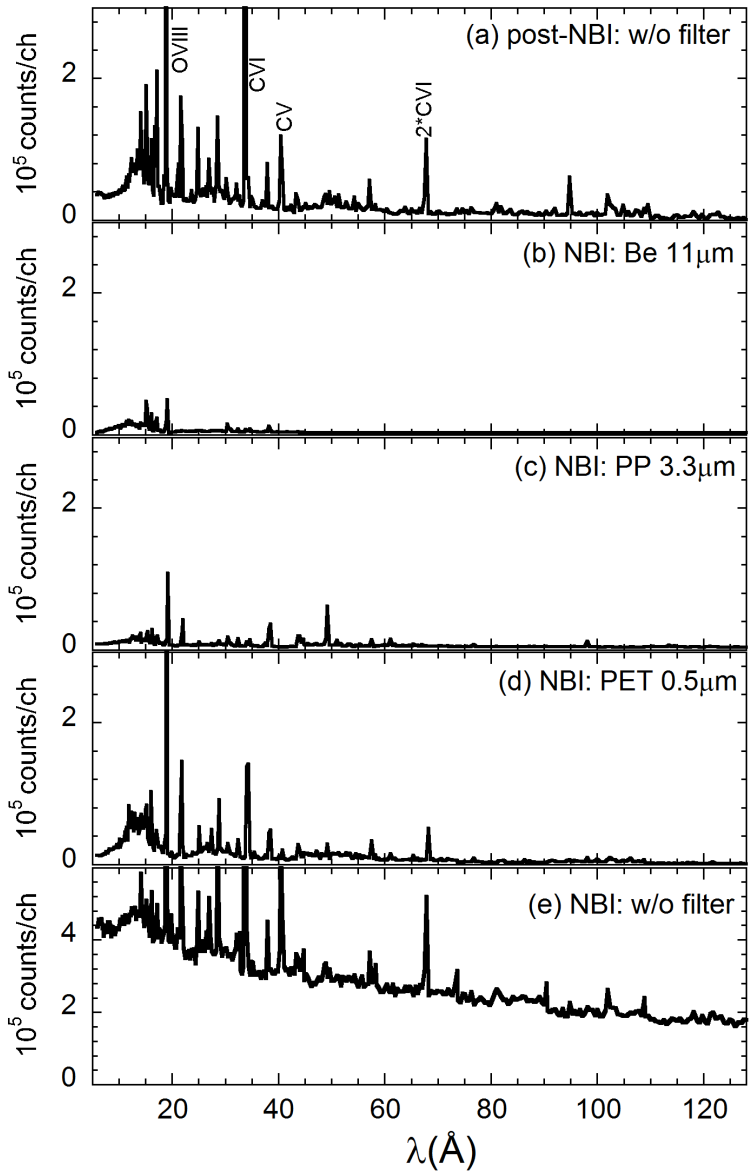

Fig. 2.12 EUV spectra from NBI discharges at $n_e = 2 \times 10^{13}$ cm^{-3} with different conditions; (a) after switching off NBI (post-NBI) without filter, (b) during NBI with 11 μm Be, (c) during NBI with 3.3 μm PP, (d) during NBI with 0.5 μm PET and (e) during NBI without filter.

without spatial resolution (5 ms). In addition, the signals in Fig. 2.12 are integrated along long axis (1024 pixels) of the CCD, while the signals in Fig. 2.7 are integrated along short axis (255 pixels) of the CCD. Therefore, the spike noise in Fig. 2.12 entirely averaged among the CCD pixels forms a continuous background emission, while the background emission in Fig. 2.7 is fluctuating due to relatively small number of the spike noises. The signal intensity is much reduced in cases of the Be and PP filters (see Figs. 2.12(b) and (c)) as described above, whereas the spike noise can be fully deleted from the spectrum. In contrast to it, the spectrum with PET filter plotted in Fig. 2.12(d) is very similar to Fig. 2.12(a) without NBI. The result also indicates that the PET filter can keep a sufficient signal level.

The filter response mentioned above is also verified from pulse height distribution of the spike noise. The result is shown in Fig. 2.13. The pulse height distribution is analyzed with a manner similar to Fig. 2.9(c), while the background noise emission with small pulse height is not subtracted due to the lack of data.

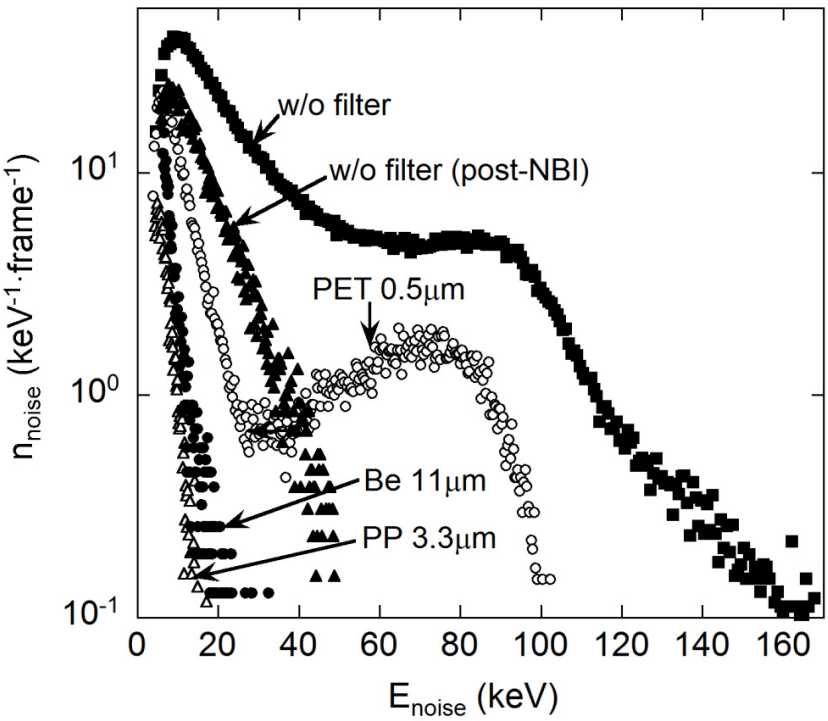

Fig. 2.13 Pulse height distributions of spike noise with different conditions; solid squares: during NBI without filter, solid triangles: after switching off NBI (post-NBI) without filter, open circles: during NBI with 0.5 μm PET, solid circles: during NBI with 11 μm Be and open triangles: during NBI with 3.3 μm PP.

Instead, the pulse height distribution after switching off the NBIs is referred as the background noise. All of the data are obtained in similar plasma conditions at n_e = 2–3 × 10^{13} cm^{-3}. High-energy particles from both the n- and p-NBIs are included in all distributions of Fig. 2.13 except for the reference distribution denoted with post-NBI. The pulse height distribution without filter (solid squares) is fully composed of the spike noise from high-energy n-NBI and low-energy p-NBI. The spike noise at high energies, e.g. $E_{noise} \geq 100$ keV, scarcely contributes to the total noise counts. When the NBIs are switched off, the spike noise with high energies of $E_{noise} \geq 50$ keV is mostly disappeared (see solid triangles: post-NBI). When the PP and Be filters are used, the noise counts are reduced much lower than the level of post-NBI in addition to the signal counts. This result also confirms the low transmittance and the high stopping power of the 11 μm PP and 3.3 μm Be filters as indicated in Fig. 2.10.

The pulse height distribution with the PET filter is quite different from other distributions, expressing a notable plateau between 40 and 100 keV, which is a little

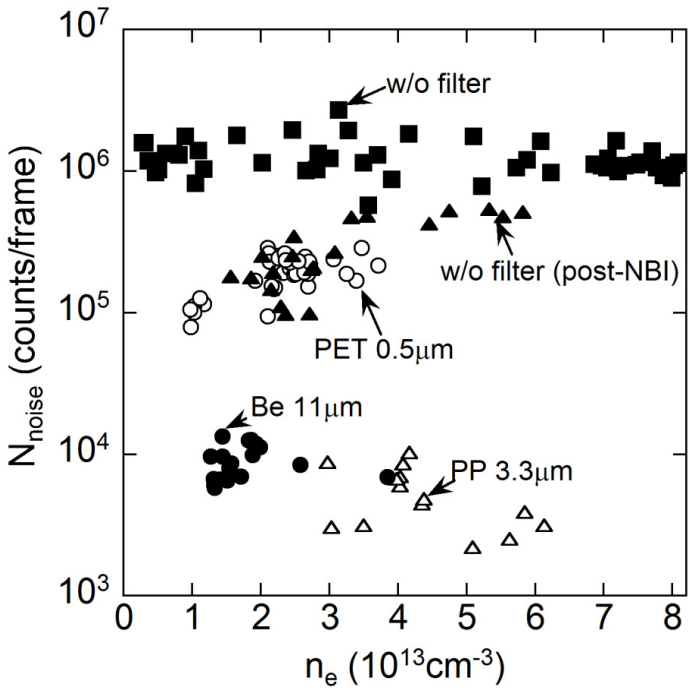

Fig. 2.14 Total Noise counts per CCD frame with different conditions; closed squares: during NBI without filter, solid triangles: after switching off NBI (post-NBI) without filter, open circles: during NBI with 0.5 μm PET, solid circles: during NBI with 11 μm Be and open triangles: during NBI with 3.3 μm PP.

similar to the plateau seen in the case without NBI (solid squares: $50 \leq E_{noise} \leq 100$ keV). Although it is not easy to understand this plateau, it probably reflects both the effects on the scattering in the filter and slowing down processes of high-energy ions confined in the plasma including charge-exchange collision with slow neutrals. The residual spike noise in the high-energy range of $30 \leq E_{noise} \leq 100$keV can be easily discriminated and deleted from the spectral image shown in Fig. 2.11(d) based on the software signal processing. The noise count with PET filter in the low energy range of $E_{noise} \leq 30$ keV is significantly lower than that from the post-NBI case without filter. The result implies that the signal intensity clearly decreases even if the 0.5 μm thick PET filter is used.

The total noise count integrated over the energy is analyzed as a function of electron density, as shown in Fig. 2.14. In the case without filter (solid squares) the total noise count does not depend on the density and keeps a constant value, while the total noise count in the post-NBI case (solid triangles) reflecting the background noise emission from plasmas increases with density. Consequently, the noise due to high-energy particles decreases with density. This result is fairly reasonable because the high-energy ion density determined by the slowing down time is inversely proportional to the electron density. For the PET filter case (open circles), the total noise count overlaps with the post-NBI case at the density range of $n_e = 2–3 \times 10^{13}$ cm^{-3}, whereas the pulse height distribution is entirely different each other as shown in Fig. 2.13. Therefore, it is concluded that the total noise count can be reduced in one order of magnitude, when the 0.5 μm thick PET filter is used. In the Be and PP filter cases the noise count is at least two orders of magnitude less than the NBI noise without filter, but the signal count is also much reduced as described before.

2.4 Vertical profiles of continuum and line emissions

2.4.1 Bremsstrahlung profiles

Bremsstrahlung vertical profile is measured at $\lambda = 18.2$ Å with a filter in NBI discharges at $n_e = 2.5 \times 10^{13}$ cm^{-3}, as shown in Fig. 2.15(a). The error bars denote certain data scattering amplitude in the profile. The profile without filter obtained

from NBI discharge (dotted line) is distorted by the spike noise which unreasonably gives rise to a large intensity in the plasma edge. It evidently points out urgent necessity of the filter in measuring the bremsstrahlung continuum with the EUV spectrometer. The bremsstrahlung continuum measured with the PET filter (solid line) expresses a reasonable profile with sufficient intensity, while the result from the post-NBI case without filter (long-dashed line) shows a little large intensity compared

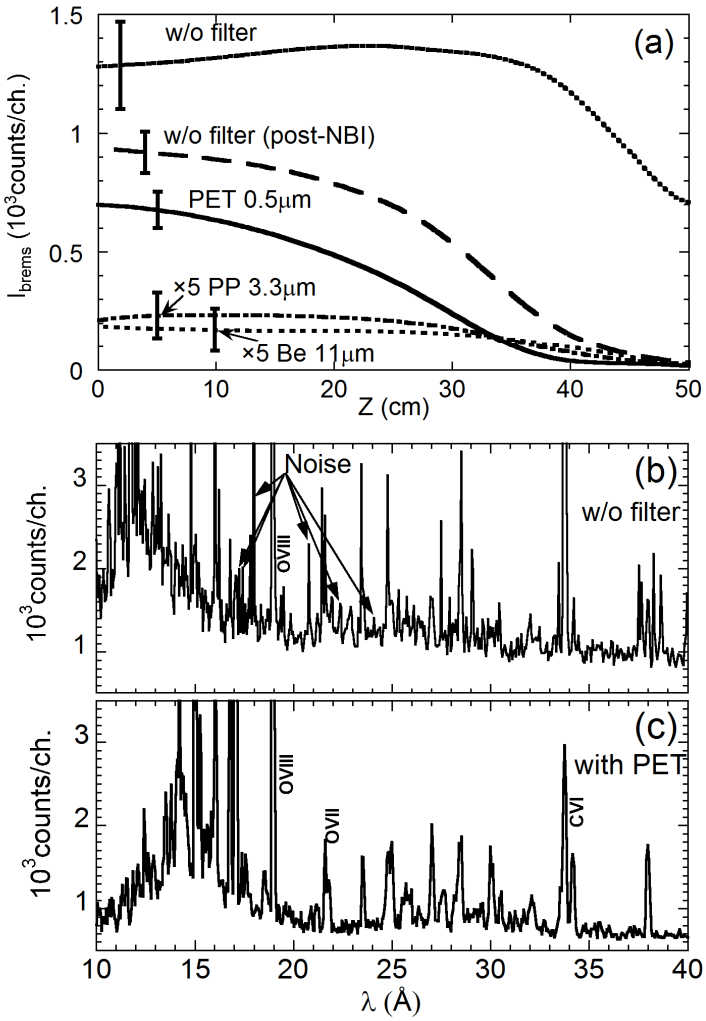

Fig. 2.15 (a) Line-integrated bremsstrahlung profiles measured at 18.2 Å in NBI discharges with n_e = 2.5 × 10^{13} cm^{-3} as a function of vertical position; dotted line: during NBI without filter, long-dashed line: after switching off NBI (post-NBI) without filter, solid line: during NBI with 0.5 μm PET, short-dashed line: during NBI with 11 μm Be and dashed-dotted line: during NBI with 3.3 μm PP and EUV spectra (b) without filter and (c) with PET filter.

to the PET case. In cases of the 3.3 μm PP (dashed-dotted line) and 11 μm Be filter (short-dashed line) the application to the bremsstrahlung profile measurement seems to be difficult due to extremely weak signal intensity. The spectra measured without filter and with PET filter are also plotted in wavelength range of 10–40 Å in Figs. 2.15(b) and (c), respectively. When the filter is not used, the bremsstrahlung continuum is considerably blurred not only by high-energy neutral particles but also low-energy neutral particles, as described in section 3.1. The PET filter can clearly reduce both types of the noise exhibiting a high-quality bremsstrahlung continuum. Therefore, we conclude that the use of the 0.5 μm PET filter for the bremsstrahlung profile measurement is the best choice in the present study.

When we measure the bremsstrahlung continuum in the EUV range, we have to carefully examine an exact wavelength interval free of impurity lines. In order to identify a good wavelength window for the bremsstrahlung measurement, the experimental profile is compared with the theoretical one calculated with temperature and density profiles from Thomson scattering diagnostic. The result is shown in Fig. 2.16. In the calculation a radially constant Z_{eff} profile is assumed [29]. The bremsstrahlung profile calculated at 20.0 Å is normalized to the experimental data from low- and high-density discharges, i.e., $n_{\mathrm{e}} = 2.9 \times 10^{13}\ \mathrm{cm}^{-3}$ and $13.3 \times 10^{13}\ \mathrm{cm}^{-3}$. The experimental profile well agrees with the calculated profile for both the density ranges.

In the wavelength range of 10–90 Å where the bremsstrahlung intensity is sufficiently strong for the observation, we finally determine possible wavelength windows for the bremsstrahlung profile measurement based on the present EUV spectrometer system with the PET 0.5 μm thick filter. The results are summarized as follows;

16.5 Å $\leq \lambda \leq$ 16.6 Å, 17.9 Å $\leq \lambda \leq$ 18.4 Å, 19.9 Å $\leq \lambda \leq$ 20.7 Å, 20.9 Å $\leq \lambda \leq$ 21.0 Å, 21.3 Å $\leq \lambda \leq$ 21.5 Å, 21.9 Å $\leq \lambda \leq$ 23.2 Å, 23.5 Å $\leq \lambda \leq$ 24.7 Å, 27.2 Å $\leq \lambda \leq$ 27.4 Å, 27.8 Å $\leq \lambda \leq$ 28.0 Å, 29.2 Å $\leq \lambda \leq$ 29.8 Å, 32.9 Å $\leq \lambda \leq$ 33.2 Å, 35.8 Å $\leq \lambda \leq$ 33.6 Å, 41.1 Å $\leq \lambda \leq$ 41.5 Å, 42.6 Å $\leq \lambda \leq$ 43.0 Å, 43.8 Å $\leq \lambda \leq$ 48.3 Å, 48.8 Å $\leq \lambda \leq$ 53.6 Å, 54.8 Å $\leq \lambda \leq$ 56.5 Å, 57.2 Å $\leq \lambda \leq$ 60.1 Å, 61.4 Å $\leq \lambda \leq$ 62.6 Å, 70.4 Å $\leq \lambda \leq$ 73.1 Å, 77.2 Å $\leq \lambda \leq$ 79.0 Å, 83.9 Å $\leq \lambda \leq$ 85.5 Å and 88.1 Å $\leq \lambda \leq$ 89.9 Å.

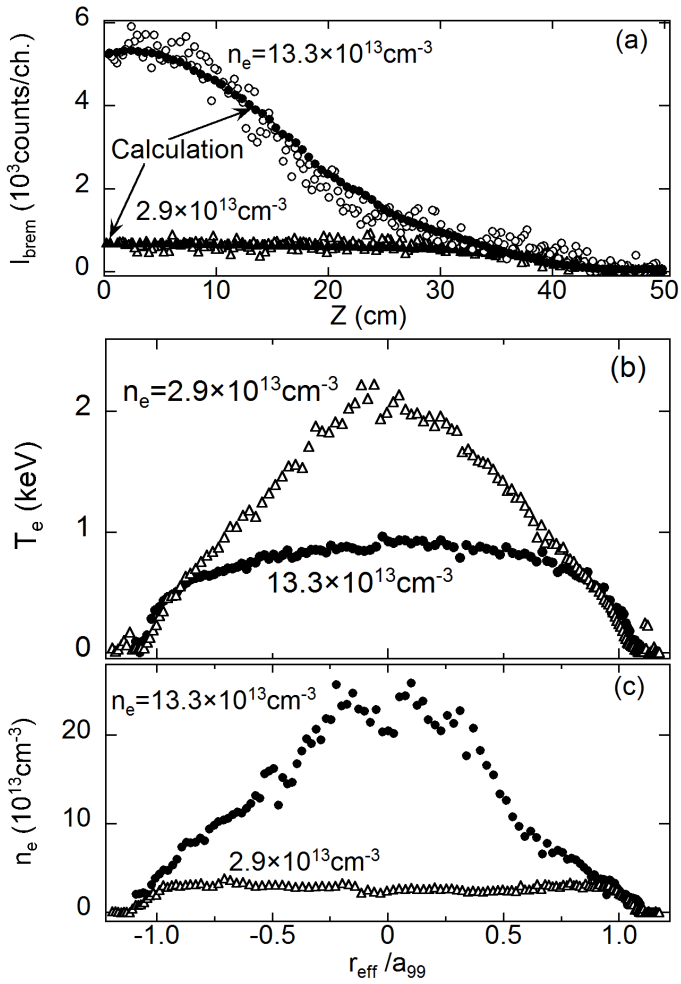

Fig. 2.16 (a) Vertical profiles of bremsstrahlung continuum at 20 Å at n_e = 13.3 × 10^{13} cm^{-3} (open circles: measurement, closed circles: calculation) and 2.9 × 10^{13} cm^{-3} (open triangles: measurement, closed triangles: calculation), (b) T_e (open triangles: n_e = 2.9 × 10^{13} cm^{-3} and closed circles: n_e = 13.3 × 10^{13} cm^{-3}) and (c) n_e (open triangles: n_e = 2.9 × 10^{13} cm^{-3} and closed circles: n_e = 13.3 × 10^{13} cm^{-3}) profiles as a function of averaged plasma radius, r_{eff}, normalized to averaged plasma radius, a_{99}.

2.4.2 Spectrum and profiles of Fe L_α transitions

Iron spectrum with n = 3–2 L_α transitions between 10 and 20 Å has been measured by injecting an iron impurity pellet [30]. A typical result is shown in Fig. 2.17. A lot of L_α transitions from highly ionized Fe ions are observed in the spectrum. Since several Fe lines are blended with other Fe lines at several wavelength intervals,

the spectrum appears with structure like pseudo continuum. In particular, it is enhanced in the wavelength range of 12–16 Å. The reason may be caused by a lack of the spectral resolution. It is often hard to distinguish the spectral line individually. Nevertheless, the ionization stage of Fe L_α transitions basically increases step-by-step when the wavelength decreases from 20 Å to 10 Å. The resultant spectrum at such a narrow wavelength interval then exhibits Fe transitions in a variety of ionization stages of Ne-like to Li-like ions, i.e., FeXVII to FeXXIV.

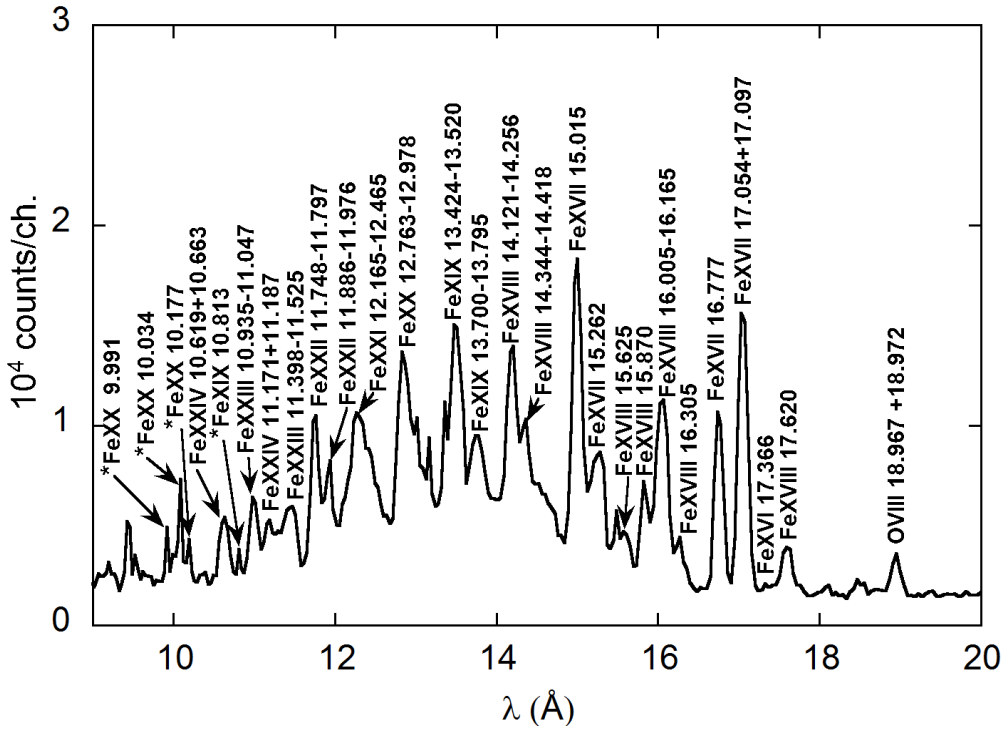

Fig. 2.17 Fe n = 3–2 L_α spectrum below 20 Å measured after an iron impurity pellet injection. The asterisks (*) before wavelengths, denote that two or more lines are blended into the same wavelength position.

The line-integrated vertical profile of the Fe L_α transition from FeXVII to FeXXIV is analyzed by carefully choosing the wavelength interval at each ionization stage. The result is shown in Fig. 2.18(a). The electron density and temperature profiles are also shown in Fig. 2.18(b) of which the coordinate is converted into the vertical position at horizontally elongated plasma cross section by taking into account the elliptical magnetic surface calculated with VMEC code. The vertical profiles are normalized at each peak position. The peak position of each profile moves inside with increasing the ionization stage, reflecting the centrally peaked electron

temperature profile. The FeXXIII and FeXXIV indicate an almost flat profile in the vicinity of plasma center reflecting a hollow iron density profile.

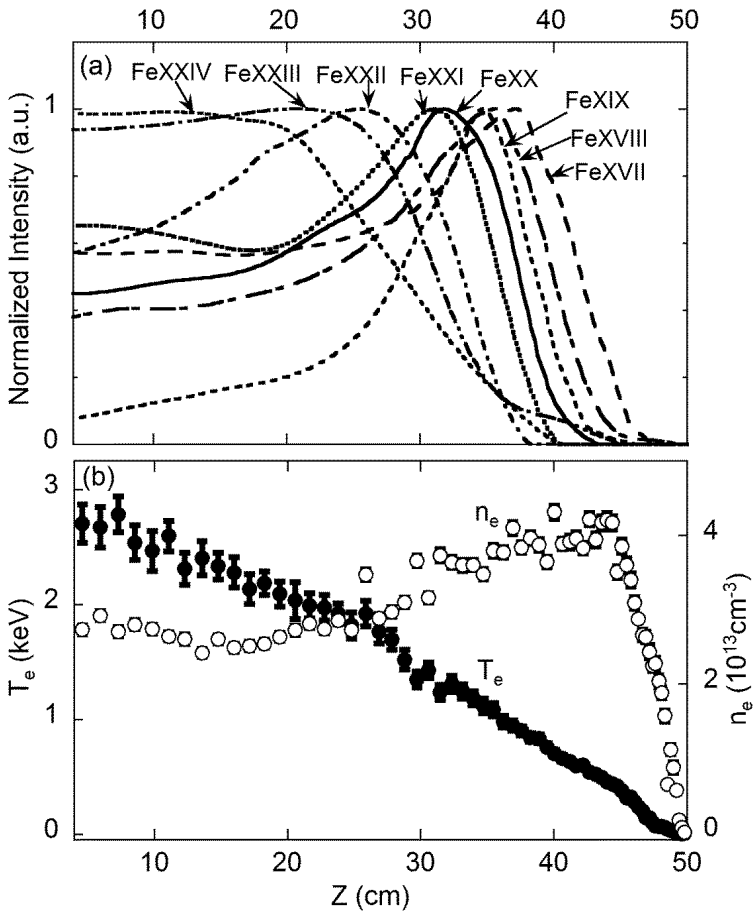

Fig. 2.18 (a) Line-integrated vertical intensity profiles of FeXVII (17.054 Å & 17.097 Å), FeXVIII (14.121–14.256 Å), FeXIX (13.424–13.520 Å), FeXX (12.763–12.978 Å), FeXXI (12.165–12.465 Å), FeXXII (11.748–11.797 Å), FeXXIII (10.935–11.047 Å) and FeXXIV (10.619 Å & 10.663 Å) and (b) electron temperature (closed circles) and density (open circles) profiles.

Since many lines appear in the wavelength range of 10–130 Å, the line identification is often difficult, even if the line is theoretically predicted in the wavelength list. If the radial profile measurement is applied to the line identification, the spectrum identification is really reliable. For instance, several lines are predicted in the vicinity of 17.6 Å as L_α transitions of FeXV, FeXVI and FeXVIII. In order to identify the transition at 17.6 Å in Fig. 2.17, the vertical profile is compared with profiles of L_α Fe transitions in neighboring ionization stages of FeXVII, FeXVIII and

FeXIX which have been already identified. The result is plotted in Fig. 2.19. From the figure we can clearly understand that the vertical profile of the line emission at 17.6 Å is identical to that of FeXVIII (14.121–14.256 Å). The line emission at 17.6 Å is thus determined as the FeXVIII at 17.62 Å, of which the transition is $2s^2 2p^4 3p\ ^2P_{3/2}$ $-2s^2 p^6\ ^2S_{1/2}$ [31]. The L_α transitions shown in Fig. 2.17 are identified based on this technique.

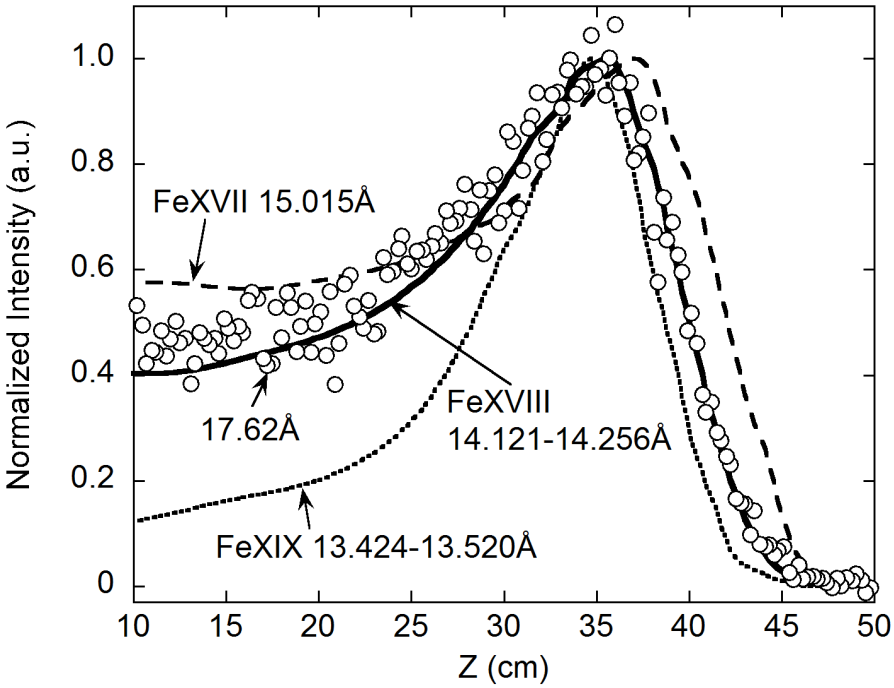

Fig. 2.19 Line-integrated vertical intensity profiles of unknown spectral line at 17.62 Å, FeXVII (15.015 Å), FeXVIII (14.121–14.256 Å) and FeXIX (13.424–13.520 Å). The unknown line can be identified by comparing with other three spectral lines which are already identified.

2.5 Summary

A space-resolved extreme ultraviolet (EUV) spectrometer working in wavelength range of 10–130 Å has been developed to measure vertical profiles of bremsstrahlung continuum and impurity line emissions at horizontally elongated plasma cross section on LHD. The spectrometer has a spectral resolution of 0.15 Å at 30 Å when 100 μm width entrance slit is used. The spatial resolution in the vertical direction is sufficiently good, i.e., approximately 30 mm, when a 1 mm width spatial-resolution

slit is used. The spatial resolution in the toroidal direction is also good, i.e., 22 mm. The spectral intensity of the present system is absolutely calibrated based on the profile measurement of visible and EUV bremsstrahlung continuum. The resultantly observed constant calibration factor along the grating groove shows a constant reflectivity of the EUV emissions. These results obtained here indicate a sufficient performance for the profile measurement.

High-energy neutral particles originating in NBI give rise to a large amount of spike noise on the EUV spectroscopy, especially in low-density discharges. A holographic grating used in the present spectrometer causes more spike noises compared to a ruled grating. It is probably due to a geometric difference in the groove structure of rectangular shape for holographic grating and triangle shape for ruled grating. The pulse height distribution analysis on the spike noise definitely concludes that the spike noise is composed of high-energy neutral particles attributed to 180 keV n-NBIs and 40 keV p-NBIs.

Three filters of 0.5 μm thick PET, 3.3 μm thick PP and 11 μm thick Be have been tested to reduce the spike noise. The 11 μm Be and the 3.3 μm PP filters entirely eliminate all the spike noises, but the signal intensity is also significantly reduced. The 0.5 μm PET filter fully eliminates low-energy neutral particles originating in the p-NBIs, while high-energy neutral particles from the n-NBIs cannot be sufficiently blocked. However, the spike noise remaining in the EUV spectrum can be deleted by the software data processing. The 0.5 μm PET is then selected as the best filter for the bremsstrahlung profile measurement in the present EUV system. Based on the PET filter the bremsstrahlung profile has been successfully measured without spike noise at low-density discharges as well as the high-density discharges.

The Fe n = 3–2 L_α transition array in 10–20 Å is observed by injecting an iron impurity pellet. The vertical profile of Fe L_α transitions has been also successfully measured with several charge states, i.e., FeXVII-XXIV. The measured profile is applied to the line identification of the Fe L_α transition array. As an example of the method, the L_α transition of FeXVIII at 17.62 Å is reliably identified. The Fe L_α transition array measured with the present space-resolved EUV spectrometer system is thus accurately identified for the impurity transport study.

References

[1] K.Kadota, M.Otsuka and J.Fujita, Nucl. Fusion **20**, 209 (1980).

[2] H.Y.Zhou, S.Morita, M.Goto and C.F.Dong, J.Appl.Phys. **107**, 053306 (2010).

[3] E. Hinnov and M. Mattioli, Phys. Rev. A **66**, 109(1978).

[4] J. L. Schwob, A. W. Wouters, S. Suckewer and M. Finkenthal, Rev. Sci. Instrum. **58**, 1601(1987).

[5] R. J. Fonck, A. T. Ramsey and R. V. Yelle, Appl. Opt. **21**, 2115(1982).

[6] T. Kawachi, H. Suemitsu, K. Sawada, T. Fujimoto, T. Maehara, S. Yoshimura, T. Maekawa and Y. Terumichi, Rev. Sci. Instrum. **66**, 1042(1995).

[7] P. Beiersdorfer, M. Bitter, L. Roquemore, J. K. Lepson and M.-F. Cu, Rev. Sci. Instrum., **77**, 10F306 (2006).

[8] P. Beiersdorfer, J. K. Lepson, M. Bitter, K. W. Hill and L. Roquemore, Rev. Sci. Instrum. **79**, 10E318 (2008).

[9] Z. Cui, S. Morita, B. Fu, Y. Huang, P. Sun, Y. Gao, Y. Xu, C. Dong, P. Lu, Q. Wang, X. Ding, Q. Yang and X. Duan, Rev. Sci. Instrum. **81**, 043503 (2010).

[10] M. Yoshikawa, Y. Okamoto, E. Kawamori, Y. Watanabe, C. Watabe, N. Yamaguchi and T. Tamano, Nuclear Instruments and Methods in Physics Research Section A: Accelerators, Spectrometers, Detectors and Associated Equipment **467–468**, 1533 (2001).

[11] W. Biel, G. Bertschinger, R. Burhenn, R. Konig and E. Jourdain, Rev. Sci. Instrum. **75**, 3268 (2004).

[12] Y. Shen, X. Du, W. Zhang, Q. Wang, Y. Li, J. Fu, F. Wang, J. Xu, B. Lu, Y. Shi and B. Wan, Nuclear Instruments and Methods in Physics Research Section A: Accelerators, Spectrometers, Detectors and Associated Equipment **700**, 86 (2013).

[13] C. Dong, S. Morita, M. Tokitani, M. Goto, H. Sakaue, E. Wang and H. Zushi, Rev. Sci. Instrum. **83**, 10D509 (2012).

[14] J. Roth, E. Tsitrone, T. Loarer, V. Philipps, S. Brezinsek, A. Loarte, G. F. Counsell, R. P. Doerner, K. Schmid, O. V. Ogorodnikova and R. A. Causey, Plasma Phys. Control. Fusion **50**, 103001 (2008).

[15] V. Philipps, Journal of Nuclear Materials **415**, S2 (2011).

[16] M. B. Chowdhuri, S. Morita and M. Goto, Appl. Opt. **47**, 135 (2008).

[17] C. Dong, S. Morita, M. Goto and H. Zhou, Rev. Sci. Instrum. **81**, 033107 (2010).
[18] M. B. Chowdhuri, S. Morita, M. Goto, H. Nishimura, K. Nagai and S. Fujioka, Rev. Sci. Instrum.**78**, 023501 (2007).
[19] M. Koike, T. Yamazaki and Y. Harada, Journal of Electron Spectroscopy and Related Phenomena, **101–103**, 913 (1999).
[20] C. Dong, S. Morita, M. Goto and E. Wang, Rev. Sci. Instrum. **82**, 113102 (2011).
[21] H. Y. Zhou, S. Morita, M. Goto and M. B. Chowdhuri, Rev. Sci. Instrum. **79**, 10F536 (2008).
[22] K. Narihara, I. Yamada, H. Hayashi and K. Yamauchi, Rev. Sci. Instrum. **72**, 1122 (2001).
[23] D. G. Hummer, The Astrophysical Journal **327**, 477 (1988).
[24] P. J. Storey and D. G. Hummer, Computer Physics Communications **66**, 129 (1991).
[25] H. Winter, Physics Reports **367**, 387 (2002).
[26] S. L. O'Dell, M. W. Bautz, J. Blackwell, Y. M. Butt, R. A. Cameron, R. F. Elsner, M. S. Gussenhoven, J. J. Kolodziejczak, J. I. Minow, R. M. Suggs, D. A. Swartz, A. F. Tennant, S. N. Virani and K. M. Warren, in Proceedings of SPIE **4140**, 99 (2000).
[27] S. K. Allison, J. Cuevas and M. Garcia-Munoz, Phys. Rev.**127**, 792 (1962).
[28] H. Ogawa, N. Sakamoto, I. Katayama, Y. Haruyama, M. Saito, K. Yoshida, M. Tosaki, Y. Susuki and K. Kimura, Phys. Rev. A **54**, 5027 (1996).
[29] H. Zhou, S. Morita, M. Goto, C. Dong, J. Yanagibayashi and M. Hasuo, Rev. Sci. Instrum. **81**, 10D706 (2010).
[30] R. Katai, S. Morita, M. Goto, H. Nishimura, K. Nagai and S. Fujioka, Jpn.J.Appl.Phys. **46**, 3667 (2007).
[31] J. J. Drake, D. A. Swartz, P. Beiersdorfer, G. V. Brown and S. M. Kahn, The Astrophysical Journal **521**, 839 (1999).

Chapter 3

Development of coaxial pellets for metallic impurity injection

3.1 Introduction

The study on tungsten (W) is an urgently important current topic in the fusion research, since the tungsten is adopted as a divertor material of the International Thermonuclear Experimental Reactor (ITER) [1]. Experiments on tungsten-seeded plasmas have been extensively carried out in many fusion devices [2–5] for studying the effect of tungsten material on the plasma performance. A comprehensive understanding of spectral structures and atomic processes in tungsten ions is then

strongly required to diagnose the tungsten behavior in high-temperature plasmas [6]. However, several tungsten spectra still remain unknown and the tungsten atomic database, in particular, recombination rates, are extremely inaccurate for use in the transport study. Therefore, spectral identification of tungsten emissions and reevaluation of atomic data related to tungsten ions based on the profile measurement are necessary for the tungsten transport study in the ITER. For the purpose a bright light source of tungsten is strongly desired for accurate data analysis.

In the study of tungsten on the Large Helical Device (LHD), an active method is necessary for introducing it into plasmas, e.g. laser blow-off. However, the laser blow-off technique seems to be impossible because of the existence of edge ergodic layer [7] by which the coming ablated particles are easily screened. Therefore, a method of impurity pellet injection has been adopted until now for the impurity study using a cylindrical pellet with sizes of 0.5–1.5 mm [8]. However, the discharge is easily terminated through radiative collapse, when a pure tungsten pellet with such a size is injected in the LHD plasma. Use of extremely small pellet is not easy due to several technical problems. A coaxial-structure pellet has been thus developed for the spectroscopic study of tungsten. As the first step a coaxial molybdenum pellet was tested. The LHD discharge could be excellently sustained after the injection [9]. In this paper, the result is presented on two different coaxial tungsten pellets with graphite carbon and polyethylene tubes. Analysis is also done on the pellet velocity and deposition.

3.2 Experimental setup

LHD is a superconducting fusion device based on continuously wound helical coils with toroidal and poloidal pitch numbers of $M = 10$ / $l = 2$. In the present study the plasma discharge is operated with major radius of $R = 3.6$ m and averaged minor radius of $a = 0.64$ m at magnetic field of $B_t = 2.75$ T. The discharge is sustained and heated by 180 keV tangential neutral beam injection (NBI).

The impurity pellet injector is installed on an outboard port (10-O) at horizontally elongated plasma cross section. The impurity pellet is accelerated by helium gas at a pressure of 12 atmospheres. The pellet is injected at the equatorial plane with an

angle of 12º from the normal to the toroidal magnetic field. The pellet velocity is measured by a time-of-flight technique at three pellet chambers for differential pumping [10]. Each chamber is composed of a He-Ne laser, two narrow rectangular slits and a photodiode. When a pellet passes the front of the narrow slit, a small dip in the laser signal is recorded. The pellet velocity is derived from the time interval between two dips in the signal.

In order to monitor the pellet ablation, emissions of H_α, CI and visible bremsstrahlung are measured with an interference filter along the pellet trajectory from the backside of the pellet injection port. The data processing is started after a trigger for the pellet injection with a sampling rate of 1 MHz.

3.3 Specifications of coaxial pellets

The pellet used in the present study consists of a tungsten wire and a cylindrical tube made of polyethylene (PE) or graphite carbon (C), as shown in Figs. 3.1 (a) and (b), respectively. The diameter of tungsten wire is 0.15 mm and the dimension of PE and C tubes is 0.6^L (length) × 0.6^ϕ (outer diameter) × 0.3^ϕ (inner diameter) and 0.7^L × 0.7^ϕ × 0.25^ϕ, respectively. The W-in-PE and W-in-C contain 7–8 × 10^{17} tungsten atoms.

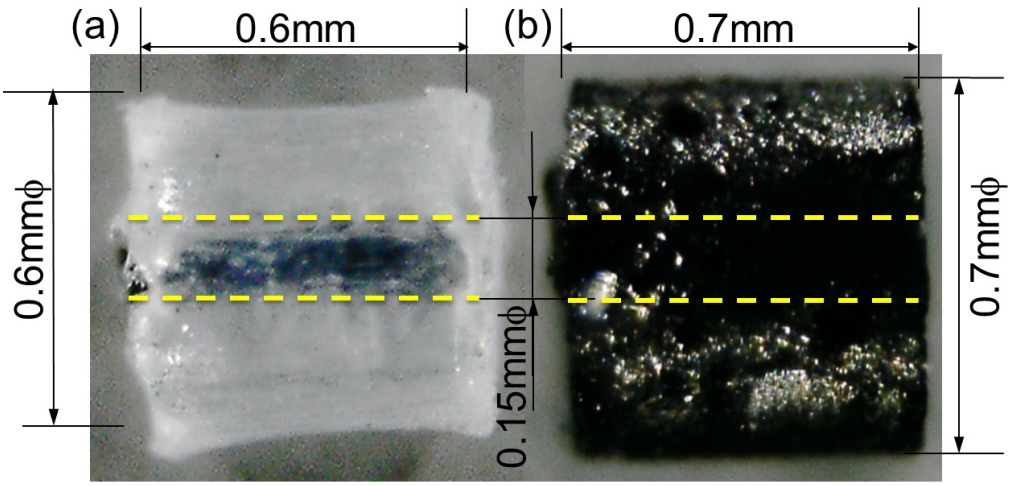

Fig. 3.1 Photos of (a) W-in-PE and (b) W-in-C coaxial pellets. The yellow dashed lines denote the position of tungsten wire.

Figure 3.2 shows velocity of the tungsten pellet against pellet mass. It also includes results from C tube, PE tube, Al-in-PE, Al-in-C, Fe-in-PE and Fe-in-C. The velocity tends to decrease with the mass. The W-in-PE velocity is then slightly higher than the W-in-C velocity. It may be interpreted by the acceleration of α_{pellet} (= F / m_{pellet}) at which the kinetic force is basically given by the pellet size and the helium gas pressure in addition to acceleration length.

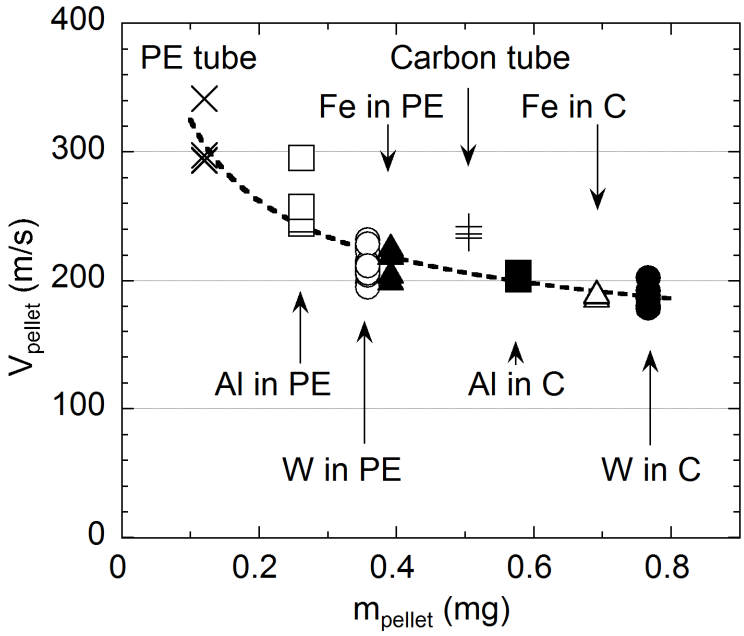

Fig. 3.2 Pellet velocity against pellet mass; W-in-PE (open circles), W-in-C (solid circles), Fe-in-PE (solid triangles), Fe-in-C (open triangles), Al-in-PE (open squares), Al-in-C (solid squares), PE tube (crosses) and C tube (plus signs). The dashed line denotes a polynomial fitting.

3.4 Experimental comparison between two pellets

3.4.1 Experimental result with different pellets

Typical waveforms of discharges with W-in-PE and W-in-C pellets are shown in Fig. 3.3. The discharges are maintained by two counter-close-wise NBIs (#1 and #3) and a close-wise NBI (#2). The tungsten pellet is injected at t = 5.5 s. After the injection the discharge with W-in-PE smoothly recovers with density increase of 1.8 ×

10^{13} cm^{-3}, whereas the discharge with W-in-C is terminated by the collapse just after the injection (see Figs. 3.3(c) and (d)). The WXXV at 32.3 Å with 5g–4f transition [4] is clearly observed after the W-in-PE injection (see Fig. 3.3(g)). In the discharge with W-in-C, the WXXV and CVI lines only display a sharp peak at the injection. The small signal after the plasma collapse is due to high-energy neutral particles from NBI [11].

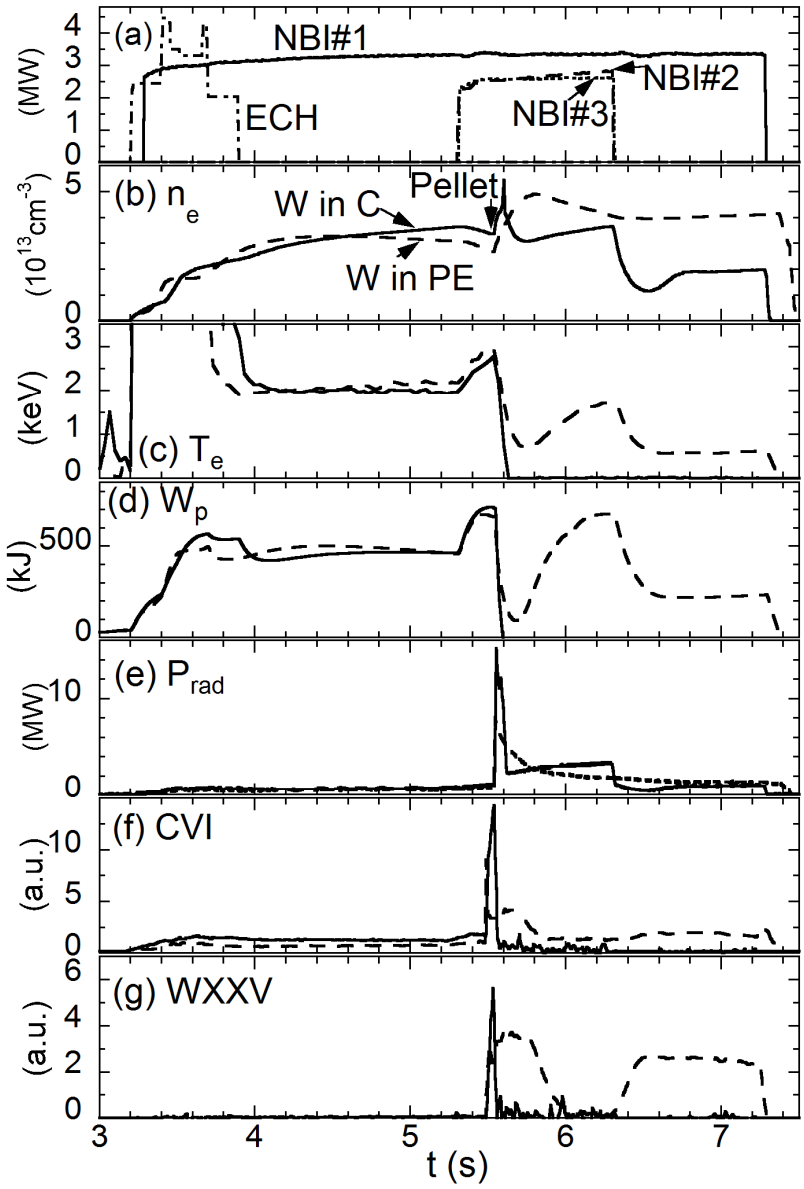

Fig. 3.3 Waveform of discharges with W-in-PE (dash lines) and W-in-C (solid line) pellets; (a) ECH and NBI port-through power, (b) line-averaged electron density, (c) central electron temperature, (d) plasma stored energy, (e) radiation power, (f) CVI at 33.73 Å and (g) WXXV at 32.3 Å.

3.4.2 Pellet deposition analysis

Most discharges with W-in-PE can be sustained, but most discharges with W-in-C are terminated just after the injection. Such a clear difference can be explained by pellet deposition profile.

Figure 3.4(a) shows time evolution of H_α, visible bremsstrahlung and CI emissions observed along the path of W-in-PE pellet with velocity of 216 m/s. The time sequence of emissions is first converted into pellet movement distance assuming a constant velocity during the ablation. The distance is again converted into magnetic surface coordinate as indicated at upper abscissa in Fig. 3.4 (a). The H_α emission exhibits a wide ablation between ρ = 0.75 and 1.0 with a peak at ρ = 0.82, indicating the deposition range of PE tube surrounding the tungsten wire. The radial location of tungsten deposition is revealed by the narrow H_α peak at ρ = 0.72, which coincides with peaks of bremsstrahlung and CI emissions. Since the tungsten wire does not include any C atoms, the CI peak may originate in emissions of WI and/or WII in wavelength range of the CI filter. Since numerous tungsten lines appear in the visible range during the tungsten ablation, the intensity increase in three signals is caused by the tungsten visible line. The deposition layer of PE tube and tungsten wire is also verified by a time evolution of electron temperature (T_e) measured by electron cyclotron emission (ECE) diagnostic, as shown in Fig. 3.4(b). The ordinate indicates a relative change in T_e from the pellet trigger timing, t_0 = 5.503 s. At two H_α peaks the T_e gradient at ρ = 0.812 and ρ = 0.718 drastically changes, suggesting the pellet deposition layer, i.e. T_e at ρ = 0.892 rapidly decreases before T_e at ρ = 0.812 starts to drop. It means the pellet already starts to ablate before the H_α meets the peak intensity. The T_e value at ρ = 0.663 decreases with a constant decay time during the pellet ablation, suggesting no ablation occurs at ρ = 0.663. Therefore, the T_e evolution at four radii indicates the same result as the H_α behavior. It is thus confirmed that the PE tube is ablated first in the outer part of the plasma, $0.75 \leq \rho \leq 1.0$ and the tungsten wire is ablated in a narrow radial location around ρ = 0.72.

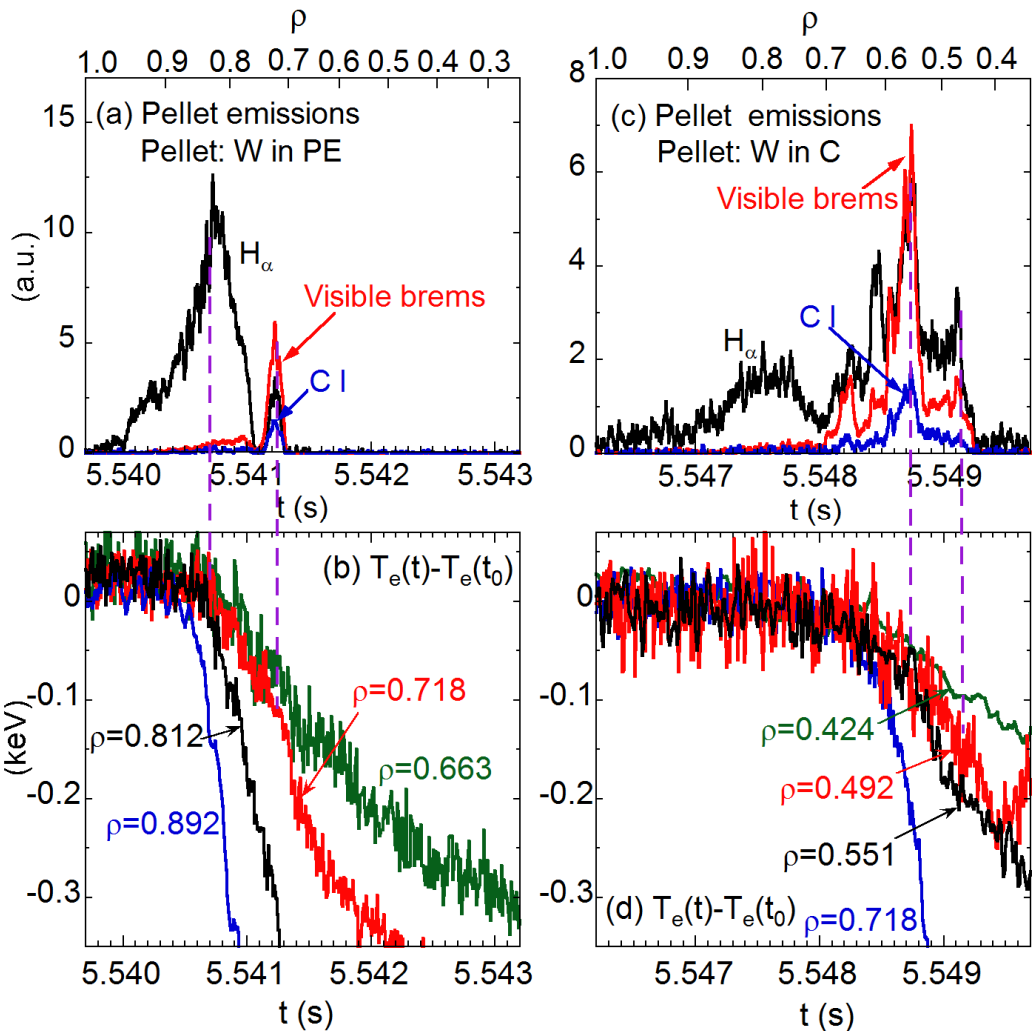

Fig. 3.4 Time behavior of visible emissions from (a) W-in-PE and (c) W-in-C and relative change in electron temperature of (b) W-in-PE and (d) W-in-C. Visible emissions are plotted for H_α (black solid line), CI (blue solid line) and bremsstrahlung (red solid line). Radial position at the upper abscissa in (a) and (c) is derived from velocity of W-in-C (190 m/s) and W-in-PE (216 m/s).

The time evolution of ablation light from W-in-C pellet with velocity of 190 m/s is shown in Fig. 3.4(c). The emission is widely distributed compared to W-in-PE case. It suggests a deeper penetration while the velocity is slower. The bump in the H_α profile at $0.7 \leq \rho \leq 0.9$ seems to reflect the ablation of adhesive consisting of hydrocarbon, which is used to fix the wire with the tube. Though it is not easy to interpret each peak in the range $0.53 \leq \rho \leq 0.70$, three peaks are at least a sign of

pellet ablation. The CI emission gradually increases until the pellet arrives at $\rho = 0.56$ and then sharply drops. The H_α and bremsstrahlung behave similarly to the CI emission. It is found that these time behaviors resemble closely those from C pellet without tungsten. After the C tube is fully ablated, the tungsten wire is exposed to plasmas and starts to ablate near $\rho \sim 0.53$. The ablation is completed at $\rho \sim 0.43$. As well as the analysis of T_e signals in Fig. 3.4(b), the time evolution of T_e shown in Fig. 3.4(d) also confirms the radial location of two H_α peaks indicated with dashed lines.

It is obvious that both the C and PE tubes are ablated before the tungsten wire is exposed to plasmas. Since the sublimation energy of carbon (7.5 eV per atom) is much higher than that of PE (0.08 eV per molecule [12]), the C tube can survive longer in plasmas and reach deeper position [13]. As a result, the tungsten in C can penetrate into deeper radius ($\rho = 0.43$) compared to that in PE ($\rho = 0.7$). When the tungsten is ablated in the plasma core, all the tungsten ions are confined and resultant radiation loss becomes really huge in a relatively small plasma volume in addition to the ionization loss. On the contrary, when the tungsten is ablated in the edge, the LHD plasma can decrease the plasma radius to minimize the edge cooling because helical plasmas have free boundary. The coaxial pellet with carbon tube can be probably applicable to lighter element such as Fe and Mo.

Increase in electron density for W-in-PE (Δn_{e_total}) and PE (Δn_{e_PE}) pellets measured from several discharges is listed in Table 3.1 against three wire diameters (ϕ_W) of 0.2, 0.15 and 0.1 mm. The density increase by tungsten ($\Delta n_{e,W}$) is much larger than that by PE tube ($\Delta n_{e,PE}$). The density increase is also calculated as $\Delta n_{e,W,cal.}$ and $\Delta n_{e,PE,cal}$ for tungsten and PE, respectively. The experimental value of $\Delta n_{e,W}$ is one order of magnitude larger than the calculated value of $\Delta n_{e,W,cal}$, while $\Delta n_{e,PE}$ is close to $\Delta n_{e,PE,cal}$. This strongly suggests that the reduced plasma radius due to the edge cooling deletes the edge particle screening [14] based on the presence of stochastic magnetic field layer and resultantly increases the edge particle confinement. If the wire diameter is below 0.05 mm, the density increase is estimated to be smaller than 1.0×10^{13} cm^{-3}, giving small perturbation to discharges. Here, it should be noticed that some tungsten EUV lines detected by CCD with exposure time of 5 ms is saturated when $\phi_W = 0.15$ and 0.20 mm pellets are injected. Therefore, the tungsten transport study is possible if we use the wire below $\phi_W = 0.05$ mm.

Table 3.1 Measured and calculated density increase for W-in-PE pellets in unit of 10^{13} cm^{-3} (*estimation).

ϕ_W(mm)	$\Delta n_{e,PE}$	$\Delta n_{e,PE,cal}$	$\Delta n_{e,W}$	$\Delta n_{e,W,cal}$	$\Delta n_{e,total}$
0.20	0.3 ± 0.2	0.1	2.3 ± 0.5	0.16	2.6 ± 0.5
0.15	0.3 ± 0.2	0.1	1.7 ± 0.3	0.09	2.0 ± 0.3
0.10	0.3 ± 0.2	0.1	1.3 ± 0.4	0.04	1.6 ± 0.4
0.05*	0.3 ± 0.2	0.1	0.7	0.01	1.0

3.5 W spectrum and profiles

Using coaxial tungsten pellets, several tungsten spectra have been measured and analyzed [4, 15, 16]. A typical tungsten spectrum is obtained with W-in-PE pellet using an extreme ultraviolet (EUV) spectrometer which monitors the spectra at 10–130 Å [17], as shown in Fig. 3.5(a). The spectrum consists of two pseudo-continuums in ranges of 14–40 Å and 45–70 Å and line emissions in ionization stages of W^{24+} to W^{33+}. The spectral structure between 15 and 35 Å can be well explained with spectra from a compact electron beam ion trap [4]. Identification of several tungsten line emissions in the range of 45–70 Å is given in another paper [16].

Figure 3.5(b) shows radial emissivity profiles of three spectral peaks, WXXV at 32.3 Å, WXXVI at 30.9 Å and WXXVII at 29.6 Å. The emissivity profile is calculated from line-integrated profile measured with a space-resolved EUV spectrometer [18] in time frame of t = 5.6–5.8 s. Corresponding T_e and n_e profiles measured by Thomson scattering are plotted in Fig. 3.5(c). Each emissivity profile can be used to estimate the tungsten ionization stage, assuming the intensity coefficient does not change much against the temperature. It is then clear that the ionization energy of W^{24+} (734.1 eV), W^{25+} (784.4 eV) and W^{26+} (833.4 eV) ions shows a good agreement with T_e.

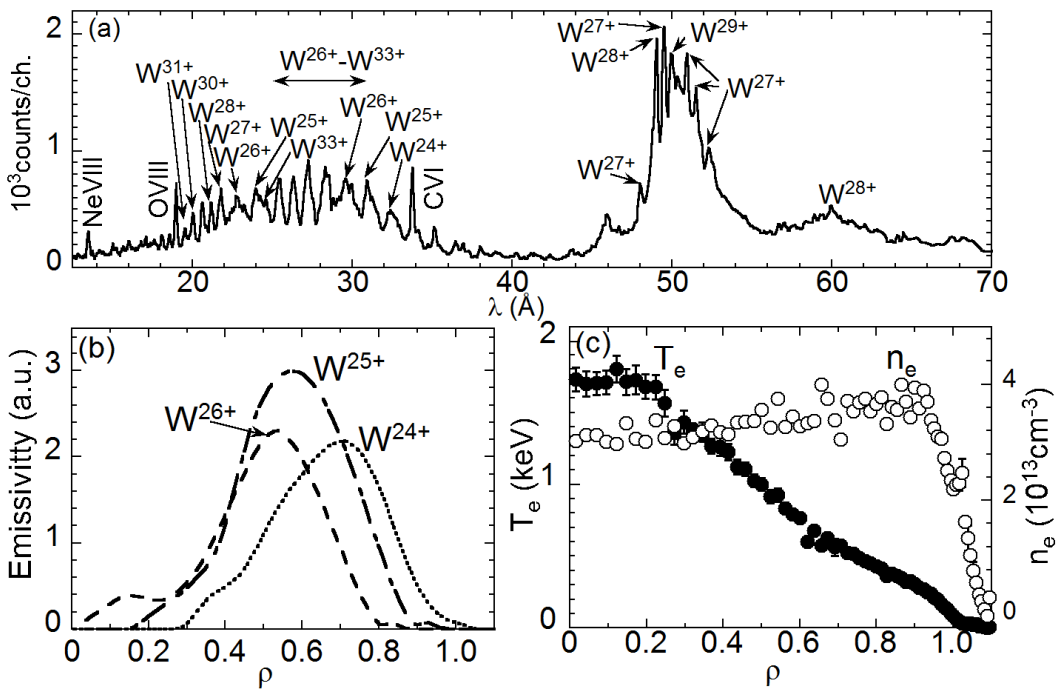

Fig. 3.5 (a) Tungsten spectrum between 12 and 70 Å, (b) radial emissivity profiles of WXXV at 32.3 Å (W^{24+}), WXXVI at 30.9 Å (W^{25+}) and WXXVII at 29.6 Å (W^{26+}) and (c) T_e and n_e profiles after W-in-PE injection.

3.6 Summary

Two types of coaxial pellets, W in PE and W in C, have been investigated in LHD for tungsten study. Experimental results show the W-in-PE pellet can avoid plasma collapse, whereas the W-in-C pellet usually terminates the discharge. The reason is clearly explained by the analysis of pellet deposition profile using pellet ablation spectroscopy with interference filters. Since carbon has a higher sublimation energy, the tungsten pellet can be delivered into deeper radial location (ρ = 0.43). It leads to a huge energy loss in the plasma core including radiation and ionization losses. On the contrary, as the W-in-PE pellet has a shallower penetration (ρ = 0.7), the energy loss is much smaller, suggesting some of tungsten ions are not confined. Then, the plasma can survive from the tungsten pellet injection. As a result, the W-in-PE pellet can excellently produce sufficient tungsten emissions in LHD. Several tungsten spectra

are thus measured with the W-in-PE pellet. Radial emissivity profiles of WXXV (32.3 Å), WXXVI (30.9 Å) and WXXVII (29.6 Å) are obtained, which are useful for future transport study.

References

[1] R. A. Pitts *et al*, Phys. Scr. **2009**, 014001 (2009).

[2] G. F. Matthews *et al.*, Phys. Scr. **2011**, 014001 (2011).

[3] R. Neu *et al.*, Plasma Phys. Control. Fusion **44**, 811 (2002).

[4] S. Morita *et al.*, AIP Conf. Proc. **1545**, 143 (2013).

[5] J. Clementson *et al.*, Rev. Sci. Instrum. **81**, 10E326 (2010).

[6] J. Clementson *et al.*, AIP Conf. Proc. **1525**, 78(2013).

[7] T. Morisaki *et al.*, J. Nucl. Mater. **313–316**, 548 (2003).

[8] H. Nozato *et al.*, Rev. Sci. Instrum. **74**, 2032 (2003).

[9] R. Katai *et al.*, Jpn. J. Appl. Phys. **46**, 3667 (2007).

[10] S. Morita *et al.*, Plasma Sci. Technol. **13**, 290 (2011).

[11] C. F. Dong *et al.*, Rev. Sci. Instrum. **83**, 10D509 (2012)

[12] F. W. Billmeyer, Jr., J. Appl. Phys. **28**, 1114 (1957).

[13] P. B. Parks, J.S. Leffler, and R.K. Fisher, Nucl. Fusion **28**, 477 (1988).

[14] S. Morita, *et al.*, Nucl. Fusion **53**, 093017 (2013).

[15] C. Suzuki *et al.*, J. Phys. B: At. Mol. Opt. Phys. **44**, 175004 (2011).

[16] M. B. Chowdhuri *et al.*, Plasma Fusion Res. **2**, S1060 (2007).

[17] M. B. Chowdhuri, S. Morita, and M. Goto, Appl. Opt. **47**, 135 (2008).

[18] X. L. Huang, *et al.*, Rev. Sci. Instrum. **85**, 043511 (2014).

Chapter 4

Spectral analysis on FeXVII *n* = 3–2 line emissions

4.1 Introduction

The Ne-like ion in the ionization balance of elemental iron is a dominant ionization state existing over a broad electron temperature range in both cosmic and laboratory plasmas due to its closed L shell atomic configuration. Therefore, the 3s–2p and the 3d–2p transitions of Ne-like iron (Fe^{16+}) in the wavelength range of 15–17 Å, which are prominent for diagnosing high-temperature plasmas, have been extensively analyzed in both astrophysical and laboratory plasma studies, including fusion plasma research [1–7]. A collisional-radiative (CR) model theoretically predicts that the intensities of FeXVII lines at 17.097 Å, 17.054 Å, and 16.777 Å

depend on not only electron temperature but also electron density. Therefore, the FeXVII lines with transitions of $n = 3$ to $n = 2$ called L_α transitions are very useful for measurements of the electron temperature [8], the electron density [5] and the ion abundance [1]. In addition to such diagnostics, the L_α transitions can be applied to the impurity transport study in fusion plasma research because their intensities are considerably strong [9]. In spite of this importance, however, the observed intensities of a few FeXVII lines have not been well interpreted using the C-R model. For example, the observed overall intensity of 3s–2p transitions is larger than the theoretically-predicted one when compared with the intensity of 3d–2p transitions [10]. A significant discrepancy between the observation and the calculation exists in the intensity of the 3d–2p transition at 15.015 Å [11]. Therefore, further investigation is necessary to explore the underlying physical processes related to the Ne-like FeXVII intensities.

4.2 Spectra and radial profiles of FeXVII *n* = 3–2 transitions

In the Large Helical Device (LHD), the Fe $n = 3$–2 L_α transition array composed of ionization stages of Ne-like Fe^{16+} to Li-like Fe^{23+} ions has been observed in the wavelength interval of 10–20 Å. Figure 4.1 shows typical spectra of the Fe L_α array for different electron temperatures. Several FeXVII lines have been identified from the spectra:

3C: 15.015 Å ($2p^5 3d\ ^1P_1 \rightarrow 2p^6\ ^1S_0$),
3D: 15.262Å ($2p^5 3d\ ^3D_1 \rightarrow 2p^6\ ^1S_0$),
3E: 15.450 Å ($2p^5 3d\ ^3P_1 \rightarrow 2p^6\ ^1S_0$),
3F: 16.777 Å ($2p^5 3s\ ^3P_1 \rightarrow 2p^6\ ^1S_0$),
3G: 17.054 Å ($2p^5 3s\ ^1P_1 \rightarrow 2p^6\ ^1S_0$) and
M2: 17.097 Å ($2p^5 3s\ ^3P_2 \rightarrow 2p^6\ ^1S_0$).

The 3G line is blended into the M2 line due to a limited spectral resolving power. The 3E line is usually weak in observations. The 3G+M2 and the 3C lines show the strongest intensities in the Fe L_α transition array. Very clearly Ne-like FeXVII dominates in the Fe $n = 3$–2 transition array when the electron temperature is low (see Fig. 4.1 (a)) whereas the Fe L_α lines from higher ionization stages, e.g., FeXXI, gradually become dominant over lines from lower ionization stages when the electron

temperature increases (see Figs. 4.1 (b) and (c)).

The vertical profiles of the FeXVII lines have been measured with a flat-field space-resolved extreme ultraviolet (EUV) spectrometer working in the wavelength range of 10–130 Å on the LHD [12]. The EUV spectrometer consisting of a slit, a holographic grating and a charged coupled device (CCD) detector is installed on a mid-plane spectrometer port at the backside of a rectangular vacuum extension chamber connected to a mid-plane LHD port. The observation chords of the spectrometer passing through a horizontal slit for spatial resolution which is placed between the grating and the entrance slit have a small upper elevation angle to

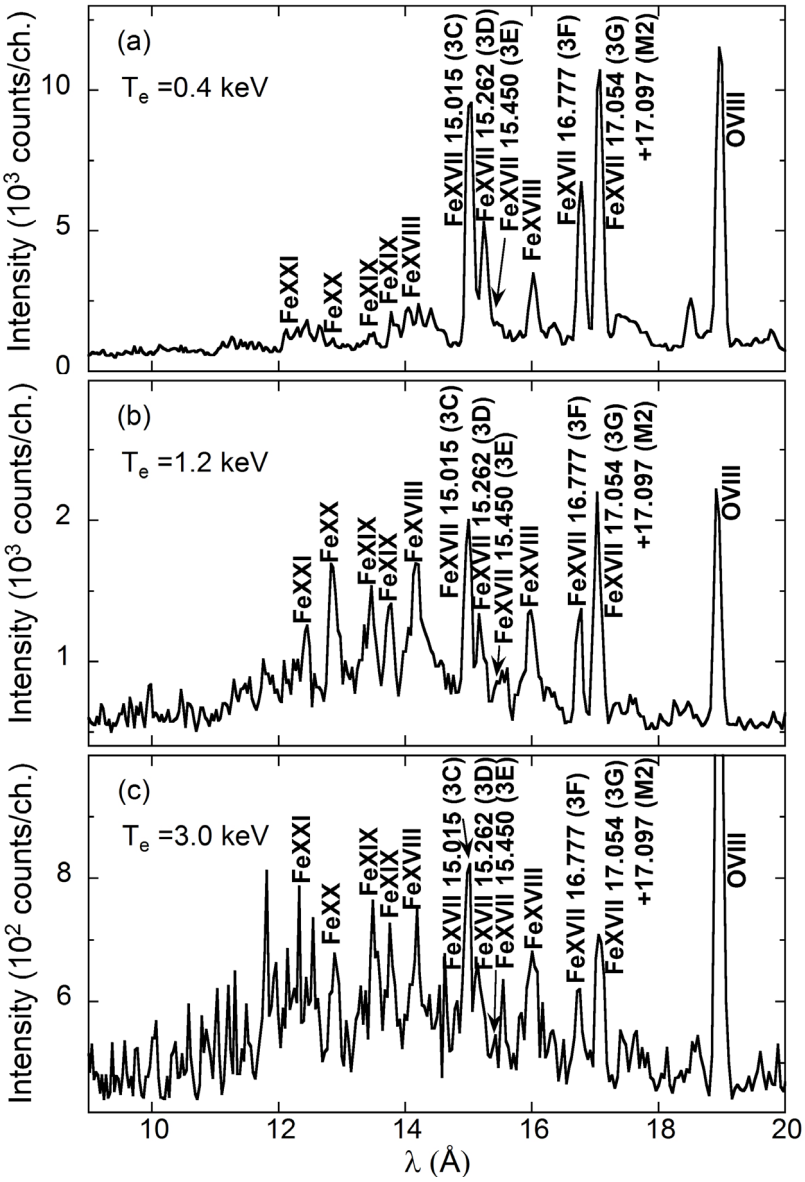

Fig. 4.1 EUV spectra of Fe n = 3–2 transitions in discharges with different electron temperatures: (a) 0.4 keV, (b) 1.2 keV and (c) 3.0 keV.

observe the vertical profile at the upper half (Z = 0–50 cm) of the horizontally-elongated plasma cross section. In the present study, the vertical profile is observed with a spatial resolution of 3 cm, and the data are taken with a temporal resolution of 200 ms. The resolving power ($\equiv \lambda / \Delta\lambda$) at λ = 17 Å is 400 during the line identification and 80 during the profile measurement. Figure 4.2(a) shows the vertical profiles of line intensity integrated along the observation chords against different FeXVII transitions: 3C, 3D, 3F and 3G+M2.

The radial emissivity profiles shown in Fig. 4.2(b) are derived from the vertical profiles in Fig. 4.2(a) based on an Abel inversion technique. The magnetic flux surface structure in LHD plasmas is calculated with a variation moments equilibrium code (VMEC) [13, 14]. Then, the integral lengths of the emissivity at all magnetic surfaces are evaluated with a finite-β value along the observation chords of the spectrometer. Here, we should point out that the magnetic flux surfaces are also

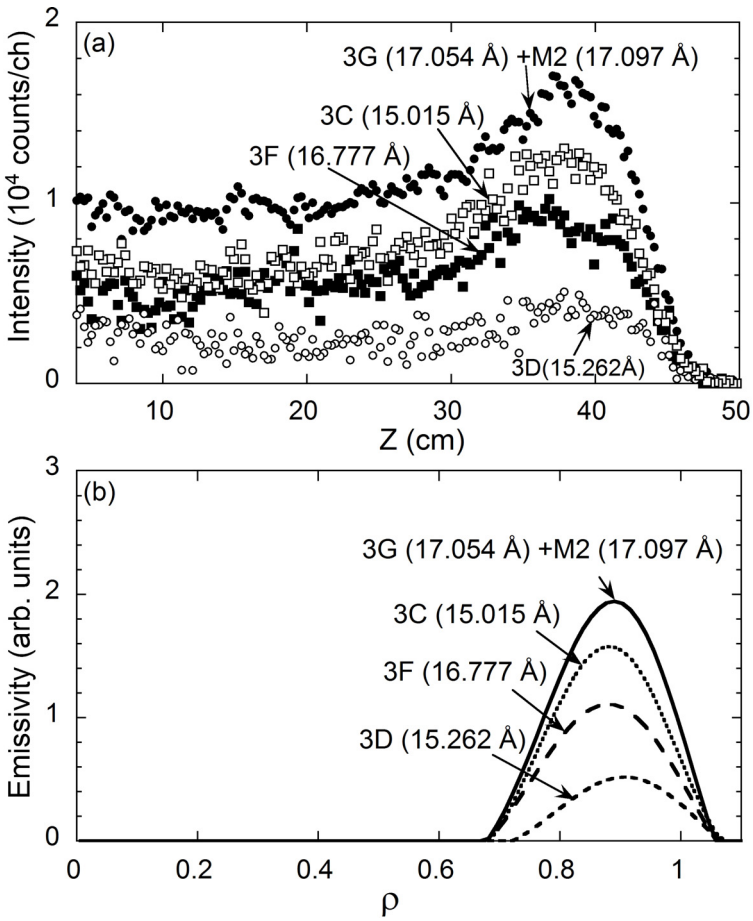

Fig. 4.2 (a) Vertical profiles of the chord-integrated intensity and (b) emissivity profiles as a function of normalized radius in Ne-like FeXVII n = 3–2 transitions.

assumed to exist outside the last closed flux surface (LCFS) by extrapolating the contour of the magnetic surface. Although the assumption may cause a certain uncertainty, it does not strongly affect the emissivity peak inside the LCFS because the emissivity outside the LCFS is usually weak.

4.3 Collisional-radiative model for iron

A CR model, including the fine-structure levels with the principal quantum number up to n = 5, is developed for Fe ions [15, 16]. If a quasi-steady state is assumed, the CR model includes all relevant atomic processes necessary for determining the level population. Most atomic data are calculated with the HULLAC code [17]. Although the population density of an excited level contains both the ionizing and the recombining plasma components, the ionizing plasma component is dominant because the plasma discharge is stable; the recombination process is only dominant in the plasma termination phase.

The intensity coefficients of the Fe XVII transitions are calculated using the CR model. The result is shown in Fig. 4.3. The populations in the upper levels of the 3d–2p transitions (3C, 3D and 3E) are mainly determined by the collisional excitation

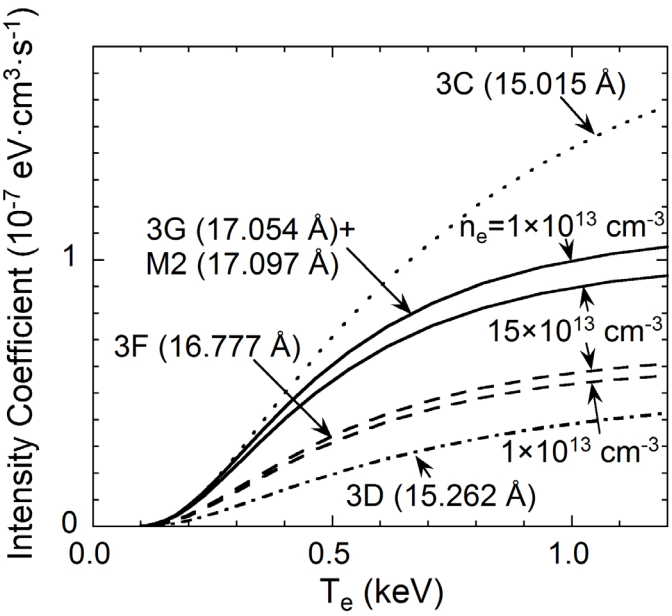

Fig. 4.3 Intensity coefficients of FeXVII n = 3–2 transitions as a function of electron temperature calculated with the CR model.

from the ground level whereas the upper levels of the 3s–2p transitions (3F, 3G and M2) are dominantly populated by cascades from higher levels [18]. Population redistribution through collision appears in the 3s–2p transitions when the electron density increases above 10^{13} cm^{-3} [5]. As a result, the intensities of the 3G and the 3F lines increase with increasing density, while the M2 intensity decreases with increasing density because the M2 line is a forbidden transition. The M2 intensity is then more sensitive to the density.

4.4 Analysis of the emissivity ratios among FeXVII *n* = 3–2 transitions

4.4.1 Temperature effect on emissivity ratios

The emissivities of the 3C, 3D and 3F transitions are analyzed by taking the ratio against the 3G+M2 transition. The ratio is evaluated at the peak position of the emissivity profiles in the electron density range of n_e = 1–5 × 10^{13} cm^{-3}. The emissivity ratios analyzed here are shown in Fig. 4.4 as a function of the electron temperature T_e. The result from a theoretical calculation with the CR model is also shown in Fig. 4.4. The temperature and the density profiles measured by using the Thomson scattering diagnostic is used in the analysis.

The CR model calculation predicts that the emissivity ratios of the 3D and the 3F to the 3G+M2 transitions, i.e., $\varepsilon_{3D}/\varepsilon_{(3G+M2)}$ and $\varepsilon_{3F}/\varepsilon_{(3G+M2)}$, are not sensitive to the electron temperature. The measurement plotted in Fig. 4.4 also indicates a weak dependence on T_e and shows good agreement with the theoretical prediction. On the other hand, the emissivity ratio $\varepsilon_{3C}/\varepsilon_{(3G+M2)}$ is also predicted to increase with increasing T_e. The ratio is then carefully investigated as shown in Fig. 4.3. The measured ratio is found to be smaller than the theoretical calculation by 25–40%. Because the ratios of $\varepsilon_{3D}/\varepsilon_{(3G+M2)}$ and $\varepsilon_{3F}/\varepsilon_{(3G+M2)}$ are in good agreement between the measurements and the calculations, the discrepancy in the ratio of $\varepsilon_{3C}/\varepsilon_{(3G+M2)}$ should be attributed to an overestimate of the 3C emissivity.

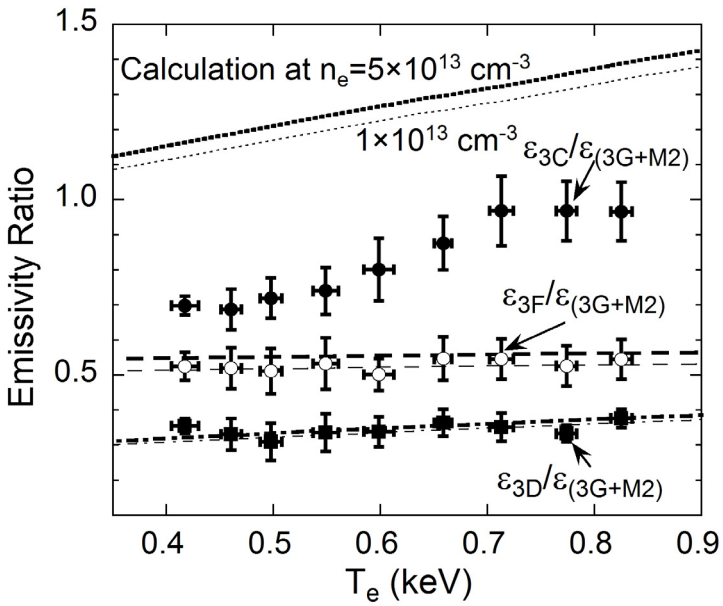

Fig. 4.4 Emissivity ratios of FeXVII transitions as a function of electron temperature (circles and squares: measurements, lines: CR model calculations).

The discrepancy related to the 3C emissivity has also been studied in laboratory and astrophysical plasmas based on an analysis of the ratio $R \equiv \varepsilon_{3C}/\varepsilon_{3D}$. The ratio R in the present study ranges from 2.0 to 2.9 as T_e increases from 0.4 keV to 0.8 keV. The value is obviously lower than the predicted range of R = 3.6–3.7. The present result is entirely consistent with the results from the solar corona [19], the Princeton Large Torus (PLT) tokamak [6] and electron beam ion traps (EBITs) [3, 20]. It also reveals that the discrepancy does not originate in certain effects related to chord-integrated information. Although there is no atomic theory explaining the discrepancy at present, the result from the EBIT at Lawrence Livermore National Laboratory (LLNL) suggests that the excitation cross section of the 3C transition in the theoretical calculation is obviously underestimated while the cross section of the 3D transition is in good agreement with theory [21]. The excitation cross section is proportional to the oscillator strength of the transition and to the Gaunt factor in the high-energy limit [22]. A recent study on the ratio of oscillator strength of 3C/3D suggests that the discrepancy is caused by the accuracy in the atomic wave functions [23]. If more accurate theoretical ratio, which should be close to the experimental value, is to be

obtained, further improvement, including more complete treatment of the spin-orbit interaction, is necessary for theoretical modeling.

4.4.2 Density effect on emissivity ratios

In addition to the T_e dependence of the ratio, the density effect on the ratio $\varepsilon_{3F}/\varepsilon_{(3G+M2)}$ has been examined. The density effect is studied by analyzing two discharges with distinctly different densities. The result is shown in Fig. 4.5. Shot numbers of #119551 and #118639 indicate a high-density discharge with flat T_e and centrally-peaked n_e profiles and a low-density discharge with centrally-peaked T_e and flat n_e profiles, respectively (see Figs. 4.5(b) and (c)). The emissivity ratio analyzed from the profiles is plotted in Fig. 4.5(a) along with the result from the CR model calculation. Due to data scattering in the vicinity of the plasma edge and to the uncertainty in the Abel inversion near the plasma center, the emissivity ratio profile is expressed in a limited range of normalized radius from $\rho = 0.2$ to $\rho = 0.8$.

The emissivity ratio at high density (#119551) is evidently larger than that at low density (#118639). Because the temperatures of two discharges are almost identical in the region of $0.6 < \rho < 0.8$, the difference in the emissivity ratios between the two discharges is certainly attributed to the density effect. These different values of the measured ratio also show excellent agreement with the CR model calculation. Furthermore, we notice that the ratio of #119551 increases with increasing density as a function of ρ because the temperature radially stays constant while the ratio of #118639 increases with increasing temperature as a function of ρ.

The space-resolved spectra from discharges similar to shot #119551 have been analyzed to study the density dependence of $\varepsilon_{3F}/\varepsilon_{(3G+M2)}$. Figure 4.6 shows the measured ratio as a function of electron density. The result from the CR model calculation is also plotted as the dashed line. In the analysis, the electron temperature is fixed at 0.5 keV where the Ne-like iron is usually located. The ratios obtained here increase with increasing electron density and agree well with the theoretical calculation in the density range of $n_e = 4–22 \times 10^{13}$ cm^{-3}; the relatively large error bars are due to the low signal-to-noise ratio in the measured signal. As a result, the effect of density on the FeXVII emissivity ratio is clearly confirmed in the present study.

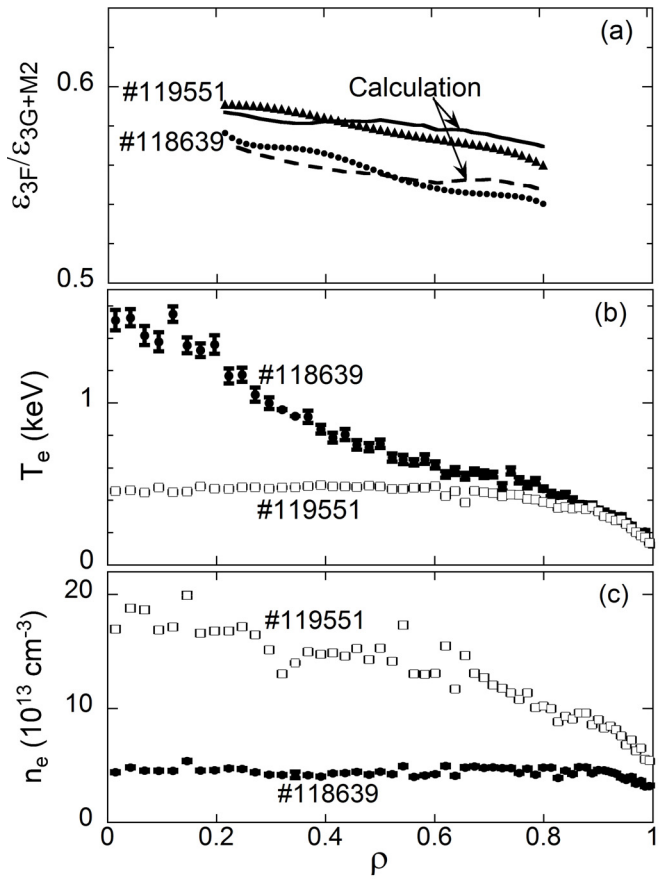

Fig. 4.5 (a) Emissivity-ratio profiles of $\varepsilon_{3F}/\varepsilon_{(3G+M2)}$ in two discharges at different densities (triangles and circles: measurement, lines: CR model calculations), (b) electron-temperature profiles, and (c) electron-density profiles.

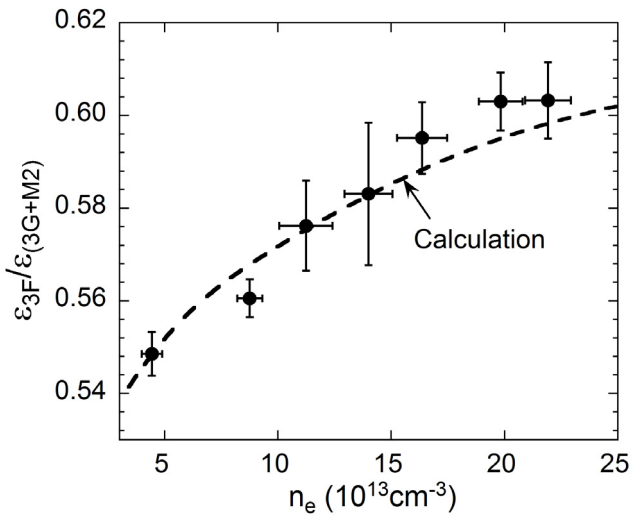

Fig. 4.6 Emissivity ratio, $\varepsilon_{3F}/\varepsilon_{(3G+M2)}$, as a function of electron density (closed circles: measurements, dashed line: CR model calculation).

4.5 Summary

Ne-like FeXVII n = 3–2 L_α transitions denoted with labels of 3C, 3D, 3E, 3F, 3G and M2 have been observed, along with the radial intensity profiles, from LHD plasmas. The radial emissivity profiles of the FeXVII transitions are calculated from the intensity profiles by means of Abel inversion, and the emissivity ratios among the FeXVII transitions are analyzed. A CR model specially developed for Fe ions is applied for analyzing the data. Although the emissivity ratios of $\varepsilon_{3D}/\varepsilon_{(3G+M2)}$ and $\varepsilon_{3F}/\varepsilon_{(3G+M2)}$ agree well with the CR model calculations, the emissivity ratio of $\varepsilon_{3C}/\varepsilon_{(3G+M2)}$ shows a clear discrepancy by 25%–40%. The result indicates that the discrepancy is not caused by the chord-integrated effect in the measured intensity. The effect of density on the emissivity ratio of $\varepsilon_{3F}/\varepsilon_{(3G+M2)}$ is also examined. The result experimentally verifies that the ratio is sensitive to the electron density as well as to the electron temperature.

References

[1] K. Waljeski, D. Moses, K. P. Dere, J. Saba, D. Web, and D. Zarro, Astrophys. J. **429**, 909 (1994).

[2] S. M. Kahn, F. D. Seward, and T. Chlebowski, Astrophys. J. **283**, 286 (1984).

[3] G. V. Brown, P. Beiersdorfer, D. A. Liedahl, K. Widmann, and S. M. Kahn, Astrophys. J. **502**, 1015 (1998).

[4] K. J. H. Phillips, C. J. Greer, A. K. Bhatia, I. H. Coffey, R. Barnsley, and F. P. Keenan, Astron. Astrophys. **324**, 381 (1997).

[5] M. Klapisch, A. Bar Shalom, J. L. Schwob, B. S. Fraenkel, C. Breton, C. de Michelis, M. Finkenthal, and M. Mattioli, Phys. Lett. A **69**, 34 (1978).

[6] P. Beiersdorfer, S. von Goeler, M. Bitter, and D. B. Thorn, Phys. Rev. A **64**, 032705 (2001).

[7] P. Beiersdorfer, M. Bitter, S. von Goeler, and K. W. Hill, Astrophys. J. **610**, 616 (2004).

[8] J. C. Raymond, and B. W. Smith, Astrophys. J. **306**, 762 (1986).

[9] P. Beiersdorfer, S. von Goeler, M. Bitter, K. W. Hill, R. A. Hulse, and R. S. Walling, Rev. Sci. Instrum. **60**, 895 (1989).

[10] U. Feldman, Comments At. Mol. Phys. **31**, 11 (1995).

[11] J. L. Saba, J. Y. Schmelz, A. K. Bhatia, and K. T. Strong, Astrophys. J. **510**, 1064 (1999).

[12] X. L. Huang, S. Morita, T. Oishi, M. Goto, and C. F. Dong, Rev. Sci. Instrum. **85,** 043511 (2014).

[13] K. Yamazaki, J. Plasma Fusion Res. **79**, 739 (2003).

[14] S. P. Hirshman, W. I. van Rij, and P. Merkel, Comput. Phys. Commun. **43**, 143 (1986).

[15] N. Yamamoto, T. Kato, H. Funaba, K. Sato, N. Tamura, S. Sudo, P. Beiersdorfer, and J. K. Lepson, Astrophys. J. **689**, 646 (2008).

[16] I. Murakami, H. A. Sakaue, N. Yamamoto, D. Kato, S. Morita, and T. Watanabe, Plasma and Fusion Research **5**, S2021 (2010).

[17] A. Bar-Shalom, M. Klapisch, and J. Oreg, J. Quant. Spectrosc. Radiat. Trans. **71**, 179 (2001).

[18] B.W. Smith, J. C. Raymond, J. B. Mann, and R. D. Cowan, Astrophys. J. **298**, 898 (1985).

[19] A. K. Bhatia and J. L. R. Saba, Astrophys. J. **563**, 434 (2001).

[20] J. M. Laming, I. Kink, E. Takacs, J. V. Porto, J. D. Gillaspy, E. H. Silver, H. W. Schnopper, S. R. Bandler, N. S. Brickhouse, S. S. Murray, M. Barbera, A. K. Bhatia, G. A. Doschek, N. Madden, D. Landis, J. Beeman, and E. E. Haller, Astrophys. J. **545**, L161 (2000).

[21] G. V. Brown, Can. J. Phys. **86**,199 (2008).

[22] H. Van Regemorter, Astrophysical J. **136**, 906 (1962).

[23] S. Bernitt, G.V. Brown, J. K. Rudolph, R. Steinbrugge, A. Graf, M. Leutenegger, S. W. Epp, S. Eberle, K. Kubicek, V. Mackel, M. C. Simon, E. Trabert, E. W. Magee, C. Beilmann, N. Hell, S. Schippers, A. Muller, S. M. Kahn, A. Surzhykov, Z. Harman, C. H. Keitel, J. Clementson, F. S. Porter, W. Schlotter, J. J. Turner, J. Ullrich, P. Beiersdorfer, and J. R. C. Lopez-Urrutia, Nature **492**, 225 (2012).

Chapter 5

Z_{eff} profile analysis in high T_{i} discharges using EUV bremsstrahlung

5.1 Introduction

Impurity behavior has been extensively studied in both theoretical and experimental fields in fusion research because impurities play an important role on the plasma performance [1, 2]. Impurity accumulation leads to a large radiation loss and ion dilution, especially in H-mode plasmas with a long impurity confinement time [3]. Recent experiments suggest an importance of the electron heating to avoid the impurity accumulation [4, 5]. Gyro-kinetic and fluid simulations have been also used for understanding the impurity transport [6]. In the Large Helical Device (LHD), an

improvement of plasma performance with increase in central T_i has been observed with carbon pellet injection [7]. It is therefore necessary to investigate the impurity behavior in such discharges.

The impurity content is commonly characterized by the effective ion charge $Z_{eff} = \sum_i n_i Z_i^2 / \sum_i n_i Z_i = \sum_i n_i Z_i^2 / n_e$. Z_{eff} can be derived from the emissivity of bremsstrahlung, which is expressed by the following equation [8]:

$$\varepsilon_{brem} = \frac{1.89\times10^{-28} n_e^2 g_{ff} Z_{eff}}{T_e^{1/2}\lambda^2}\exp\left(\frac{-12400}{T_e\lambda}\right), \qquad (1)$$

where ε_{brem} (W·cm^{-3}·Å), n_e (cm^{-3}), g_{ff}, T_e (eV) and λ (Å) stand for the emissivity, the electron density, the free-free gaunt factor, the electron temperature and the wavelength, respectively.

A Czerny-Turner spectrometer has been installed on the LHD to measure the radial bremsstrahlung profile in the visible range [9]. However, the visible bremsstrahlung profile is strongly affected and distorted by bremsstrahlung emission from the edge boundary of the LHD ergodic layer in low-density discharges [10]. As the electron density in high T_i discharges is usually below 2×10^{13} cm^{-3}, it becomes difficult to obtain Z_{eff} profiles using the visible spectrometer. On the contrary, the bremsstrahlung in the extreme ultraviolet (EUV) range is free of the non-uniform edge bremsstrahlung emission because of the higher photon energy in the EUV range compared with that in the visible range. In addition, the bremsstrahlung is much stronger in the EUV range. Therefore, Z_{eff} profiles in high-T_i discharges can be evaluated from the space-resolved measurement of EUV bremsstrahlung.

5.2 Experimental setup and intensity calibration

Two space-resolved EUV spectrometers have been installed on LHD [11,12]. Both spectrometers include an entrance slit, a spatial-resolution slit, a varied-line-spacing holographic grating and a charge-coupled device (CCD) detector with 1024 × 255 pixels. Time resolution of the two systems was 200 ms in 2012 and has been improved to 50 ms after the installation of a new CCD for each system in 2013. The vertical spatial resolution of the systems is roughly 3 cm. A space-resolved spectrometer called 'EUV-Short2' works in the wavelength range of 10–130 Å and can

measure upper half of the elliptical plasma, as shown in Fig. 5.1. The other spectrometer, called 'EUV-Long2', works in the wavelength range of 30–650 Å, which can measure either upper or lower half profile. A 0.5 μm-thick filter made of polyethylene terephthalate (PET) is installed in each system to reduce spike noises caused by high-energy NBI particles. The filter can effectively eliminate the spike noise. A spectrum measured by EUV-Long2 in a low density discharge is shown in Fig. 5.2. The continuum can be observed at the base line of the spectrum.

In order to obtain a better signal-to-noise ratio, the aperture size of the slits in the EUV systems are changed to 200 μm (width of entrance slit) × 2 mm (height of space-resolved slit), which is four and two times as large as the sizes of the usually used slits for EUV-Short2 and EUV-Long2, respectively. Consequently, new intensity calibration is necessary to obtain the absolute intensity. The EUV systems are calibrated by means of comparison between visible and EUV bremsstrahlung profiles.

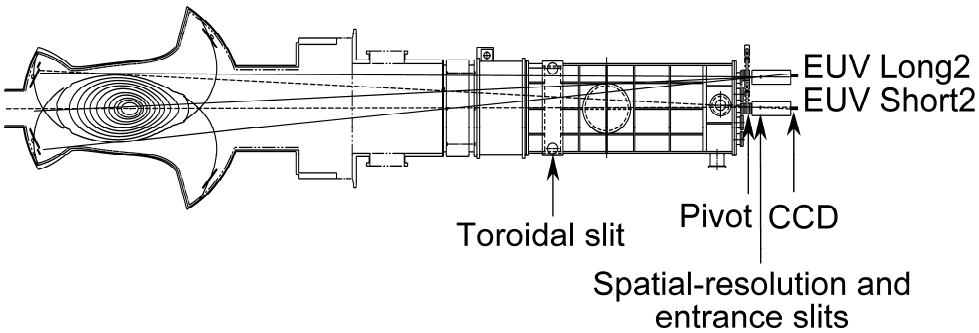

Fig. 5.1 Observation ranges of the EUV-Short2 (dashed lines) and the EUV-Long2 (solid lines) systems in the vertical direction at a horizontally elongated plasma cross section on the LHD.

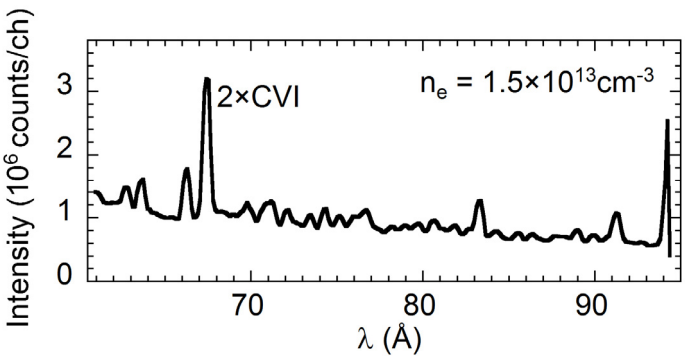

Fig. 5.2 EUV spectrum measured by EUV-Long2 in a low-density discharge.

The visible bremsstrahlung profile has been measured by the above-mentioned Czerny-Turner spectrometer. Figure 5.3 shows the calibration results. Fitting with previous calibration curves are also plotted with solid lines. The calibration factor shows that the system brightness is enhanced by a factor of 4.0 and 2.2 for EUV-Short2 and EUV-Long2, respectively. This means the system brightness is approximately proportional to the size of the slit aperture.

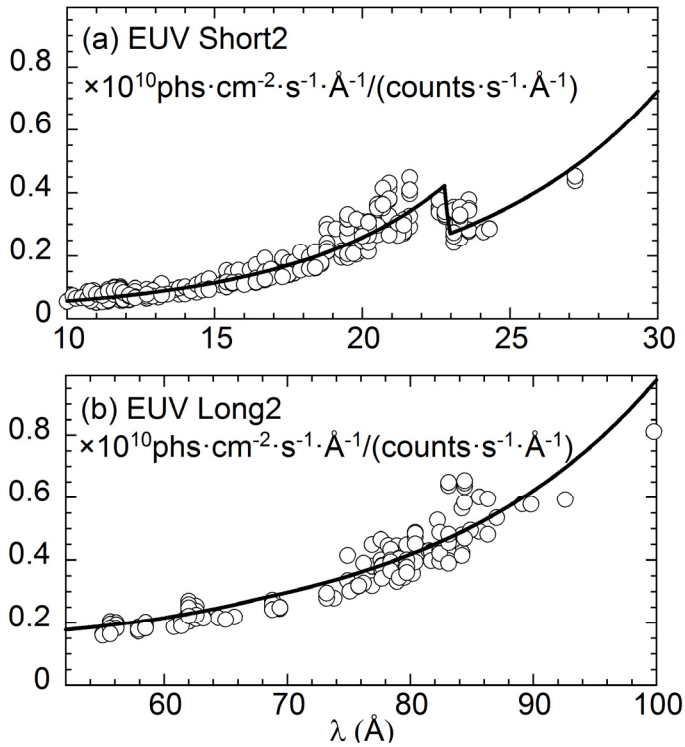

Fig. 5.3 Intensity calibration factors as a function of wavelength for (a) EUV Short2 and (b) EUV Long2. Solid lines denote fitting curves using previous calibration results.

5.3 Analysis of Z_{eff} Profile

A typical example of Z_{eff} profile analysis at λ = 77.4–80.0 Å is shown in Fig. 5.4. The vertical profile of the line-integrated signal is plotted in Fig. 5.4(a) and radial profiles of n_{e}, T_{e}, ε and Z_{eff} are shown in Figs. 5.4(b)–(e), respectively.

The emissivity profile, ε, is derived from the line-integrated profile based on Abel inversion. The magnetic surface used in the inversion is calculated with VMEC code

[13]. The emissivity near the last closed flux surface (LCFS) is much larger than that in the plasma core (ρ < 0.75) as seen in Fig. 5.4(d). It seems that the large amount of continuum radiation is attributed to recombination radiation instead of bremsstrahlung because the intensity of bremsstrahlung is limited by Z_{eff}, which should be less than 6 if the impurity density is determined by only carbon. Since the photon energy is around 158 eV, the recombination radiation mainly originates in C^{4+} and C^{5+}. This is verified by comparison of the edge continuum emissivity profile with C^{5+} and C^{4+} density profiles measured using CVI 33.73 Å and CV 40.27 Å & 40.73 Å, as shown in Fig. 5.4(d). The edge emissivity profile seems to be a superposition of the shapes of the two line emission profiles.

Despite the large amount of recombination radiation in the edge, the emissivity profile is basically free of recombination radiation in the plasma core (ρ < 0.75) because of the following reasons.

First, the enhancement of continuum emissivity due to recombination radiation dramatically decreases with increasing electron temperature [14]. For instance, the enhancement factor of recombination radiation caused by C^{5+} is around 12 at T_e = 0.2 keV while the factor decreases to 1.2 at T_e = 2 keV. Second, the impurity ions contributing to the observed recombination radiation, namely, C^{4+} and C^{5+}, are mainly located in the edge. Therefore, the emission from the plasma core certainly consists of only the bremsstrahlung.

In order to complete the Abel inversion, the magnetic surface obtained with the VMEC code is linearly extrapolated to the region of $1 < \rho \leq 1.3$. If the bremsstrahlung continuum or impurity emissivity outside the LCFS is nonuniform in the poloidal direction, the measured line-integrated profile will be distorted. However, it is not the case in the EUV bremsstrahlung measurement because the energy is relatively high. The C^{4+} and C^{5+} ions distribute around the LCFS where the connection length L_c is still quite long, e.g., $L_c > 10^3$ m. Therefore, the ion density can be considered to be uniform in the poloidal direction and then the resultant recombination radiation with such ions will be also uniform. This is verified by an impurity simulation in the ergodic layer [15].

A possible uncertainty caused by the recombination radiation from X points of the ergodic layer should be also taken into account. Assuming that emissions from the X point region enhance the integrated emissivity outside the LCFS along a viewing chord

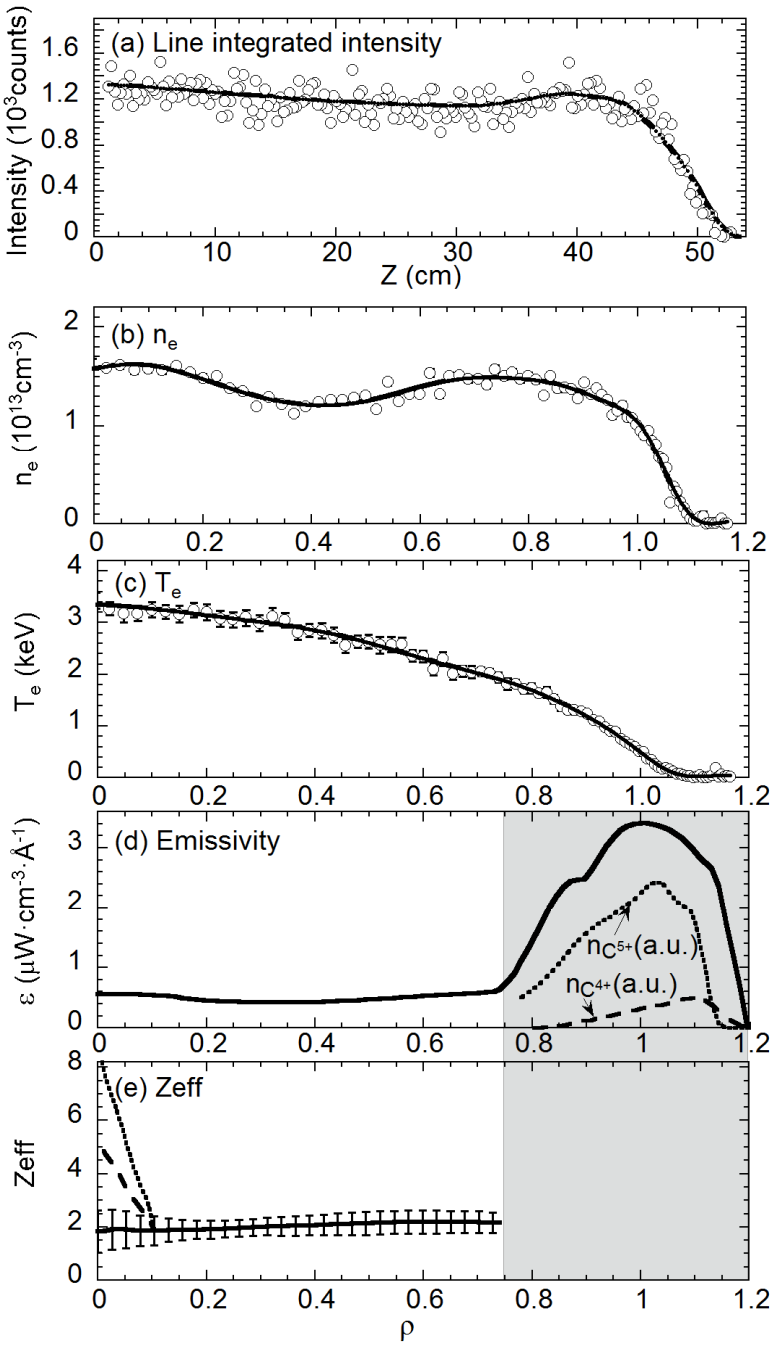

Fig. 5.4 (a) Line-integrated signal and radial profiles of (b) n_e, (c) T_e, (d) continuum emissivity at 77.4 Å - 80.0 Å and (e) Z_{eff}. Solid lines in (a)-(c) indicate curve fitting and shaded area in (d) and (e) denotes the region affected by recombination radiation. Dashed and dotted lines in (d) denote shapes of C^{5+} and C^{4+} density profiles. Dashed and dotted lines in (e) indicate Z_{eff} deviation assuming strong emissions from the X point region.

of the spectrometer by a percentage of 5% or 10%, the Z_{eff} near plasma center increases abruptly, as shown in Fig. 5.4(e). This effect is sometime observed in the measurement. Fortunately, the X point region with relatively strong emissions is usually narrow in the vertical direction, usually within $Z = \pm 5$ cm. Therefore, only the viewing chord passing through this narrow vertical region is affected by unnecessary emissions. It corresponds to the radial region of $\rho < 0.1$. In other words, the Z_{eff} profile can be always measured successfully in most radial ranges in the plasma core.

The error bars plotted in Fig. 5.4(e) is calculated from the data scattering involved in the line-integrated intensity, the electron density and the electron temperature. The total uncertainty is estimated to be 20%–30%.

5.4 Evolution of Z_{eff} Profile in High-T_i Discharges

Time evolution of the NBI port-through power P_{NBI}, n_e, T_e, T_i, the plasma stored energy W_p and the radiation power P_{rad} are shown in Fig. 5.5. The Z_{eff} profile analysis is performed in six time frames, designated as F1–F6 as denoted in Fig. 5.5. A carbon pellet is injected at $t = 4.5$ s. The line-integrated density n_e increases from 1.0×10^{13} cm^{-3} to 2.2×10^{13} cm^{-3} after the pellet injection and then gradually decays to 1.4×10^{13} cm^{-3}. The electron temperature T_e is not significantly affected by the pellet. The ion temperature T_i increases from 3.1 keV to 4.2 keV and becomes higher than T_e after the injection (F2). The value of T_i is maintained at around 4.0 keV for 200 ms (F3). The decrease in T_i starts from $t = 5.0$ s and becomes lower than T_e after $t = 5.25$ s.

The radial profiles of Z_{eff}, n_{C5+}/n_e, T_i and T_e in the above-mentioned time frames F1-F6 are shown in Fig. 5.6. The Z_{eff} profile in Fig. 5.6(a) is basically flat before the pellet injection. In the frame just after the injection (F2), the line-averaged Z_{eff} value increases by approximately 0.8 and a centrally peaked Z_{eff} profile occurs. At the same time, the T_i profile is increased as a whole and becomes higher than T_e in the central region ($\rho < 0.6$). All three profiles are maintained in the next time frame when the central T_i stays at 4.0 keV (F3). The normalized C^{5+} density (n_{C5+}/n_e) profile derived from CVI 28.5 Å is shown in Fig. 5.6(b). The radial profile of C^{5+} density in the plasma core shows a good agreement with the Z_{eff} profiles in F2 and F3. The C^{6+} ion density is estimated to be roughly three to four times as high as the C^{5+} density just after the pellet injection by referring a result from similar discharges with

carbon pellet injection. The central Z_{eff} is thus around 3.5. With the presence of other impurities taken into account, the Z_{eff} value should be slightly higher. Therefore, the present Z_{eff} value of 3.6 is quite reasonable in F2. When the T_i starts to decrease at t = 5.0 s, the Z_{eff} profile gradually returns to the original shape before the injection. Here, it is noted that the C^{5+} density profile measurement in the plasma core is not easy except for the period just after the pellet injection due to the low signal-to-noise ratio. The T_i profile tends to exhibit a similar behavior to the Z_{eff} profile. Then, the Z_{eff} values at ρ = 0.1 are compared with T_i values at ρ = 0.1 for the six time frames of F1–F6. The result is plotted in Fig 5.7. The value of Z_{eff} clearly increases with increasing T_i. The T_e profile and its central value remain basically unchanged in all time frames. Comparison between the Z_{eff} and T_i profiles strongly indicates that there is a positive relation between Z_{eff} and T_i. Possible explanations

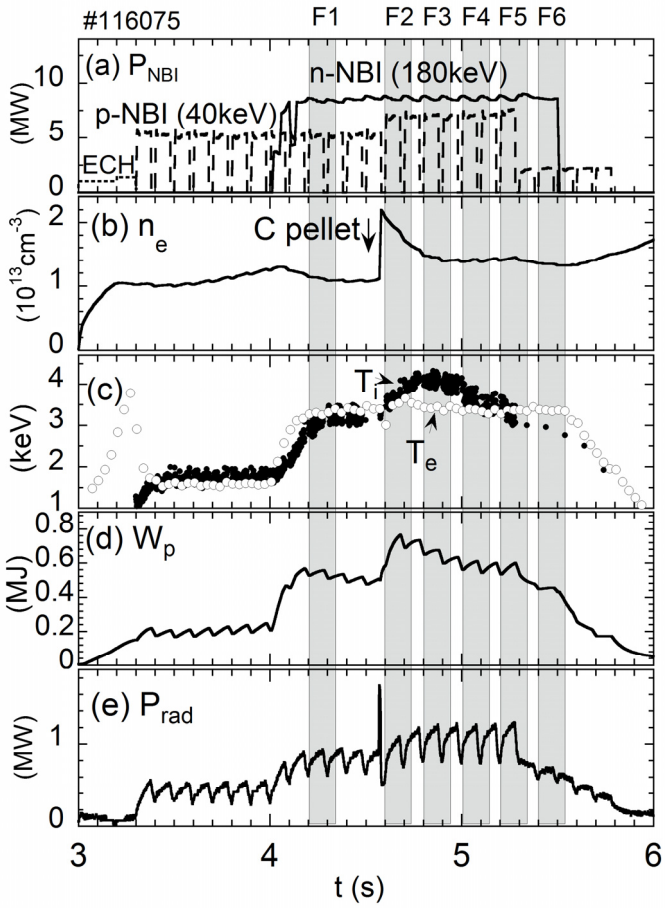

Fig. 5.5 Time evolution of (a) NBI port-through power, (b) n_e, (c) T_e and T_i, (d) plasma stored energy W_p and (e) radiation power P_{rad}. Dashed areas indicate six time frames of F1–F6.

are an enhancement of the absorption efficiency of NBI power and ion heating power per ion with increasing Z_{eff}. It has been also identified that the plasma confinement is improved in such high T_i discharges with carbon pellet injection. A recent study shows there is a strong relation between the density of the carbon impurity and the thermal diffusivity [16]. The time behavior of the Z_{eff} and T_i profiles also suggests that Z_{eff} plays an important role in the confinement improvement.

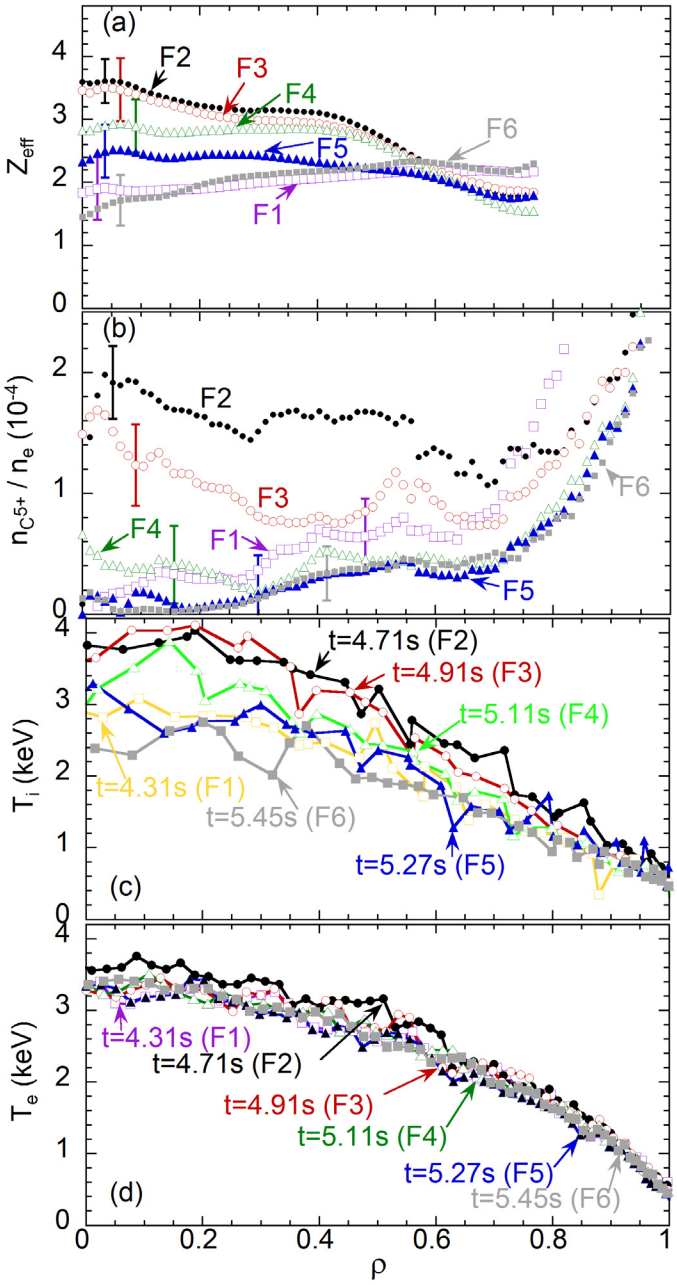

Fig. 5.6 Profiles of (a) Z_{eff}, (b) n_{C5+}/n_e, (c) T_i and (d) T_e in in the six time frames of F1–F6.

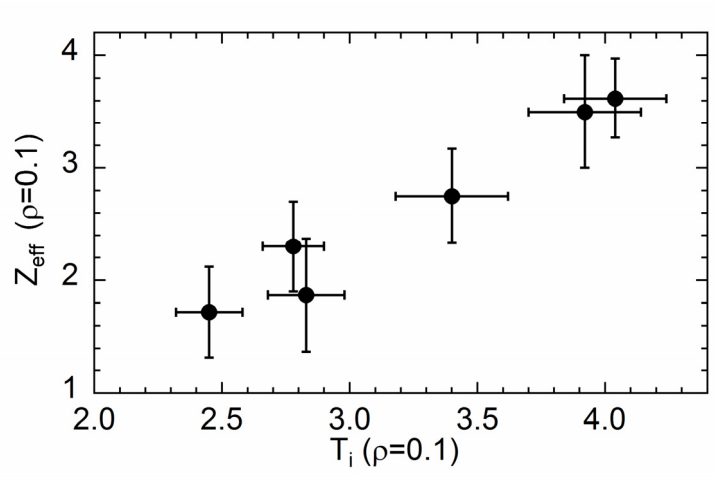

Fig. 5.7 Z_{eff} as a function of T_i at ρ = 0.1 measured in the six time frames of F1–F6.

5.5 Density dependence of Z_{eff}

In order to examine the density dependence of Z_{eff}, the Z_{eff} value is analyzed at ρ = 0.5 in NBI discharges with a flat n_e profile. The standard magnetic configuration with the largest plasma volume in LHD is chosen for the present analysis, i.e. the magnetic axis position of R_{ax} = 3.6 m and the toroidal magnetic field of B_t = 2.75–2.85 T. The result is plotted in Fig. 5.8. The value of Z_{eff} clearly decreases with increasing n_e. In density range of $n_e > 4 \times 10^{13}$ cm^{-3}, the present result analyzed from the EUV bremsstrahlung is consistent with previously studied Z_{eff} values using visible bremsstrahlung [17], while the Z_{eff} measurement with visible bremsstrahlung is not accurate at $n_e \leq 4 \times 10^{13}$ cm^{-3}.

The Z_{eff} value is also examined in ECH and ICRF&ECH discharges (R_{ax} = 3.6 m and B_t = 2.75 T), as plotted in Fig. 5.9. The value of Z_{eff} decreases with increasing n_e in the ICRF&ECH case, which has a similar trend to Z_{eff} in the NBI discharge. In the ECH discharge, however, any obvious relation is not seen between Z_{eff} and n_e. In addition, the Z_{eff} has larger values in ICRF&ECH discharges compared with those in ECH discharges below 1.7×10^{13} cm^{-3}, while the value is similar each other above 2.3×10^{13} cm^{-3}. An enhancement of impurity influx is observed in ICRF&ECH discharges. It is probably caused by the presence of ICRF antennas and perpendicularly accelerated high-energy ions. Another possible reason seems to be due to the difference in the

impurity transport between the two discharges, e.g. temperature screening based on steep temperature gradient in ECH discharges. Further detailed analysis is necessary to clarify the observed difference between ICRF and ECH discharges.

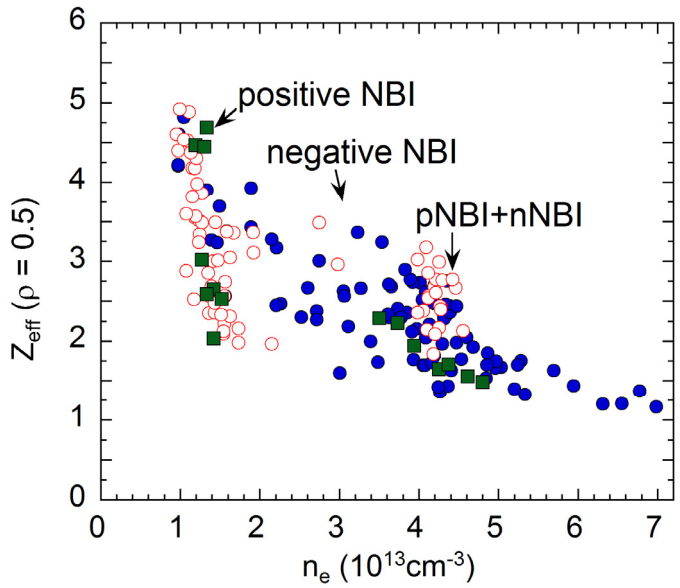

Fig. 5.8 Z_{eff} as a function of n_e in NBI-heated plasmas (n-NBIs: solid circles, p-NBIs: solid squares and p-NBI + n-NBI: open circles).

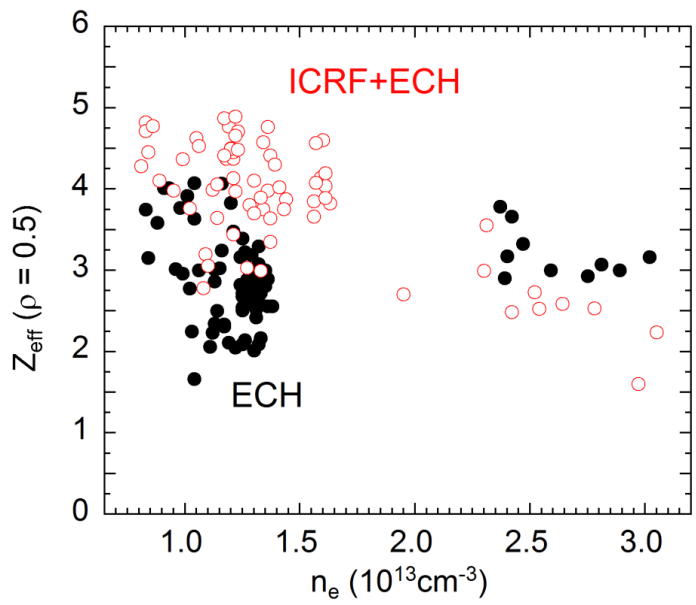

Fig. 5.9 Z_{eff} as a function of n_e in ICRF&ECH- and ECH- heated plasmas (ECH: solid circles and ICRF + ECH: open circles).

5.6 Summary

The Z_{eff} profile has been successfully obtained in the plasma core ($\rho < 0.75$) from space-resolved profiles of bremsstrahlung in the EUV range. The recombination radiation can give a significant effect on the bremsstrahlung profile, in particular, in the edge region ($\rho > 0.75$) and also a small region ($\rho < 0.1$) near the plasma center. The time behavior of Z_{eff} profiles suggests a strong relation between Z_{eff} and T_i. The density dependence of Z_{eff} values is also examined at half plasma radius. The analyzed Z_{eff} value is found to decrease with ne in NBI and ICRF&ECH discharges, while no density dependence is observed in ECH discharges.

References

[1] T. Fülöp *et al.*, Phys. Plasmas **16**, 032306 (2009).

[2] G. P. Maddison *et al.*, Nucl. Fusion **43**, 49 (2003).

[3] C. Angioni *et al.*, Nucl. Fusion **54**, 083028 (2014)

[4] M. Valisa *et al.*, Nucl. Fusion **51**, 033002 (2011)

[5] M. Sertoli *et al.*, Plasma Phys. Control. Fusion **53**, 035024 (2011)

[6] N. T. Howard *et al.*, Plasma Phys. Control. Fusion **56** 124004 (2014)

[7] S. Morita *et al.*, Plasma Sci. Technol. **13**, 290 (2011).

[8] H. Y. Zhou *et al.*, J. Appl. Phys. **107**, 053306 (2010).

[9] H. Y. Zhou *et al.*, Rev. Sci. Instrum. **79**, 10F536 (2008).

[10] H. Y. Zhou *et al.*, Rev. Sci. Instrum. **81**, 10D706 (2010).

[11] C. F. Dong *et al.*, Rev. Sci. Instrum. **81**, 033107 (2010).

[12] X. L. Huang *et al.*, Rev. Sci. Instrum. **85**, 043511 (2014).

[13] K. Yamazaki *et al.*, J. Plasma Fusion Res. **79**, 739 (2003).

[14] E. H. Silver *et al.*, Rev. Sci. Instrum. **53**, 1198 (1982).

[15] E. H. Wang, *Development of two-dimensional EUV spectroscopy for study of impurity behavior in ergodic layer of LHD* (Doctoral thesis), The Graduate University for Advanced Studies, p.111-p.115 (2013).

[16] M. Osakabe *et al.*, Plasma Phys. Control. Fusion **56,** 095011 (2014).

[17] H.Y. Zhou *et al.*, Jpn. J. Appl. Phys. **49**, 106103 (2010).

Chapter 6

Iron transport analysis using radial profiles of Fe n = 3–2 L_α transition array

6.1 Introduction

Radial transport of impurity ions still remains several important issues in magnetically confined fusion devices, since the plasma performance is significantly affected by the radiation loss and fuel dilution caused by the impurity.

In the Large Helical Device (LHD), the density profile can exhibit a variety of distributions of a peaked, flat or hollow shape, depending on plasma parameters such as B_t, T_e and n_e. Therefore, it is of great importance to investigate the corresponding

impurity transport in the plasma core of LHD [1–3]. As a typical phenomenon in the impurity transport it is reported that the impurity accumulation can be also observed in LHD as well as tokamaks. However, the impurity transport has been usually analyzed based on an assumption of the radial structure of convection velocity and diffusion coefficient. In LHD it is also analyzed in high-density discharges with a centrally peaked density profile under assumed radial profiles of transport coefficients. [4]. On the other hand, formation of the hollow and flat density profiles frequently appeared in LHD is quite unique compared to the tokamak case. Therefore, the LHD plasma can give a good opportunity for studying the impurity transport in a variety of density profiles through analysis of the radial structure in the transport coefficient, in particular, in relation to the density and temperature gradients. For the purpose it is strongly requested to find a new technique with which the radial structure of the transport coefficients can be analyzed without initial assumption on the profile. If the detail structure analysis of transport coefficients is possible with the new technique, the result certainly brings us better understanding on the impurity radial transport.

In this chapter we represent the new method for the impurity transport analysis based on the radial profile measurement of Fe n = 3–2 L_α transition array. The iron transport can be then analyzed along the minor radius without any assumption on the radial structure of transport coefficients because the Fe L_α transitions of FeXVII to FeXXIV composing the L_α transition array existing at 10–18Å are emitted over a wide range of the radial plasma location.

6.2 Experimental setup and Fe L_α transition array

The EUV system used in the present study, which works in the wavelength range of 10–130Å, mainly consists of an entrance slit, a spatial-resolution slit, a gold-coated concave varied-line-spacing (VLS) laminar-type holographic grating with a groove density of 2400 per mm and a charge-coupled device (CCD) detector with 1024 × 255 pixels (26 μm × 26 μm / pixel). The EUV spectrometer is installed on a mid-plane port at the backside of a rectangular vacuum extension chamber.

The elevation angle of the central viewing chord is exactly aligned to make possible the vertical profile measurement at upper half of the elliptical plasma, i.e. Z =

0–50 cm, as shown in Fig. 6.1. A relatively long distance between the spectrometer and the plasma is necessary for observing the half vertical plasma range of 0.5 m. In practice the distance between the central plasma position and the entrance slit of the spectrometer is set to 9.157 m when the plasma axis position is R_{ax} = 3.90 m. Since the distance between the entrance slit and the CCD detector is roughly 0.47 m, which is a weak function of wavelength, we obtain a multiplication factor of 19.5. Figure 2.2 shows a top view of the optical layout in the spectrometer. EUV radiation emitted from LHD plasmas passes through the entrance slit and reaches the grating adjusted at the angle of incidence of 88.6°. The iron radiation diffracted on the grating is focused on the focal plane and recorded by the CCD detector. The large angle of incidence is necessary for observing the EUV light in such a short wavelength range with high throughput. Spectral and spatial resolutions, absolute intensity calibration and other details of the EUV spectrometer are described in chapter 2.

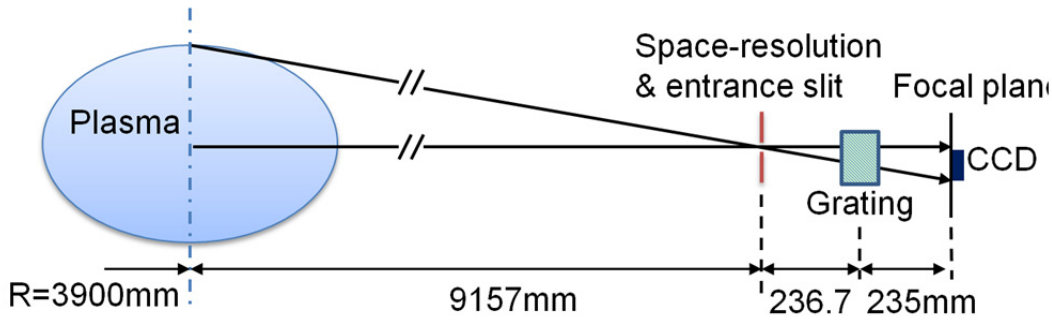

Fig. 6.1 Schematic view of the space-resolved EUV spectrometer system. The observation range in the vertical direction is indicated with two solid lines, i.e. the upper half at horizontally elongated plasma cross section on the LHD.

The iron spectrum including n = 3–2 L_α lines between 10 and 18 Å has been measured by injecting an iron impurity pellet [6]. The spectrum is replotted in Fig. 6.2 which is obtained from a different discharge from Fig. 2.17. A lot of L_α transitions from highly ionized iron are observed in the spectrum. Since many iron lines are blended, the spectrum seems to be a pseudo-continuum. The line-integrated vertical profile of the Fe L_α transition from FeXVII to FeXXIV is analyzed by carefully choosing the wavelength interval at each ionization stage. The result is shown in Figs. 6.3(a). The electron density and temperature profiles are also shown

in Figs. 6.3(b) of which the coordinate is converted into the vertical position at horizontally elongated plasma cross section by taking into account the elliptical magnetic surface. The vertical profile is normalized at each peak position. The peak position of each profile moves inside with increase in the ionization stage, reflecting the centrally peaked electron temperature profile. These new plots are determinately identical to the results already shown in Figs. 2.8(a) and (b), indicating a good reliability in the raw data and data analysis.

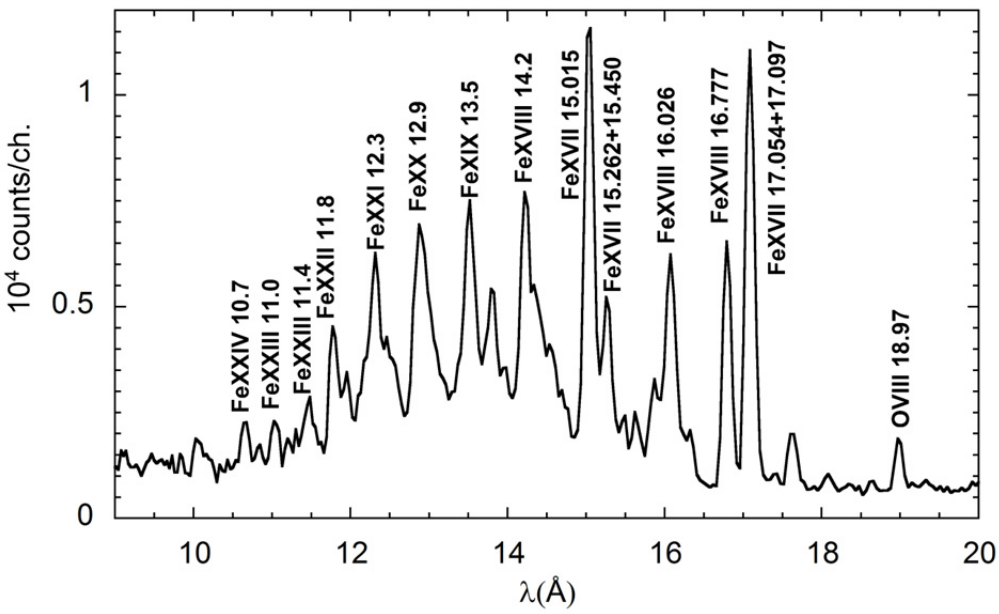

Fig. 6.2 Fe n = 3–2 L_α spectrum below 20 Å measured after iron impurity pellet injection in the NBI discharge #118739.

The emissivity profile is derived from the measured vertical profile based on a Fourier Method of Abel inversion [7]. The magnetic surface structure in LHD plasmas is calculated with variation moment equilibrium code (VMEC) [8]. Here, it should be pointed out that the magnetic flux surface calculated with the VMEC is also assumed outside the last close flux surface (LCFS) by extrapolating the magnetic surface contour at LCFS. Although the assumption may cause certain uncertainty, it does not strongly affect the emissivity peak inside the LCFS because the emissivity outside the LCFS is usually weak. The impurity density profile is then calculated from the emissivity profile based on intensity coefficients obtained with the HULLAC code [9].

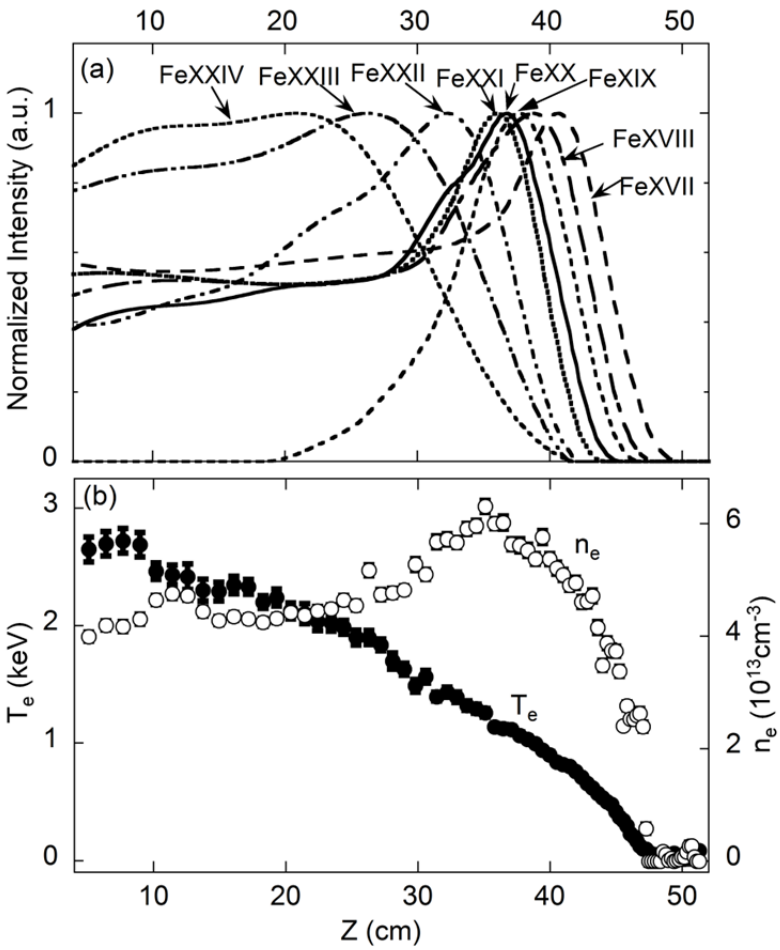

Fig. 6.3 (a) Line-integrated vertical intensity profiles of FeXVII (17.054 Å & 17.097 Å), FeXVIII (14.121–14.256 Å), FeXIX (13.424–13.520 Å), FeXX (12.763–12.978 Å), FeXXI (12.165–12.465 Å), FeXXII (11.748–11.797 Å), FeXXIII (10.935–11.047 Å), and FeXXIV (10.619 Å & 10.663 Å) and (b) electron temperature (closed circles) and density (open circles) profiles.

6.3 Description of one-dimensional impurity transport code

A one-dimensional impurity transport code is employed to determine the transport coefficient [10, 11]. It is assumed that the impurity ions satisfy the following equations on transport and continuity;

$$\Gamma_I^K = -D\frac{\partial n_I^K}{\partial r} + V n_I^K \tag{6.1}$$

and

$$\frac{\partial n_I^K}{\partial t} = -\frac{1}{r}\frac{\partial}{\partial r} r\Gamma_I^K + n_\mathrm{e}\left[S_I^{K-1} n_I^{K-1} - \left(S_I^K + \alpha_I^K\right) n_I^K + \alpha_I^{K+1} n_I^{K+1}\right], \tag{6.2}$$

where $\Gamma_I^K, n_I^K, D, V, S_I^K$ and α_I^K are the particle flux, the ion density, the diffusion coefficient, the convection velocity, the ionization rate coefficient and the recombination coefficient of impurity ions in the *K*th charge state, respectively. Positive and negative values of V stand for outward and inward convections, respectively.

Updated rate coefficients for ionization and recombination have been included in the present transport code [12–14], while ADPAK code was used in the old version. With given transport coefficients and radial profiles of plasma parameters, the code yields the impurity ion density profile in all charge states as a function of time.

The transport coefficient near the emissivity peak can be determined by comparing the emissivity profile between the measurement and the simulation. In order to determine the transport coefficient at the whole plasma radii, the iron emission is simultaneously analyzed at several charge states. The minimization of deviation between measured and simulated impurity profiles can uniquely give the solution as the transport coefficient profile.

6.4 Fe transport analysis of discharges with peaked density profile

Impurity accumulation has been observed with a centrally peaked density profile after hydrogen multi-pellet injection in the LHD. Here, the radial structure of the transport coefficient is analyzed using emissions of FeXVII at 15.02 Å and FeXVIII at 14.20 Å.

The waveform of a high-density discharge with multi-pellet injection is shown in Fig. 6.4 for the line-averaged electron density (n_e), central electron temperature ($T_\mathrm{e}(0)$), total radiation power (P_rad) and plasma stored energy (W_p) together with NBI port-through power (P_NBI). The emission profile is measured at the time frame

denoted with hatched area (t = 4.6–4.8 s) in Fig. 6.4, at which the plasma stays in a quasi-steady state.

The experimental and simulated emissivity profiles are plotted in Figs. 6.5(a) and (b), respectively. The coefficients determined from the comparison of two emissivity profiles are shown in Fig. 6.5(c). Figure 6.5(d) displays corresponding electron temperature and density profiles measured by Thomson scattering system. The simulated emissivity profile is basically in a good agreement with experimental one. The diffusion coefficient, D, is constant along the minor radius, while the convection velocity, V, increases with minor radius at $\rho < 0.75$ as an inward convection and then keeps a constant value of V = -2.5 m/s in the plasma periphery ($0.75 \leq \rho \leq 1$). When comparing Fig. 6.5(c) with Fig. 6.5(d), the structure of V seems to change with the density profile because the temperature profile is flat in the core region. Therefore, the radial profile of V obtained here roughly agrees with a conventionally assumed profile, i.e. $V = -V_0 \times \rho$, where V_0 is the convection velocity at LCFS.

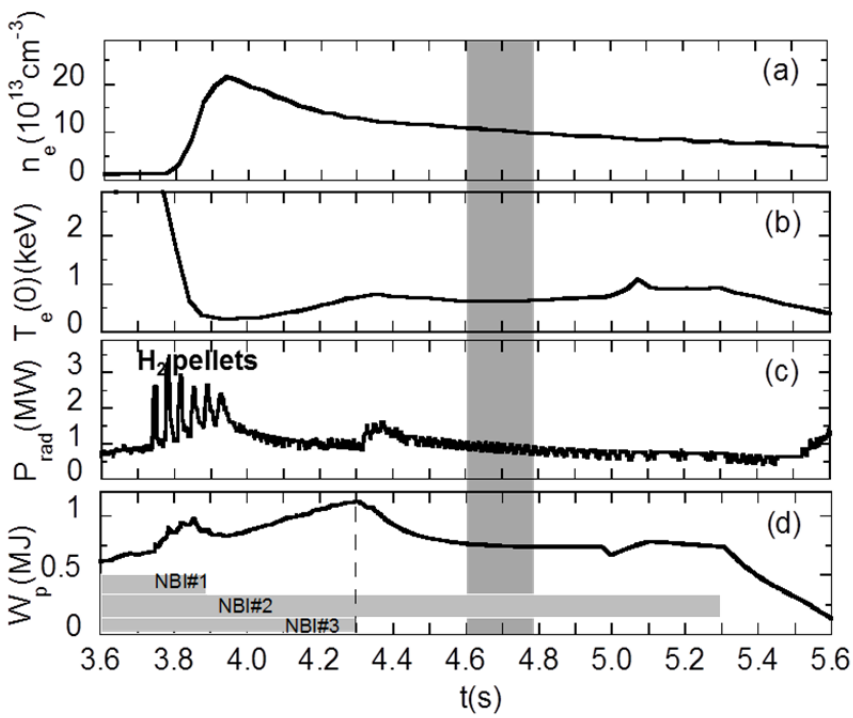

Fig. 6.4 Time evolution of (a) line-averaged electron density, (b) central electron temperature, (c) radiation power and (d) plasma stored energy together with NBI port-through power. The vertical hatched region denotes the time frame when the emission profile is analyzed.

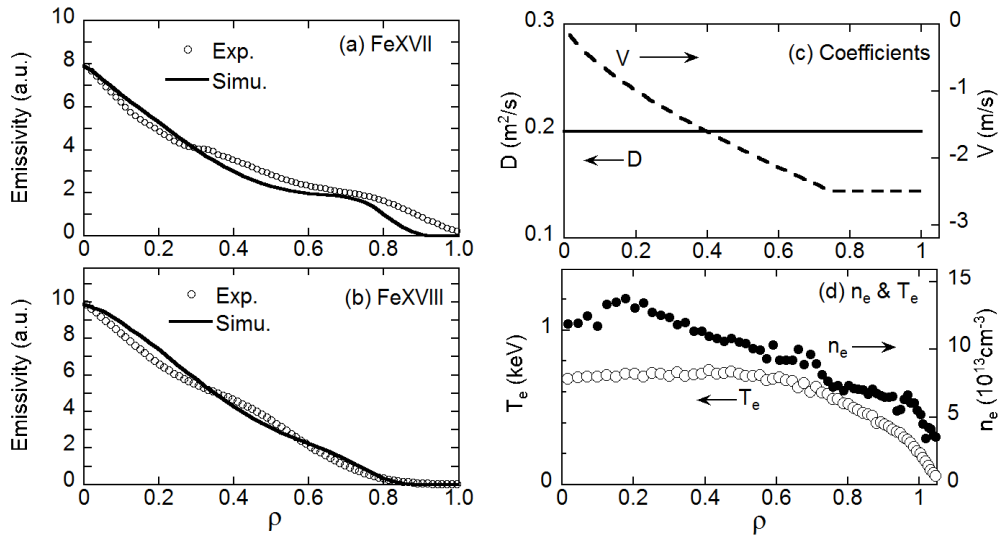

Fig. 6.5 Experimental (open circles) and simulated (solid line) profiles of (a) FeXVII at 15.02 Å and (b) Fe XVIII at 14.20 Å, (c) profiles of diffusion coefficient (solid line) and convection velocity (dashed line) and (d) profiles of electron temperature (open circles) and density (solid circles); R_{ax} = 3.6 m, NBI heating.

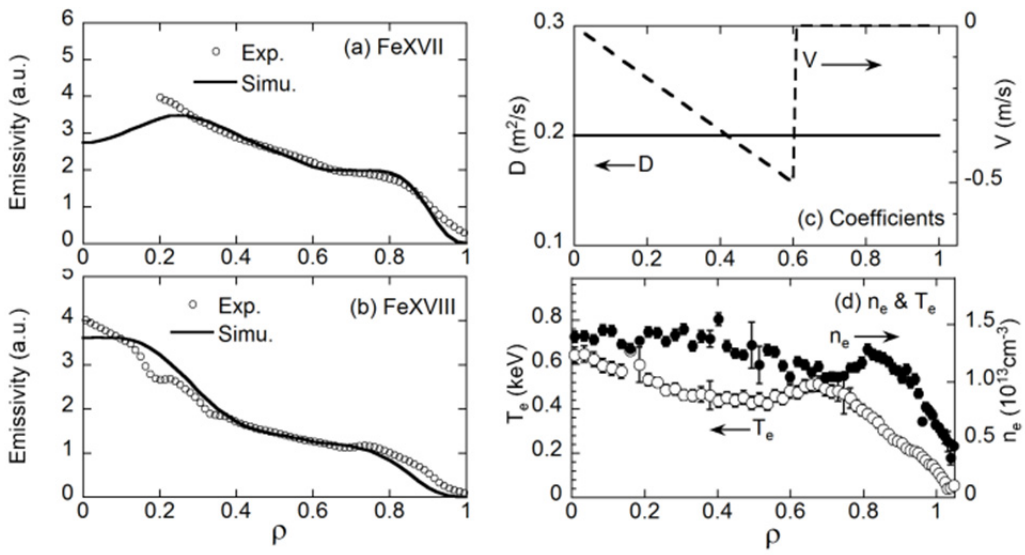

Fig. 6.6 Experimental (open circles) and simulated (solid line) profiles of (a) FeXVII at 15.02 Å and (b) Fe XVIII at 14.20 Å, (c) profiles of diffusion coefficient (solid line) and convection velocity (dashed line) and (d) profiles of electron temperature (open circles) and density (solid circles) in discharges with ECH off-axis heating at R_{ax} = 3.75 m.

Analysis is also carried out for low-density discharge with off-axis ECH heating, as shown in Fig. 6.6. The density profile shows a slightly peaked one in the plasma core (see Fig. 6.6(d)). In this case, a weak inward convection is observed only in the plasma core at $\rho < 0.6$ where the density profile is slightly peaked towards the center. In the outer region of $0.6 \leq \rho \leq 1.0$, the convection suddenly vanishes. The density gradient changes the sign to positive from negative at $\rho = 0.7$. The behavior of the two parameters, i.e. density and temperature profiles, suggests the density gradient drives the inward convection. On the other hand, the effect of temperature screening is not so obvious because the temperature gradient is negative at both the plasma core ($\rho \leq 0.4$) and edge ($0.7 \leq \rho \leq 1.0$).

6.5 Fe transport analysis of discharges with hollow density profile

Fe pellets are injected into the LHD plasma at different densities for the impurity transport study. As shown in Fig. 6.7, the time evolution of Fe line emissions is clearly distinguishable at different densities and at different ionization stages. The decay time of FeXVII and FeXX is plotted against n_e in Fig. 6.8. Here, the decay time, t_{decay}, is defined by a time at which the line intensity becomes half to the peak intensity.

The intensity decay time of FeXX is longer than that of FeXVII and the decay time increases with n_e. It then indicates that the impurity has a long confinement time near the plasma center and can be concentrated in the plasma core when n_e becomes higher.

In these discharges, the density profiles are hollow, as shown in Fig. 6.9(c). The transport analysis is then carried out to investigate the effect of density profiles.

The impurity transport is studied for hydrogen discharges with Fe pellet injection. The magnetic axis position is 3.6 m and the toroidal field is 2.75 T. At first the radial emissivity profile of FeXVII, FeXIX, FeXXI and FeXXIII is calculated as a function of averaged minor radius from measured intensity profiles, and then the density profile of Fe^{16+}, Fe^{18+}, Fe^{20+} and Fe^{22+} ions is derived by concerning the emission rate coefficient in addition to the electron temperature and density profiles. The result is plotted at three different times in Figs. 6.9(a), (b) and (c) with open symbols. The

profile data at $\rho > 1$ are not available because the VMEC magnetic surface calculation is possible within $\rho = 1$. The density profiles obtained at different radial location are analyzed with the impurity transport code. The simulated result is also plotted in Figs.

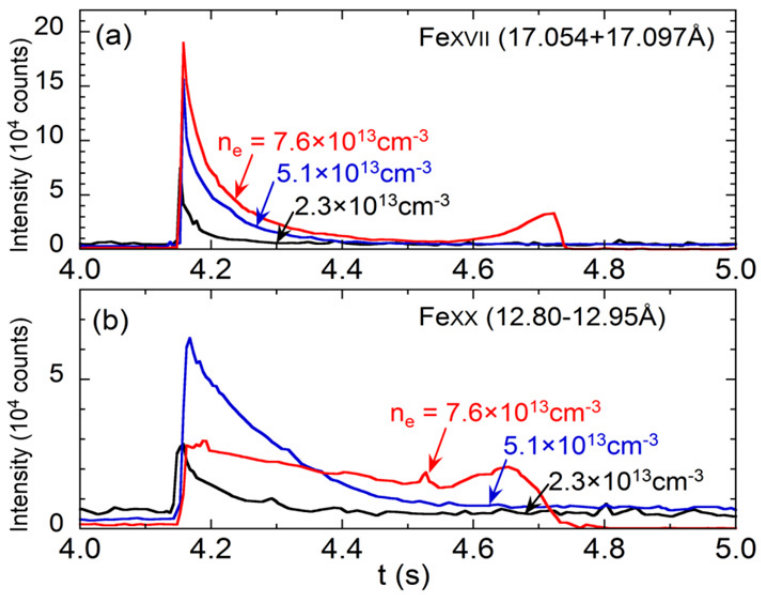

Fig. 6.7 Time evolution of (a) FeXVII and (b) FeXX after pellet injection in NBI discharges with different densities at R_{ax} = 3.6 m and B_t = -2.75 T (shot #125724–#125735).

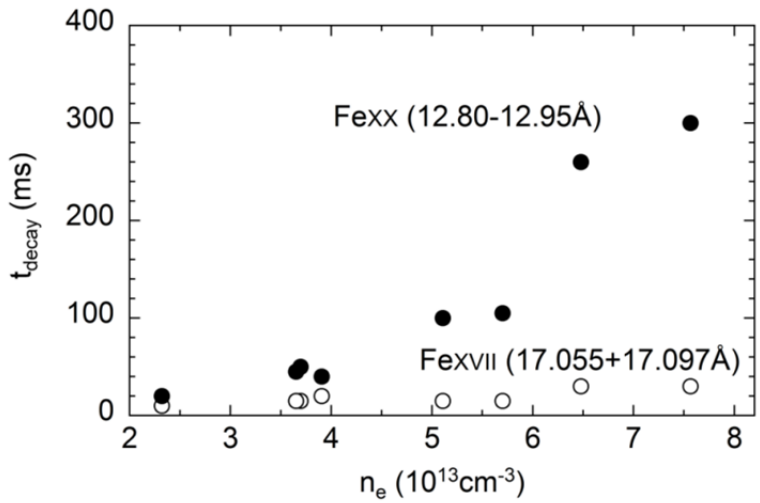

Fig. 6.8 Decay time of FeXVII (open circles) and FeXX (closed circles) emissions as a function of n_e. The decay time is defined by a time at which the line intensity becomes half to the peak intensity.

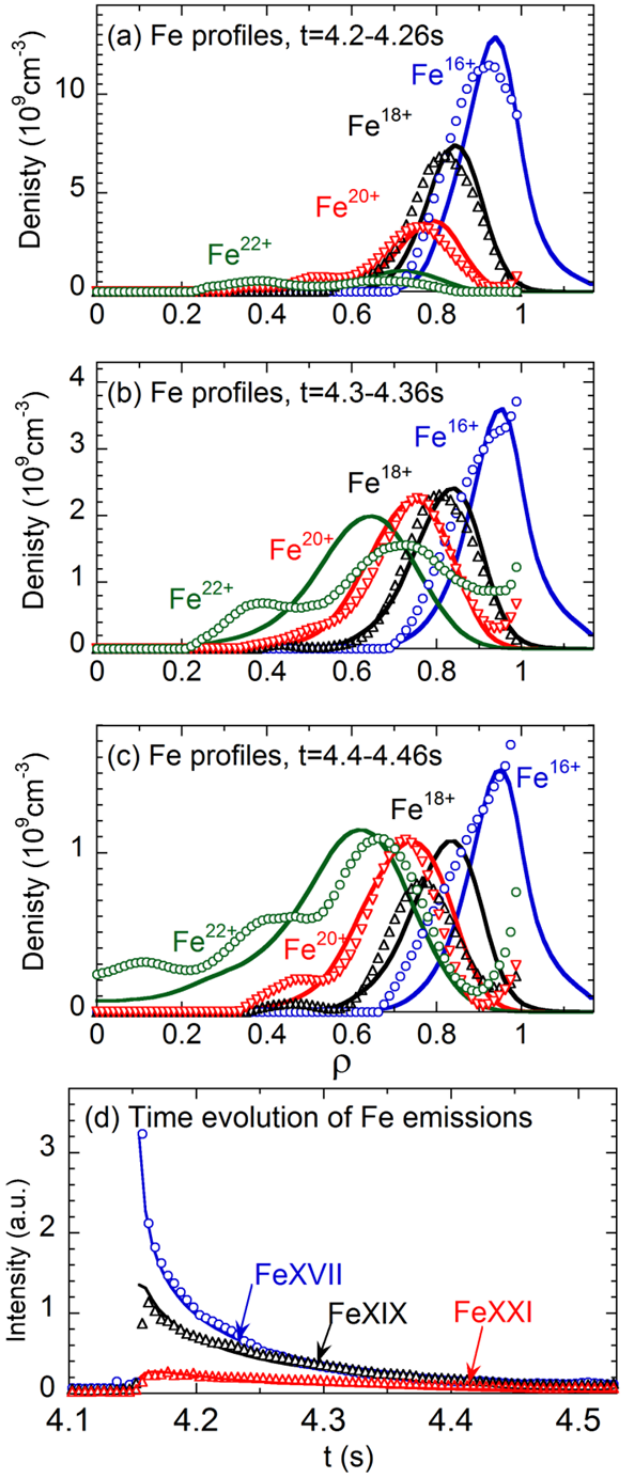

Fig. 6.9 Experimental (open symbols) and simulated (solid lines) density profiles of Fe^{16+}, Fe^{18+}, Fe^{20+} and Fe^{22+} ions at (a) t = 4.2–4.26 s, (b) t = 4.3–4.36 s and (c) t = 4.4–4.46 s, and (d) time evolution of FeXVII, FeXIX and FeXXI emissions (open symbols: experiment, solid lines: simulation).

6.9(a), (b) and (c) with solid lines. The transport code can well reproduce the iron density profile, in particular for relatively low-ionized iron such as Fe^{16+}, Fe^{18+} and Fe^{20+} ions. In case of Fe^{22+} ions, however, the agreement is a little poor because the spectral intensity of FeXXIII is considerably weak and the derived density profile includes non-negligible uncertainty. The temporal behavior in spectral intensities of FeXVII, FeXIX and FeXXI emissions is also analyzed with the simulation code, as plotted in Fig. 6.9(d). The simulation shows an excellent agreement with the measurement. It indicates that the spectral intensity decay after the pellet injection is not sensitive to the radial structure of transport coefficients. .

The radial structure of impurity transport coefficients is thus determined through the density profile analysis of iron ions. The result is shown in Fig. 6.10. The diffusion coefficient gradually increases with ρ, while the convection velocity changes its direction from outward to inward along the minor radius. The inverse point is around $\rho = 0.82$ at which the value is equal to the peak position in the hollow density profile.

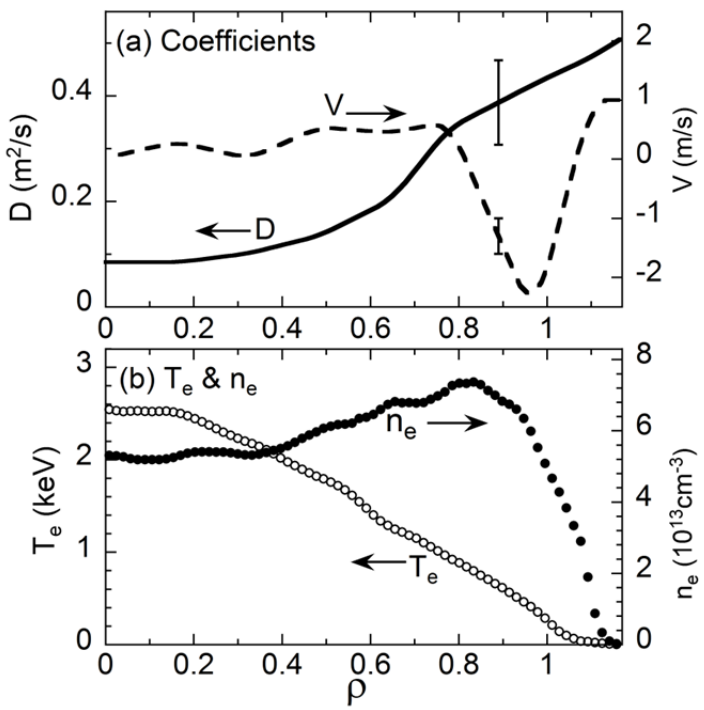

Fig. 6.10 Radial profiles of (a) diffusion coefficient (solid line) and convection velocity (dashed line) and (b) electron temperature (open circles) and density (solid circles).

Since the carbon density is usually less than 10^{-2} to the electron density in high-density discharges, the proton density should be nearly equal to the electron density. Therefore, the result suggests the convection is related to the ion density gradient. This also shows a qualitative agreement with the neoclassical theory on the impurity transport which predicts that the impurity ion is concentrated in the peak position of the ion density profile.

In addition, the outward convection can be observed even in discharges with impurity accumulation if the density profile is hollow. The waveform of the discharge is shown in Fig. 6.11 for NBI port-through power, electron density, electron temperature, radiation power, plasma store energy and the total intensity of Fe L_α

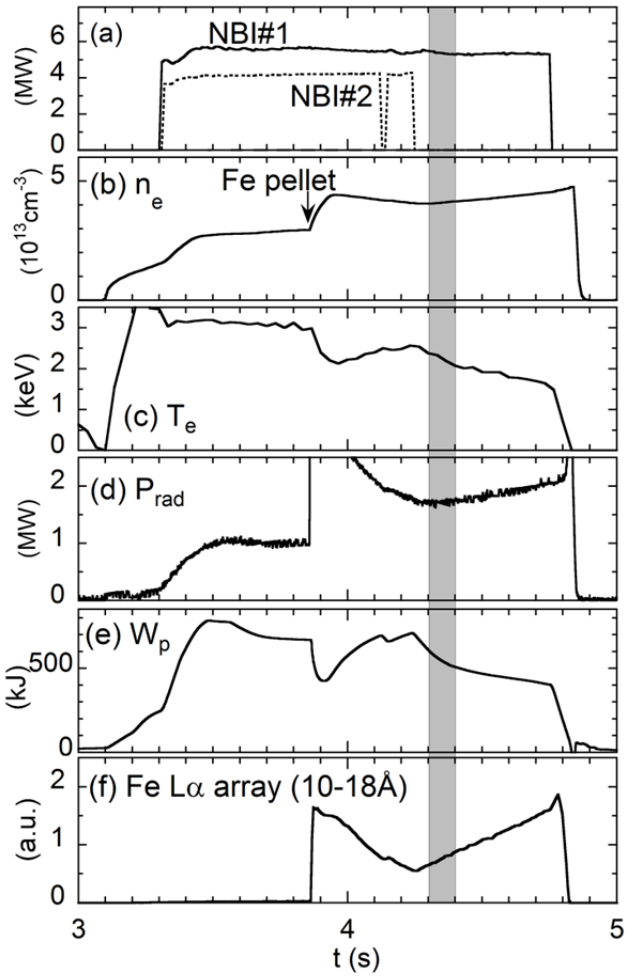

Fig. 6.11 Waveforms in discharge with impurity accumulation; (a) NBI port-through power, (b) electron density, (c) electron temperature, (d) radiation power, (e) plasma store energy and (f) total intensity of Fe L_α array.

array. The total intensity of Fe L_α array quickly increases when one of two NBI beams is switched off at $t = 4.2$ s. It indicates a start of the impurity accumulation.

The result of impurity transport analysis is shown in Fig. 6.12. A large inward convection velocity is obtained at the plasma edge of $\rho \geq 0.8$ where n_e gradient is large. However, the convection changes the direction in the plasma core where the density profile is slightly hollow. The effect of temperature screening is not clearly observed in such discharges because the temperature gradient is almost the same in the whole plasma radii.

In order to clarify the dependence of convection velocity on density gradient, which is suggested by the neoclassical theory, the impurity transport analysis has been carried out in NBI discharges with different densities at $R_{ax} = 3.6$ m configuration. In

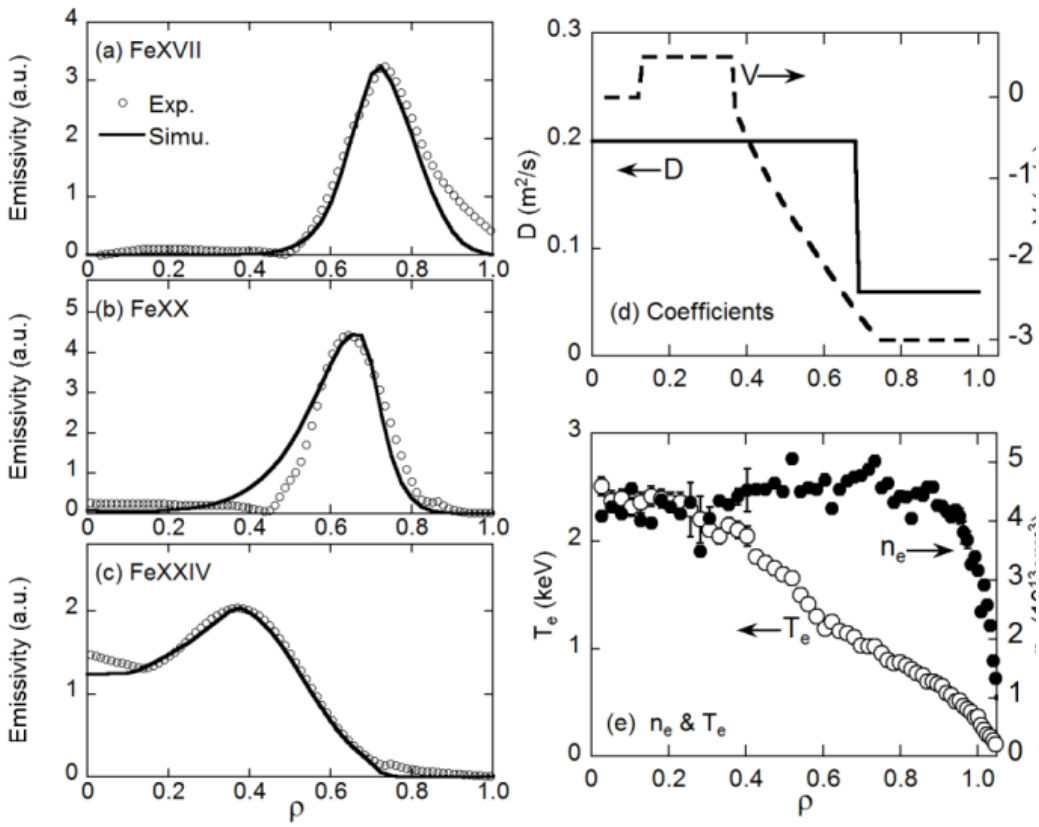

Fig. 6.12 (a) Experimental (open circles) and simulated (solid line) radial profiles of FeXVII at 15.02Å and (b) FeXVIII at 12.818 Å and (c) FeXXIV at 10.62 Å & 10.66 Å, (d) radial profiles of diffusion coefficient (solid line) and convection velocity (dashed line) and (e) radial profiles of electron temperature (open circles) and density (solid circles).

these discharges the density always exhibits a hollow profile. The analysis is then focused on the impurity transport study in discharges with hollow density profile. The result of transport coefficient at $\rho = 0.55$ is shown in Figs. 6.13 and 6.14. The diffusion coefficient, *D,* is around 0.2 m^2/s and seems to be independent of density as seen in Fig. 6.13, while the convection velocity, *V*, tends to decrease with density. Then, the relation between the convection velocity and normalized density gradient,

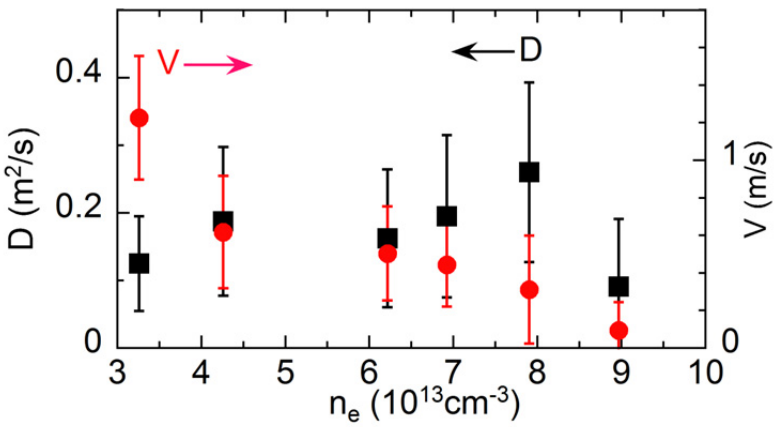

Fig. 6.13 Diffusion coefficients (solid squares) and convection velocities (solid circles) at $\rho = 0.55$ as a function of electron density in discharges with iron pellet injection.

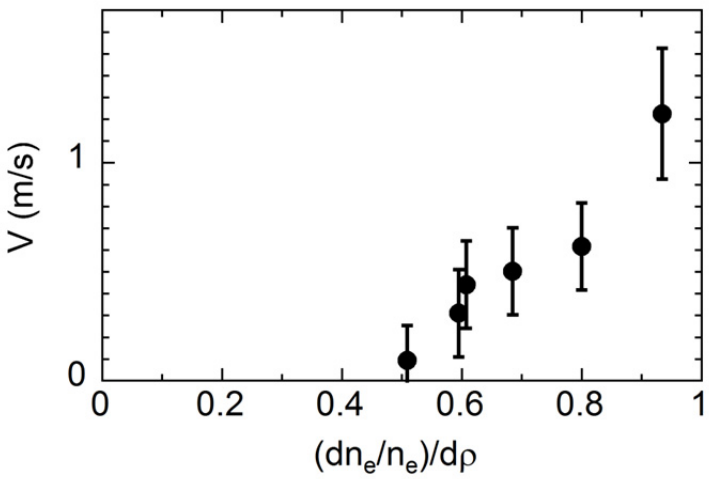

Fig. 6.14 Convection velocities at $\rho = 0.55$ as a function of normalized density gradient in discharges with iron pellet injection.

$(dn_e/n_e)/d\rho$, is examined because the density gradient changes according to the density range. The result is displayed in Fig. 6.14. The convection velocity clearly increases with increasing normalized density gradient. This result can well explain the density dependence of emission decay time shown in Fig. 6.8. Since the normalized density gradient $(dn_e/n_e)/d\rho$ is smaller at higher density ranges, the outward convection velocity becomes small. As a result, the Fe ions stay during longer period in the plasma at higher n_e as seen in Fig. 6.8.

6.6 Summary

Impurity transport analysis has been carried out in discharges with peaked and hollow density profiles. It is found that the normalized density gradient has an important role on the formation of the convection velocity. In the discharge with impurity accumulation inward convection is shown to be closely related to the centrally peaked density profile. A large outward convection velocity is observed in the plasma core when a hollow density profile occurs. The convection velocity changes the direction at radial location where the density gradient changes the sign. The study is also done for discharges with different densities using iron impurity pellet injection. The result shows that the convection velocity increases with increasing normalized density gradient, whereas the diffusion coefficient does not exhibit any obvious dependence on both the density and density gradient.

References

[1] S. Morita *et al.*, Plasma Sci. Technol. **8**, 55 (2006).

[2] Y. Nakamura *et al.*, Nucl. Fusion **43**, 219 (2003).

[3] M. Yoshinuma *et al.*, Nucl. Fusion **49**, 062002 (2009).

[4] C. F. Dong *et al.*, Plasma Sci. Technol. **15**, 230 (2013).

[5] X. L. Huang *et al.*, Rev. Sci. Instrum. **85**, 043511 (2014).

[6] R. Katai *et al.*, Jpn. J. Appl. Phys. **46**, 3667 (2007).

[7] G. Pretzier *et al.*, Z. Naturforsch. **47a**, 955 (1992).

[8] S. P. Hirshman *et al.*, Comput. Phys. Commun. **43**, 143 (1986).

[9] A. Bar-Shalom *et al.*, J. Quant. Spectrosc. Radiat. Trans., **71**, 169 (2001).

[10] T. Amano, J. Mizuno, and J. Kako, Simulation of impurity transport in tokamak, Int. Rep. IPPJ-616, Institute of Plasma Physics, Nagoya University (1982).

[11] S. Morita, *et al.*, Plasma Sci. Technol. **8**, 55 (2006).

[12] N. R. Badnell, Astrophys. J. Suppl. Ser. **167**, 334 (2006).

[13] N. R. Badnell *et al.*, Astron. Astrophys. **406**, 1151 (2003).

[14] K. P. Dere, Astron. Astrophys **466**, 771 (2007).

Chapter 7

Summary

A space-resolved extreme ultraviolet (EUV) spectrometer working in the wavelength range of 10–130 Å has been developed to measure vertical profiles of line emissions of heavy impurities and bremsstrahlung continuum at horizontally elongated plasma cross section in the Large Helical Device (LHD). The spectrometer has a spectral resolution of 0.15 Å at 30 Å when an entrance slit with 100 μm width is used. The spatial resolution in the vertical direction is sufficiently good, i.e. approximately 30 mm, when a spatial-resolution slit with 1 mm width is used. The spatial resolution in the toroidal direction is also good, i.e. 22 mm. The value is enough to measure the radial profile of impurity line emissions with good spatial resolution avoiding the effect on a quick poloidal turn of LHD elliptical plasmas.

The spectral intensity of the present system is absolutely calibrated as a function of wavelengths based on the profile measurement of visible and EUV bremsstrahlung continua. The calibration factor is also examined along the grating groove in the spectrometer with horizontal wavelength dispersion. A constant reflectivity of EUV emissions observed along the grating groove can validate the present vertical profile measurement. These results obtained here indicate a sufficient performance of the present space-resolved EUV spectrometer system for the profile measurement.

A large amount of spike noise caused by neutral particles with high energies (≤ 180 keV) has been observed with the EUV spectrometer in NBI discharges of LHD. These high-energy neutral particles originating in fast ions from neutral beam injection (NBI) bring a serious problem to the EUV spectroscopy, especially in low-density discharges at which the slowing down time of the fast ion is very long. A holographic grating used in the present spectrometer causes more spike noises compared to a ruled grating. It is probably due to a geometric difference in the groove structure, i.e. rectangular shape for the holographic grating and triangle shape for the ruled grating. The pulse height distribution analysis on the spike noise using signal counts of charge-coupled detector (CCD) definitely concludes that the spike noise is composed of high-energy neutral particles attributed to 180 keV n-NBIs and 40 keV p-NBIs.

Three filters of 0.5 μm thick polyethylene terephthalate (polyester, PET), 3.3 μm thick polypropylene (PP) and 11 μm thick beryllium (Be) have been tested to block the spike noise. The 11 μm Be and the 3.3 μm PP filters entirely eliminate all the spike noise, but the signal intensity is also significantly reduced. The 0.5 μm PET filter fully eliminates the low-energy neutral particles originating in the p-NBIs, while the high-energy neutral particles originating in the n-NBIs cannot be sufficiently blocked. However, a small amount of the spike noise remaining in the EUV spectrum can be erased by computer software programing. The 0.5 μm PET is thus selected as the best filter in the present EUV system.

Based on the good spectral and spatial resolutions, the Fe n = 3–2 L_α transition array consisting of FeXVII to FeXXIV is excellently observed with their radial profiles. The transition array is distributed in narrow wavelength range of 10 to 18 Å, the radial profile from all the charges states of FeXVII to FeXXIX can be simultaneously measured as a function of time. Therefore, the transition array is used

as a new technique for the impurity transport study. The result is mentioned later. Each transition in the L_α array can be accurately identified with its radial profile. Through the analysis a spectral line observed at 17.62 Å is newly identified as FeXVIII transition.

Two types of coaxial pellets, i.e. tungsten inserted into PE tube (polyethylene) and tungsten inserted into C tube (graphite carbon), have been designed and tested in LHD for the tungsten spectroscopy and transport study. Experimental results show the W-in-PE pellet can avoid plasma collapse, whereas the W-in-C pellet usually terminates the discharge. The reason is clearly explained by the analysis of pellet deposition profile based on pellet ablation spectroscopy with interference filters. Since the graphite carbon has a high sublimation energy, the tungsten pellet can be delivered into deeper radial location (ρ = 0.43). It leads to a huge energy loss by the tungsten ions in the plasma core including radiation and ionization losses. In the case of the W-in-PE pellet, on the contrary, the energy loss is much smaller due to a shallower penetration (ρ = 0.7), suggesting some of evaporated tungsten ions are not well confined in the plasma. The plasma can then survive from the tungsten pellet injection. As a result, the W-in-PE pellet can excellently produce sufficient emissions from highly ionized tungsten ions in LHD.

Several tungsten spectra are measured with the W-in-PE pellet. Radial emissivity profiles are also obtained for WXXV (32.3 Å), WXXVI (30.9 Å) and WXXVII (29.6 Å). Based on the emissivity profile measurement of tungsten ions in different ionization stages, the rate coefficient of ionization and recombination can be experimentally derived. Therefore, the present result is greatly helpful not only for the atomic modeling of tungsten spectra but also for the tungsten transport study in fusion devices with tungsten divertor.

Ne-like FeXVII n = 3–2 L_α transitions ($2p^5 3d$ or $3p^5 3s$ to ground state: $2p^6\ {}^1S_0$) denoted with labels of 3C ($3d\,{}^1P_1$), 3D ($3d\,{}^3D_1$), 3E ($3d\,{}^3P_1$), 3F ($3s\,{}^3P_1$), 3G ($3s\,{}^1P_1$) and M2 ($3s\,{}^3P_2$) have been observed from LHD plasmas along with the radial intensity profile. The measured line-integrated radial intensity profile is reconstructed to the radial emissivity profile of FeXVII transitions by means of Abel inversion, and the emissivity ratio among the FeXVII transitions is analyzed. A collisional-radiative (CR) model specially developed for the Fe ions is applied for analyzing the data. Although the emissivity ratios of $\varepsilon_{3D}/\varepsilon_{(3G+M2)}$ and $\varepsilon_{3F}/\varepsilon_{(3G+M2)}$ well agree with the CR model calculation, the emissivity ratio of $\varepsilon_{3C}/\varepsilon_{(3G+M2)}$ shows a clear discrepancy by

25%–40%. The result indicates that the discrepancy is not caused by the chord-integrated effect in the measured intensity. It seems that the theoretically calculated excitation cross section of 3C transition is an overestimate due to uncertainty of the atomic wave function used in the calculation. The effect of electron density on the emissivity ratio of $\varepsilon_{3F}/\varepsilon_{(3G+M2)}$ is also examined. It is found that that the ratio is also sensitive to the electron density in addition to the electron temperature.

The bremsstrahlung profile has been successfully observed without spike noise at low-density discharges, e.g. 2.9×10^{13} cm^{-3}, as well as high-density discharges, by installing the PET filter and optimizing the entrance and space-resolved slit widths. The Z_{eff} profile has been also obtained in the plasma core ($\rho < 0.75$) from the measured EUV bremsstrahlung radial distribution. Recombination radiation can give a significant effect on the bremsstrahlung profile, in particular, in the edge region ($\rho > 0.75$), since the energy of EUV bremsstrahlung is relatively high, e.g. 100–600 eV. In the plasma core ($\rho < 0.75$), on the other hand, the emissivity profile is basically free of the recombination radiation because the radiative recombination rate drastically decreases with increasing electron temperature T_e. The time behavior of Z_{eff} profiles analyzed in low-density NBI discharges with carbon pellet injection suggests a strong relation between Z_{eff} and T_i. The value of Z_{eff} decreases with increasing electron density n_e in both the NBI- and ICRF-heated discharges, while it has no obvious correlation with n_e in ECH discharges.

The Fe n = 3–2 L_α transition array is of great advantage because the transition array consists of emissions from several charge states of Ne-like Fe^{16+} through Li-like Fe^{23+} ions. Radial profiles of all the charge states can be simultaneously measured with the EUV spectrometer developed in the present study. Therefore, the radial structure of transport coefficients, i.e. diffusion coefficient D and convection velocity V can be analyzed basically without any assumption because the iron line emissions in the transition array distribute over the whole radial location. The time behavior of the Fe transition array is examined by injecting the impurity pellet. It is found that the intensity decay time of FeXX is longer than that of FeXVII and the decay time increases with n_e. It suggests the impurity confinement time is longer when n_e increases. The impurity transport analysis is attempted to discharges with different density profiles. In the case of centrally peaked n_e profile, the radial structure of the inward convection velocity seems to be similar to the n_e profile, suggesting the importance of the density gradient. In the hollow n_e profile, on the contrary, a large

outward convection velocity is observed in the plasma center. The convection velocity changes from outward to inward at certain radial location in the peripheral region where the n_e gradient changes the sign, i.e. from positive to negative. Analysis of discharges with iron pellet injection at different density ranges shows that the convection velocity increases with the normalized density gradient, whereas the diffusion coefficient does not exhibit any obvious dependence on the density or the density gradient. The present result on the convection velocity shows a qualitatively good agreement with the neoclassical theory.

In conclusion, based on the space-resolved EUV spectrometer and impurity pellets newly developed through the present work, both the EUV spectra of impurity line emissions and bremsstrahlung continuum have been measured with their radial profiles in the wavelength range of 10–130 Å. The line emissions including the Fe n = 3–2 L_α transition array and tungsten spectra are well identified with their radial profile analyzed and the Z_{eff} profile is successfully obtained from EUV bremsstrahlung in low-density discharges. Comparison between Z_{eff} and T_i profiles indicates the central T_i increases with Z_{eff} value. Impurity transport is analyzed in discharges with peaked and hollow density profiles without assumption of radial profiles of transport coefficients, D and V, based on the radial profile of Fe L_α transition array. The result clearly indicates the impurity transport is entirely affected by the convection velocity and the convection velocity depends on the density gradient.

Acknowledgements

The doctoral thesis is completed through three-year study at National Institute for Fusion Science (NIFS), Toki, Japan. I owe my thanks to many people who have made the thesis possible.

First of all, I would like to express my deepest and most sincere gratitude to my supervisor, Prof. Shigeru Morita. His excellent and elaborate guidance leads me to the field of plasma spectroscopy and impurity study. He taught me knowledge and skills in plasma experiments and scientific writing. I greatly appreciate all his invaluable suggestions which help me to overcome many difficulties. He has been an exemplary teacher and researcher for me to learn from. His constant encouragement, patience and care support me both in the study and my personal life in Japan. I feel very fortunate to carry out my PhD study under his supervision.

I am deeply grateful to Dr. Tetsutarou Oishi for his vital help in experimental work and in the impurity transport code. I wish to thank Prof. Izumi Murakami for the series of lectures on atomic physics and for the kindly calculated rate coefficients of Fe transitions which are essential data for the thesis work. I am sincerely thankful to Dr. Motoshi Goto for his technical support in spectral data acquisition and his help in my daily life when I first arrived at NIFS. I am also thankful to Dr. Daiji Kato for useful discussion and advice about atomic data.

I am sincerely thankful to my tutor, Dr. Erhui Wang, for discussions on plasma spectroscopy and plenty of help in my daily life during the first year in Japan. I thank Dr. Chunfeng Dong for the help in the absolute intensity calibration of spectrometers. I would also like to thank my friends, Dr. Tingfeng Ming, Dr Haishan Zhou, Dr. Hao Wang, Mr. Xiaodi Du, Mr. Hongming Zhang, Ms. Haiying Fu, Mr. Shaofei Geng, Dr. Xiang Ji, Mr. Hailin Bi and Mr. Yue Xu.

I wish to express my gratitude to all members of the LHD experimental group and staffs of NIFS and The Graduate University for Advanced Studies (SOKENDAI) for their supports.

I owe my deep gratitude to Prof. Zhengying Cui, Southwestern Institute of Physics (SWIP), Chengdu, China, for supporting me pursuing the PhD overseas. I also thank Prof. Zhongbing Shi and Prof. Qingwei Yang for their supports and suggestions.

Finally, I want to thank my parents and my brother. Their never-ending supports give me strength and motivation to accomplish the goals of the thesis work.

Publications

[1] "Space-resolved extreme ultraviolet spectroscopy free of high-energy neutral particle noise in wavelength range of 10-130Å on the large helical device"
X. L. Huang, S. Morita, T. Oishi, M. Goto and C. F. Dong
Review of Scientific Instruments, **85**, 043511 (2014).

[2] "Radial profiles and emissivity ratio analysis of Ne-like FeXVII n=3-2 transitions in Large Helical Device"
X. L. Huang, S. Morita, T. Oishi, I. Murakami, M. Goto, C. F. Dong and E. H. Wang.
Journal of the Korean Physical Society, **65**, 1265 (2014).

[3] "Coaxial pellets for metallic impurity injection on the large helical device"
X. L. Huang, S. Morita, T. Oishi, M. Goto and H. M. Zhang,
Review of Scientific Instruments, **85**, 11E818 (2014).

[4] "Evaluation of Z_{eff} profile in low-density and high-Ti discharges with carbon pellet injection based on space-resolved EUV spectroscopy in LHD"
X. L. Huang, S. Morita, T. Oishi, M. Goto and H. M. Zhang
Plasma and Fusion Research, **10**, 3402036 (2015).

[5] "Iron transport study using radial profiles of Fe n=3-2 L_α transition array in the Large Helical Device "
X. L. Huang, S. Morita, T. Oishi, I. Murakami, M. Goto and H. M. Zhang
To be submitted to Physics of Plasmas.